GROWTH OF SEMICONDUCTING (CdS, CdSe and ZnSe) AND CONDUCTING FILMS (NiFe) AND INVESTIGATION ON THEIR ELECTRICAL, MAGNETIC AND OPTICAL PROPERTIES

Ph.D Thesis

in

Engineering Physics

University of Gaziantep

By

Metin Bedir

November 2002

Approval of the Graduate School of Natural and Applied Sciences

Prof.Dr. A.Rıza Tekin
Director

I certify that this thesis satisfies all the requirements as a thesis for the degree of Doctor of Philosophy.

Prof.Dr.Ömer F.Bakkaloğlu
Head of Department

This is to certify that we have read this thesis and that in our opinion it is fully adequate, in scope and quality, as a thesis for the degree of Doctor of Philosophy.

Assist.Prof.Dr.Mustafa Öztaş
Co-Supervisor

Prof.Dr.Ömer F.Bakkaloğlu
Supervisor

Examining Committee Members

Prof.Dr.Ömer F.Bakkaloğlu

Prof.Dr.Refik Kayalı

Assoc. Prof.Dr.Beşire Gönül

Assoc.Prof.Dr.Ömer Eyercioğlu

Assist. Prof.Dr.A.Necmeddin Yazıcı

ABSTRACT

GROWTH OF SEMICONDUCTING (CdS, CdSe and ZnSe) AND CONDUCTING FILMS (NiFe) AND INVESTIGATION ON THEIR ELECTRICAL, MAGNETIC AND OPTICAL PROPERTIES

BEDİR, Metin

Ph.D. in E.P., University of Gaziantep
Supervisor: Prof.Dr. Ömer Faruk BAKKALOĞLU
Co-supervisor: Assist.Prof.Dr. Mustafa ÖZTAŞ

November 2002, 166 Pages

In this study, semiconducting CdS, CdSe and ZnSe thin films were developed by using spraying pyrolysis and electrodeposition method, conducting NiFe alloy films were grown by electrodeposition method on different substrates under different deposition conditions and their electrical, magnetic and optical properties were widely investigated by using different techniques.

The optical properties of the semiconducting were investigated from optical absorption coefficient and transmittance spectra data using double beam visible spectrofotometer. By using these data the band gap energies of the semiconducting thin films were determined. The crystal structures of semiconducting (CdS, CdSe, and ZnSe) thin films and conducting (NiFe) films were determined from x-ray diffraction peaks and the thicknesses of the sprayed CdS, CdSe and ZnSe thin film samples were calculated by using weighing method. The electrical properties of the semiconducting thin film samples were investigated by Van der Pauw method (four ohmic contact). The changes in the resistivities, conductivities and Hall mobilities of the semiconducting thin films under different substrate temperatures have been investigated. The surface morphology of NiFe alloy film samples were examined from scanning electron microscope (SEM) photos nickel (Ni) and iron (Fe) concentration in NiFe alloy film samples were calculated by using the atomic absorption spectrometer results also the thicknesses of samples were determined. The electrical and magnetic properties of electrodeposited NiFe conducting alloy films were investigated by using a 2 Tesla home made electromagnet and Van der Pauw method (four ohmic contact), respectively, for different geometries (magnetic fields were applied under the different angles onto film surface) at room temperature. The temperature dependent magnetoresistance measurements were done under the influence of a constant magnetic field of 0.8 Tesla for two different geometries (longitutional and transverse). Magnetization properties of the NiFe alloy film samples were also determined by vibrating sample magnetometers (VSM).

Key words: Spray Pyrolysis method, Electrodeposition method, CdS, CdSe, ZnSe, magnetoresistance, NiFe alloy films.

ÖZ

YARIİLETKEN(CdS, CdSe and ZnSe) VE İLETKEN (NiFe) FİLMLERİN BÜYÜTÜLEREK ONLARIN ELEKTRİKSEL, MANYETİK VE OPTİKSEL ÖZELLİKLERİNİN ARAŞTIRILMASI

BEDİR, Metin

Doktora Tezi, Fizik Mühendisliği, Gaziantep Üniversitesi
Danışman: Prof.Dr.Ömer Faruk BAKKALOĞLU
Yrd. Danışman: Yrd.Doç.Dr. Mustafa ÖZTAŞ

Kasım 2002, 166 Sayfa

Bu çalışmada, püskürtme ve elektrodepolama yöntemiyle CdS, CdSe ve ZnSe yarı iletken filmleri ve iletken NiFe alaşım filmleri elektrodepolama yöntemiyle farklı alt tabanlar üzerine, farklı depolama yöntemleri uygulanarak büyütülüp onların elektriksel, manyetiksel ve optiksel özellikleri farklı teknikler kullanılarak araştırılmıştır.

Yarı iletken filmlerin optiksel özellikleri çift ışıklı olup görünür bölgede çalışan spektrometreden elde edilen optiksel soğurma katsayıları ve geçirgenlik tayflarının analiziyle araştırılmıştır. Bu veriler kullanılarak yarı iletken filmlerin enerji band değerleri hesaplanmıştır. Yarı iletken (CdS, CdSe ve ZnSe) ince filmlerin ve iletken (NiFe) filmlerinin kristal yapıları x-ışınımı difraktometresinden elde edilen pikler kullanılarak incelenmiş ve püskürtme yöntemiyle elde edilen CdS, CdSe ve ZnSe yarı iletken ince filmlerin kalınlıkları ağırlık yöntemiyle hesaplanmıştır. Yarı iletken ince filmlerin elektriksel özellikleri Van der Pauw (dört nokta kontakt) metoduyla incelenmiştir. Farklı alt taban sıcaklığında elde edilen yarı iletken ince filmlerinin özdirençlerinin, öziletkenliklerinin ve Hall mobilitelerinin alt taban sıcaklığına göre değişimi araştırılmıştır. NiFe alaşım film örneklerinin yüzey yapısı, yüzey tarayıcı elektron mikroskobu (SEM) ile çekilen fotoğraflarla belirlenmiş ve filmlerin içerisindeki Ni ve Fe yüzde oranlarıyla filmlerin kalınlıkları Atomik Absoption spektrofotometresiyle elde edilen sonuçlar kullanılarak hesaplanmıştır. İletken NiFe alaşım filmlerin elektriksel ve manyetik özellikleri 2 Teslalık elektromıknatısla Van der Pauw (dört nokta kontakt) yöntemi kullanılarak oda sıcaklığında farklı geometriler (manyetik alan film yüzeyine farklı açılarla uygulanarak) ve 0.8 Tesla'lık sabit manyetik alan altında sıcaklığa bağlı magnetoresistance ölcümleri yapılarak incelenmiştir. Bunun yanı sıra NiFe alloy filmlerin manyetizasyon özellikleri VSM (vibrating sample magnetometre) ölçümleri alınarak incelenmiştir.

Anahtar kelimeler: Püskürtme yöntemi, elektrodeposition yöntemi, CdS, CdSe, ZnSe, manyetoresistance, NiFe alaşım filmler.

ACKNOWLEDGMENTS

The author would like to express his thanks to his supervisor, Prof.Dr. Ömer Faruk Bakkaloğlu, and co-supervisor, Assist.Prof.Dr. Mustafa ÖZTAŞ, not only for their guidance, encouragement, assistance, advice, and suggestions but also for their great leadership in the construction of such a work.

He would like to thank to the Research Fund of Gaziantep University for financial support to this study, and Princeton Measurements Corporation (for VSM measurements). And also especially thanks to Mr. Ziya Gesoğlu, and Mr. İsmail Hakkı Karahan (University of Ataturk).

The author's special thanks go to his wife, Z.Emel BEDIR and his daughters; T. İrem and E. Ece and their aunt (mother's sister) Ş.Hayriye Üstkale.

To My Family

TABLE OF CONTENTS

LIST OF TABLES

LIST OF FIGURES

LIST OF SYMBOLS

E_g : energy bandgap
e : electron
h : hole
E_f : final energy
E_i : inital energy
h : planck constant
ν : frequency
λ : wave lengths
α : absorption coefficient
m_r : reduced mass
m_e : electron mass
I_o : photon beam of intensity
V_H : Hall potential
μ_H : hall mobility
E_H : hall field
M_s : magnetic saturation
χ : magnetic susceptibility
μ : permeability
H_d : demagnetizing field
E_{mag}: magnetostatic energy
H_c : coercive field
M_r : remanence field
K_u : anisotropy constant
t : thickness
L : mean free path
L_{TH}: thermal vibration path
L_i : impurity vibration path
σ : conductivity
ρ : resistivity
J : current density
H : magnetic field

CHAPTER I

General Introduction

The properties of the semiconducting thin films are widely investigated due to their importance in solar cell technology [1-3]. The polycrystalline thin films of ZnSe, CdTe, ZnS, ZnO, and CdS are the promising candidates for high efficiency photovoltaic applications due to their near-ideal band gap and high optical absorption coefficents. [4,5]. These systems are the representatives of semiconducting systems and can be successfully produced by the electrodeposition and spraying pyrolysis techniques [6-8].

CdS, CdSe and ZnSe are very important wide band gap semiconducting II-VI compounds which are used widely in different fields due to their optical and electronic properties. They have received considerable attentions as photo-electronic materials [1]. The excellent optical properties make them suitable for the fabrication of solar cells. Among the II-VI compounds, CdSe is a promising semiconductor material for fabrication of heterojunction solar cells and photoelectrochemical solar cells [9]. Because of their suitable band gap and high photosensitivity in the visible range of the solar spectrum, these materials can be advantageously used for low cost applications [10]. And also there is a great deal of interest in making light emitting devices, potential applications in optoelectronic devices, solar cells, IR detectors and lasers using wide band gap ZnSe as the semiconductor [11]. Polycrystalline thin films of CdS have received considerable attention during recent years because of their proven and potential applications in a variety of semiconducting devices such as solar cells, transistors, light activated valves, etc.

These semiconducting thin films can be easily obtained by several techniques such as r.f.sputtering, evaporation, chemical bath deposition, spray pyrolysis, electrodeposition, etc [7,9]. Among them, spray pyrolysis and electrodeposition are the simplest and most economic techniques to grow high quality semiconducting thin films. The method of spray pyrolysis (or solution spraying) is a convenient method for the growth of thin films for solar cell applications. Recently, this technique has been extensively studied by researchers, because spraying pyrolysis method is a simple for the deposition of semiconductor films [1,10].

Electrodeposition is a very attractive method for the growth of the metallic and semiconducting thin film materials. It is a simple technique which lends itself to large-scale production. It does not require specialized expensive equipment. Material utilization in the electrodeposition technique is extremely good since plating takes place only on the substrate. Electrodeposition can produce high purity materials if special attention is paid to the purification of the plating solutions which can be achieved by pre-electrolysis [12,13]. The main advantage of this technique is the easy control of growth rate through electrical quantities. This method has been successfully employed for the deposition of thin films of elementary, binary and ternary semiconductors. Magnetic thin films such as CoCu [14], NiFe [15,16], NiCoCu [17-19] can also be produced by electrodeposition technique.

The physical properties of thin films depend closely on their preparation conditions. For example, it has been observed that the substrate temperature plays a vital role on grain structure and the transport properties of the conducting and semiconducting samples [20]. In addition , a fast spray rate is also found to have an adverse effect on the crystallinity and grain size by introducing defects during the deposition [21].

The general aim of this thesis is to produce and investigate the electrical and optical properties of semiconducting films of CdS, CdSe, ZnSe, and the electrical and magnetic properties of NiFe alloy films. The semiconducting films were produced by both spraying pyrolysis and electrodeposition techniques while electrodeposition technique were used for the growth of NiFe alloy films. The comparison of the properties of semiconducting films produced by the both methods was carried out and results were discussed.

In this study, the semiconducting thin films of CdSe, ZnSe, CdS were grown by the electrodeposition and spraying methods on different substrates under different deposition conditions (with various temperature, pH, current density, composition of the materials and potentials). Magnetic thin films of NiFe were produced by electrodeposition technique with different deposition conditions (i.e. with different temperature, pH, composition of the bath, current density and potentials). The optical properties of semiconducting thin films were investigated with U/V double-beam spectrometer. The electrical properties of these thin films were examined with four point terminal method (or Van-der Pauw method) at different temperatures. Electrical and magnetic properties of magnetic films were investigated by using a home-made electromagnet (2T), the four point probe method and a vibrating sample magnetometer. The composition and crystal structures of these semiconducting and magnetic films were investigated by using chemical and x-ray techniques.

This thesis is divided into four main chapters. Chapter 1 is the present chapter which gives a brief description about the aim and scope of this thesis. Chapter 2 is devoted to the study of semiconducting materials. In this chapter, firstly, a brief theoretical background knowledge on semiconductors is introduced. The descriptions of the experimental methods and apparatus used in this study as well as the growth mechanisms of CdS, CdSe and ZnSe thin films are given. The results obtained on the electrical, optical and crystal structure properties of these systems are also introduced and discussed in this chapter. Chapter 3 is about the study of electrodeposited NiFe alloy films. The background knowledge on NiFe alloy and the experimental work done on the surface morphology, crystal structure, electrical and magnetic properties of this magnetic system are given and the results are discussed with the related figures and tables in this chapter.

The general conclusions on the studies in this thesis are introduced in Chapter 4 while the conclusions on the studies of semiconducting and conducting films are separately given at the ends of the relevant chapters.

CHAPTER II

SEMICONDUCTING THIN FILMS

2.1 Introduction

II-VI compound materials were the earliest materials used on a large industrial scale for the production of semiconductors. In the third decade of this century they became well known as crystal phosphors and were used as cathode-ray tube screen materials; they had a boom in colour television tubes late in the fifties and their production output is nowadays nearly comparable with Si. Semiconductors are an important class of materials both for industrial use and for scientific study. Semiconductors are a group of materials having electrical conductivities intermediate between metals and insulators. It is significant that the conductivity of these materials can be varied over wide ranges by changes in temperature, optical excitation, and impurity content. This variability of electrical properties makes the semiconductor materials naturel choices for electronic device investigations.

2.2 Literature Survey

2.2.1 Historical Perspective of Semiconducting Thin films Grown by Spraying and Electrodeposition Method

The process of spray pyrolysis was first introduced in the 1942's for the preparation of transparent oxide films. Since it has become one of the more extensively used low cost and readily scaleable techniques, spray pyrolysis has been reviewed several times in the literature [22-25]. One of its early applications was the deposition of thin films of sulphide by Chamberlin and his co-workers [26,27]. Subsequently they extended the process to the preparation of thin film CdS/$Cu_{2-x}S$ photovoltaic cells with the achievement of 2% efficiency. The technique was then adopted by the Stanford University group led by Bube, who eventually used the method to deposited a wide range of compound semiconductors. Starting with thin film of CdS, they were able to within a short period prepare solar cells by the spray pyrolysis of CdS films onto a single crystal CdTe substrate and thereby produce devices with 6% efficiency. They then extended the work to the deposition of (Cd,Zn)S films onto p-type single crystal CdTe substrates, thus forming solar cells and achieving efficiencies between 6% and 8% [28-30].

The spray pyrolysis technique has also been studied extensively by Krunks and his co-workers for photovoltaic application [31]. Their early studies in 1977 were similarly focused on the characterization and the improvement of (Cd,Zn)S thin films, and on solar cells prepared on them by the to epotaxial growth of Cu_2S using both the wet plating and the dry barrier methods. They also applied the spray pyrolysis technique to the deposition of metal oxides and ternary semiconductors.

In 1980, University of Montpellier (France) a group launched a programme to improve and stabilise Cu_2S/CdS solar cells based on sprayed CdS films. This was followed by the formation of Cu_2S layers by the well established wet plating method to complete the fabrication of the solar cell structure. Under this project the best reported efficiency was 7.5% for 1 cm^2 area cells [32]. The spray pyrolysis technique has also been studied extensively by Chopra and his co-workers for photovoltaic applications at the Indian Institute of Technology [33,34]. Their early studies in 1977 were focused on the characterisation and the improvement of (Cd,Zn)S films and their solar cells applications [35-37].

The optical properties of spray CdS films are particularly important for solar cell applications and are mainly determined by the microstructure of the layers. It has been demonstrated that the optical transmission of films improves as the substrate temperature and the relative concentrations of sulphur in the spray solution are increased [38]. The spray pyrolysis techique has also been studied by Kwok and his co-workers at the Chinese University of Hong Kong. They have reported a series of detailed studies of Cu_2S/(Cd,Zn)S solar cells prepared on spray pyrolysed CdS and

(Cd,Zn)S thin films using the wet plating method [38-40]. Although a great deal of effort has been put into CdS/Cu_2S solae cells since 1960, their efficiency is estimated to be limited to about 10% because of differences in the electron affinities and the lattice parameters of the two semiconductors.

Tomar and Garcia at the University of Simon Bolivar have also dealt with the spray pyrolysis of II-VI compounds and demonstrated the feasibility of preparing ZnO/$CuInSe_2$ heterojunction solar cells entirely by spray pyrolysis with efficiencies exceeding 2% [41]. Nevertheless research into the development of novel approaches to this process for the deposition of good quality thin films of CdS, (Cd,Zn)S, CdSe, Cd(S,Se), CdTe, Cu_xS, and transparent oxide semiconductors, namely SnO_x, In_2O_3:Sn, ZnO as well as copper ternaries such as $CuInS_2$ and $CuInSe_2$ have been continued actively.

Spray pyrolysis has been successfully applied to the growth of thin films of CdSe and Cd(S,Se) solid solutions by Fiegelson at al [28]. They were concluded that ; the change in the lattice parameters follows Vegard's law with increasing sulphur content, the optical band gap varies from that of CdSe to that of CdS with the variation of composition, the resistivity of the films does not change significantly with composition but is influenced strongly by the substrate temperature and spraying and cooling rates.

CdS films, undoped and doped with Al, Cu, and Fe were prepared by the spray pyrolysis technique. The films have a polycrystalline hexagonal structure as shown from their XRD patterns [42]. The crystallinity of pure CdS film is highly distorted by the addition of Al, or Fe, or Cu. The A.C. photoconductivity for the prepared samples was measured. The photo-conductivity response spectra show two distinct peaks independent of the incorporated element. The position and intensity of these peaks are affected by the type and concentration of the elements incorporated. The optical absorption coefficient for the samples investigated, as calculated from transmission and reflection spectra, was studied as a function of photon energy [43]. The pure CdS sample shows a sharp absorption edge while the incorporated films show a less sharp curve. The incorporation of Al enhances the d.c. photosensitivity response.

The investigation of sprayed CdS film optical transmission and reflection at 510 nm wavelength is here reported. It is shown that the two properties are both insensitive to the film thickness at this irradiation frequency close to the material band gap [44]. From these results, it is analytically demonstrated that the optical absorption coefficient behaves as an hyperbolic function versus film thickness near the deposition substrate. A relationship is established between this optical behaviour and the film carrier density whose value is supposed to vary due to the migration of some metallic elements during the deposition process from the bulk to the surface of the film substrate. [45].

The chemical spray process has been used successfully for inorganic films and to deposite a great many compounds of CdS, CdSe, ZnS, ZnSe, CdZnS and Cu_2S by R.R. Chamberlin and J.S. Skarman [26]. They showed that the semiconductor characteristics of a spray deposited film are most dependent on the solution composition, substrate temperature, and the crystallinty of the substrate. Parameters such as spray rate, solution concentration, and the substrate thermal environment are the parameters which are adjusted such that a physically uniform film results. The crystallinity of the spray deposited film is dependent on the substrate and the starting material, particularly the cation material such as cadmium chloride or cadmium acetate in a cadmium thiourea solution [31].

A complete range of solid-solution films has been prepared by spray pyrolysis for the CdS_xSe_{1-x} and $Zn_xCd_{1-x}S$ systems by R.S.Feigelson at all [28]. The composition of the sprayed films were compared with the composition of the spraying solution and correspondence plots were given by these researchers. And also they showed that the large variation in resistivity with x in the $Zn_xCd_{1-x}S$ system appears to be only incidentally dependent on the method of preparation [33].

The effects on the electrical properties of heat treatment in H_2 of $Cd_{1-y}Zn_yS$ ($0 \leq y \leq 0.15$) and In doped CdS spraying films were studied and also the influence of Zn concentration on the layer physical properties were investigated by A.Mzerd, D. Sayah and at all [46]. It is found that the electrical and physical properties change remarkably when the Zn concentration increases. When crystallization is modified, the activation of the donor levels and the dark resistivity increase. After annealing, the resistivity decreases by about orders of magnitude for all analyzed samples. This reduction is due to an increase in carrier concentration and Hall mobility and the removal of chlorine and oxygen from the grain boundaries.

H.L.Kwok and W.C.Siu have made a careful study of the electronic properties of chemically sprayed cadmium sulphide films using thermoelectric and photothermoelectric effects [39]. The film properties were very dependent on the thickness. Although both the thick and the thin films had high carrier concentrations, the dark mobility varied significantly for films of different thicknesses. The grain size in the films depended on the film thickness even though the spray rate was kept constant. They suggested that chemisorption of gases can be responsible for the low mobility observed in the thin films. This is supported by the observed increase of the dark mobility when the thin films were heat treated in a nitrogen atmosphere and also by the gradual decrease of the dark mobility when the films were exposed to the atmosphere [40].

The demand for the fabrication of low cost terrestrial solar cells has recently enhanced the interest in the preparation and the purification of semiconductors by electrodeposition techniques, since these are extensively used in industrial production as an inexpensive method of large scale thin film deposition [47]. Electrodeposition has been successfully employed in the preparation of many elemental and compound semiconductors in thin film form, with most of the effort being put into Ge, and Si elemental semiconductors, CdS, CdSe, CdTe, ZnSe, and ZnTe II-VI compounds; GaAs, GaP, InP.

With the progress in the electrodeposition process for CdS and CdTe thin films and the insight into the devices made with them in the joint work carried out between the University of California and Monosolar Inc (USA) over the last twentyfive years, efficiencies of up to 10% have been achieved [48,49].

The application of electrodeposition in the preparation of layers of these particular semiconductors has gained considerable interest, since Bhattacharya's first attempt in 1983 [50]. However, most of the studies so far have been limited to the preparation and characterization of thin films of these semiconductors and only a few attempts have been made to fabricated solar cells based on them. In simple terms, electrodeposition is the process by which suitable materials are deposited on electrically conducting substrates by the action of an electric current.

M. Tomkiewicz at all have studied on electrodeposited n-CdSe thin films [51]. They have described the mechanisms for galvanostatic electrodeposition of CdSe in terms of competition between chemical reactions that lead to Se formation and electrochemical reduction of Se as polyselenide, at the interfaces between selenium and selenide. This mechanism leads to a cauliflower morphology for the resulting thin film. They were showed that; (1) high efficiency and relatively stable photoelectrodes can be formed by galvanostatic cathodic electrodeposition of CdSe, (2) the complex chemical and electrochemical deposition mechanisms give rise to a film morphology well suited for liquid junction solar cells, (3) the impedance of the electrodes is completely dominated by this morphology, while the optical and photovoltaic properties are not, (4) absorved metal ions as Zn, Ru, and Ga strongly influence the dark current, presumably through their catalytic activity in the hydrogen evolution reaction.

The electrodeposition method has also been studied extensively by S.K.Das and his co-workers for photovoltaic applications [52]. They have studied cadmium telluride-based solar cells which are one of the promising photovoltaic devices for low-cost large area terrestrial application. Cadmium telluride-based solar cells have been prepared as indium tin oxide (ITO)/SnO_2/CdTe and indium tin oxide/SnO_2/CdS/CdTe structures where CdS and CdTe were prepared by an electrodeposition technique by S.K.Das and his co-workers.

In this study, current–voltage measurements were carried out by using a computer controlled system with a 300W Oriel simulator set to produce 1000Wm^{-2} AM1 radiation using a cell calibrated at the U.S. Solar Energy Research Institute [25,52].

Efficient CdTe-based polycrystalline solar cells have been fabricated as CdS/CdTe, (ITO)/CdTe, TO/CdTe, ZnO/CdTe etc. Among the different techniques of producing cadmium telluride material, electrodeposition is one of the most suitable low-cost methods that can produce over 10% efficient CdS/CdTe solar cells [53]

In recent years, there has been an increasing interest in the preparation of device quality ZnS films for applications. ZnS is a wide band gap (3.70 eV) material that finds applications in light emitting diodes, electroluminescent displays, multilayer dielectric filters, optical phase modulation systems in integrated optics, etc. ZnS thin films have been fabricated by electrodeposition method by T. Mahalingam and his co-workers. The depositions were carried out potantiostatically in a three-electrode system. During film deposition, the solution pH was maintained at 2.5 using sulphuric acid [54].

n-CdSe, in either single crystal or thin film form, is a material that has been studied for application in solar cells, with a band gap of 1.7 eV by S.Eriksson at all [55]. n-CdSe is an attractive candidate as a photoconductors, thin film transistors, and gamma ray detectors. Diverse methods have been used to make CdSe: electrodeposition, evaporation, molecular beam deposition, spray pyrolysis, sputtering, and several crystal growing techniques.

Among them electrodeposition techique is one of the most suitable and low-cost method for the preparation of CdSe thin films. Doped CdSe thin films were electrodeposited onto indium-tin-oxide (ITO) substrates by H. Wynands and et all [56]. Hall effect and resistivity measurements were performed to determine the effects of doping on the resistivity, carrier concentration, and carrier mobility. The electrical resistivity were measured in the range of $1x10^5\Omega$-cm and, carrier concentration ranged from 10^{19} to $10^9 cm^{-3}$. Hall effect mobilities were in the range of 1-50 $cm^2/Vsec$. They showed that, as doping levels increased, both resistivity and mobility decreased [56].

Thin films of cadmium sulfide (CdS) are widely used in thin film solar cell applications as n-type window layers. They are used primarily in CdTe and $CuInSe_2$ (CIS) devices. Two device configurations can be employed. Firstly, the CdS may be deposited onto a CdTe or CIS layer on a metal substrate (either bulk or thin film) followed by the deposition of a conductive transparent oxide layer. Secondly, the

CdS may be deposited onto a glass substrate with a transparent oxide coating after which the CdTe or CIS is deposited on top. This followed by the application of a conducting contact layer [57].

Cadmium sulfide (CdS) thin films have been deposited by electrodeposition using the potentiostatic method on ITO-coated glass substrates from aqueous solution containing $CdCl_2 2H_2O$ and $Na_2S_2O_3$ at 90 ^{0}C by G.Sasikala and his co-workers. The deposition were carried out for various cathodic potentials. Good quality films were obtained at a cathodic potential of –0.6V. Voltammograms have been recorded to optimize the co-deposition region of CdS on ITO-coated glass substrates at 90^{0}C. Diffarction peaks for the film deposited at –0.5V, -0.6V and –0.7V occur at $2\theta=24.65^0$, 26.35^0, 28.1^0 corresponding to the (100), (002) and (101) reflections of hexagonal phase (wurtzite) observed in the X-ray diffraction spectra. The observed band gap is 2.61±0.015 eV [58].

Epitaxial growth of CdSe has been achieved on GaAs(111) by electrodeposition from an aqueous electrolyte by H.Cachet and his co-workers [59]. The quality of epitaxy has been investigated by reflection high energy electron diffraction, transmission electron microscopy and X-ray diffraction techniques. In this study, cadmium selenide was cathodically deposited in a three electrode cell from an acid solution containing 0.2 M $CdSO_4$ and various amounts of selenious acid. The pH was adjusted to 2.2 and the temperature maintained at 80^{0}C. The working electrode potential was monitored by a potentiostat and measured against a saturated mercurous sulfate electrode. It has been demonstrated that epitaxial of CdSe on GaAs can be grown in the liquid phase by an electrodeposition process, despite a large mismatch.

R.P. Silberstein and M. Tomkiewicz have carried out the first spectroscopic study of polycrystalline electrodeposited CdSe photoelectrodes. CdSe films 5-10μ in thickness were electrodeposited on titanium substrates galvanostatically in an electrolyte consisting of 0.03 M SeO_2, 0.1 M $CdSO_4$, and 0.5 M H_2SO_4. The PL spectrum of CdSe thin films have been shown to be quite sensitive to annealing procedures and subsequent surface treatment. Donor-acceptor-pair (DAP) bands have been identified at 77 K which are individually characteristic of un aged, dark-aged, and light-aged CdSe films. At 4.2 K, spectral lines they associate with bound-exciton recombination appear to be characteristic of un aged dark-aged electrodes, but differ from those of light-aged electrodes [60].

The electrodeposition method has also been studied extensively S.J. Lade and his co-workers [45]. Cadmium selenide thin films were cathodically electrodeposited from analytical 0.05 M $CdSO_4$ and 0.01 M SeO_2 solutions onto stainless steel and fluorine-tin oxide coated glass substrate. The pH of the electrolyte was adjusted to 3 with concentrated H_2SO_4 using a Labindia µp controlled pH analyser.

The electrodeposition potentials were estimated from polarization curves. All potentials were measured with respect to a saturated calomel electrode (SCE). The CdSe films have been characterized by X-ray diffraction, scanning electron microscopy and optical absorption. X-ray diffraction spectra showed that CdSe is polycrystalline with single hexagonal phase [61]. The intensity of the (002) peak increases remarkably by annealing in nitrogen atmosphere. Optical absorption studies showed that the bandgap of the CdSe is 1.70 eV. It is observed that the conductivity of the CdSe films increases by annealing in nitrogen atmosphere. From photoelectrochemical studies it is also seen that CdSe thin film is an n-type material [62,63].

Films of (Zn,Cd)Se and ZnSe were electrodeposited galvanostaticly from dimethylsulfoxide solutions of elemental Se the perchlorates of Zn and Cd by D.Gal and G.Hodes [64]. The composition of the mixed selenides could be controlled by variation of the deposition current density, utilizing diffusion control of the low concentrations of $Cd(CIO_4)_2$. The film composition was measured by X-ray photoelectron spectroscopy and compared with the measured bandgap values extracted from optical transmission spectra. Photoelectrochemical photocurrent spectroscopy and contact potential difference measurements both showed changes in apparent conductivity type with Zn concentration in the electrolyte from “n-type” (low Zn) concentration to “p-type” (high Zn).

G. Riveros and his co-workers have been grown ZnSe thin films on ITO glass substrate by electrodeposition method. ZnSe thin films were electrodeposited the potentiostaticly growth from solutions containing 0.2 M $ZnSO_4$ and 10^{-4}-10^{-3} M SeO_2 in deionized water and pH was adjusted to 2.4 by sulfuric acid addition. They have studied on film composition by X-ray diffraction, scanning electron microscopy and photo electrochemical data. Optical measurements were done on these samples which gave a clear band edge near 2.6 eV quite close to the accepted room temperature value of 2.7 eV for ZnSe [65].

SEMICONDUCTORS

2.3. Semiconductors

2.3.1. Introduction

The term “ semiconductor ” is defined as a rather poor conductor where the conductivity may be changed radically by small changes in its physical condition. Semiconductors are an important class of material both for industrial use and for scientific study. Over the last two decades, semiconductors have come to be used in a wide range of electronic devices, such as transistors, switching devices, voltage regulators, photocells, and photodetectors.

2.3.2. Semiconductor Materials

Semiconductors are a group of materials having electrical conductivities intermediate between metals and insulators. It is significant that the conductivity of these materials can be varied over wide ranges by changes in temperature, optical excitation, and impurity content. This variability of electrical properties makes the semiconductor materials natural choices for electronic device investigations [66]. Semiconductor materials are found in column IV and neighboring columns of the periodic table as shown in Table 2.1.

The column IV semiconductors, silicon and germanium, are called elemental semiconductors because they are composed of single species of atoms. In addition to the elemental materials, compounds of column III and column V atoms, as well as certain combinations from II and VI, make up the intermetallic, or compound, semiconductors. As Table 2.1 indicates, there are numerous semiconductor materials.

Table 2.1 Common semiconductor materials: (a) the portion of the periodic table where semiconductors occur; (b) elemental and compound semiconductors

(a)	II	III	IV	V	VI
		B	C		
		Al	Si	P	Se
	Zn	Ga	Ge	As	Se
	Cd	In	Sn	Sb	Te
(b)	Elemental	IV compounds	III-V compounds		II-VI compounds
	Si	SiC	AlP		ZnS
	Ge		AlAs		ZnSe
			AlSb		ZnTe
			GaP		CdS
			GaAs		CdSe
			GaSb		CdTe
			InP		
			InAs		
			InSb		

Among these, Si is used for the majority of semiconductor devices; rectifiers, transistor. The compounds are used most widely in devices requiring the emission or absorption of light. Fluorescent materials such as those used in television screens usually are II-VI compound semiconductors such as ZnS. Light detectors are commonly made with InSb, CdSe, or other compounds such lead salts PbTe and PbSe; Si and Ge are also widely used as infrared and nuclear radiation detectors. An important microwave device, the Gunn diode, is usually made of GaAs.

2.3.2.1. Crystal Structure

Solid materials are classified by the way the atoms are arranged within the solid. Materials in which atoms are placed randomly are called amorphous. Materials in which atoms are placed in a high ordered structure are called crystalline. Poly-crystalline materials are materials with a high degree of short-range order and no long-range order. These materials consist of small crystalline regions with random orientation called grains, separated by grain boundaries as seen in Figure 2.1.

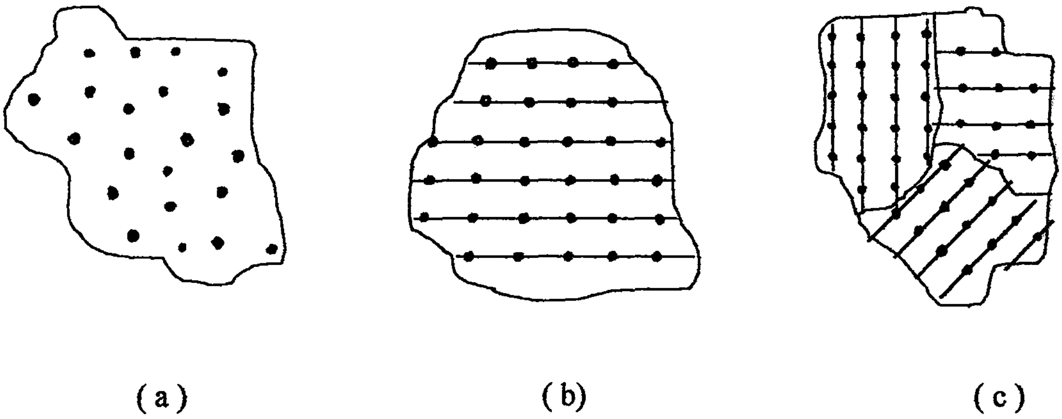

Figure 2.1 Three classes of solids, (a) Amorphous, (b) Crystalline, (c) Polycrystalline

Amorphous semiconductors are not expected to play an important role in microelectronics. For example, silicon dioxide that is an extremely important material in semiconductor technology, is also an amorphous solid. However, it is used as an insulator, because of its electrical conduction property.

In a crystalline solid, atoms are arranged in an orderly array that designs a periodic structure called lattice. It is possible to specify a unit cell which, when repeating itself, produces the crystalline solid. A unit cell contains complete information regarding the arrangement of atoms, and hence the unit cell can be used to describe the crystal structure.

In a polycrystalline solid, there are many small regions, each having a well-organized structure but differing from its neighboring regions. Such a material can be produced inexpensively and is used extensively in microelectronics [67].

2.3.2.2. Valence Band Model of Solids

In a crystal lattice, a positively charged nucleus is surrounded by negatively charged orbiting electrons in each constituent atom. If the atoms are closely packed, the orbits of the outer-shell electrons will overlap to produce strong interatomic forces. The outer electrons, i.e., valence electrons, are of primary importance in determining the electrical properties of the solid. In a metallic conductor such as aluminum or gold, the valence electrons are shared by all the atoms in the solid. These electrons are not bound to individual atoms and are free to contribute to the conduction of current upon the application of an electric field. In silicon, a crystalline semiconductor, each atom has four valence electrons to share with its four nearest-neighboring atoms as shown schematically in two-dimensional form in Figure 2.2.

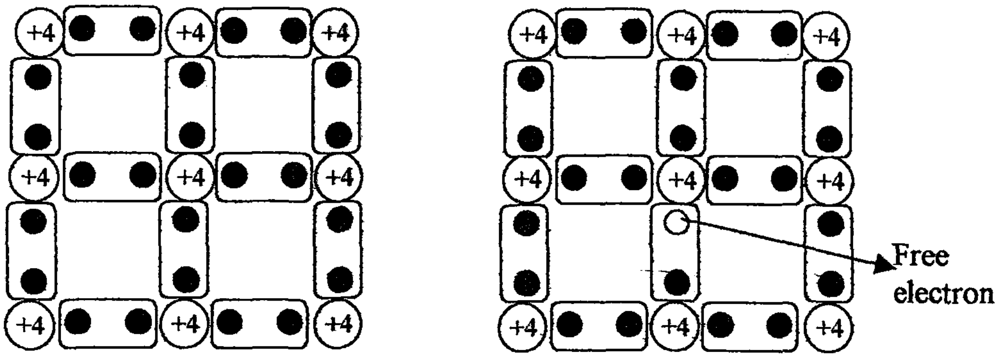

(a) Complete covelent band (b) Broken covalent band

Figure 2.2 A schematic configuration of two-dimensional form of atom which has four valence electrons

The valence electrons are shared in a paired configuration called a covalent bond. At low temperatures, these electrons are bound, and they are not available for conduction. At high temperatures, the thermal energy enables some electrons to break the bond, and the liberated electrons are then free to contribute to current conduction. Thus, a semiconductor behaves like an insulator at low temperatures and a conductor at high temperatures.

Whenever a valence electron is liberated in a semiconductor, a vacancy is left behind in the covalent bond, as shown in Figure 2.2 (b). This vacancy may be filled by one of its neighboring valence electrons, which would result in a shift of the vacancy location. One may then see the vacancy as moving inside the crystalline structure. As a result, this vacancy may be considered as a particle analogous to an electron. This particle is called a hole. It carries a positive charge and moves in the direction opposite that of an electron under an externally applied electric field.

2.3.2.3. Energy Band Model of Solids

As isolated atoms are brought together to form a solid, various interactions occur between neighboring atoms. The forces of attraction and repulsion between atoms will find a balance at the proper inter-atomic spacing for the crystal. In the process, important changes occur in the electron energy level configurations of the atoms, and these changes result in the varied electrical properties of solids.

When two atoms are completely isolated from each other so that there is no interaction of electron wave functions between them, they can have identical electronic structures. As the spacing between the two atoms becomes smaller, however, electron wave functions begin to overlap. The Exclusion principle dictates that no two electrons in a given interacting system may have the same quantum state; thus there must be a splitting of the discrete energy levels of the isolated atoms into new levels belonging to the pair rather than to individual atoms. This splitting of levels is important in the formation of molecules, such as H_2, as seen in Figure 2.3.

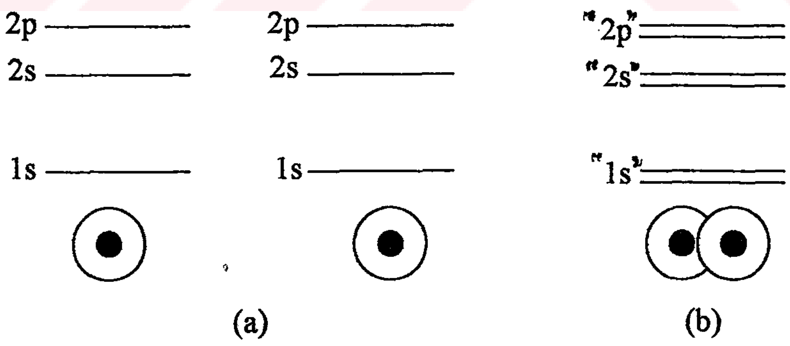

Figure 2.3 Energy level splitting in the diatomic hydrogen molecule: (a) isolated hydrogen atoms, (b) hydrogen molecule

In the hydrogen molecule, the two electrons can have opposite spins in an energy level lower than the atomic 1s level. This is the bonding state; a slightly higher level accounts for the antibonding state. The atomic 1s levels in effect split into two " 1s ". The quotation marks around "1s" indicate that the two split levels are no longer really 1s in nature; each differs slightly from 1s to accommodate the two levels in the same region of space .

Electrons are allowed to reside within the energy bands but not between the bands of allowed energy states. This is no different from the case of the isolated hydrogen atom, where the electron can only occupy the allowed discrete energy levels. Thus, certain bands of allowed energy levels are separated by gaps of forbidden energies in which an electron can't exist. Each allowed energy band contains a limited number of states that can accommodate a definite number of electrons. In a semiconductor the valence electrons group together to occupy a band of energy levels, called the valence band. The next higher band of allowed energy levels, called conduction band is separated from the former by a forbidden gap of energy E_g. This physical picture, called an energy band diagram as shown in Figure 2.4, for three classes of solids [68].

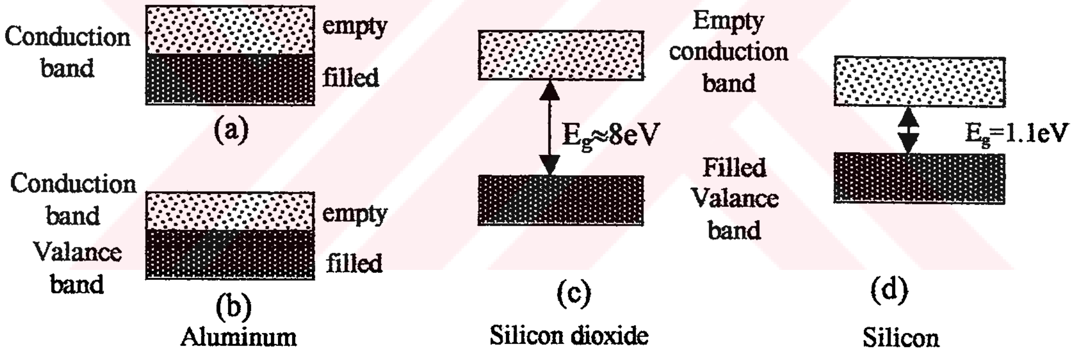

(a)
(b) Aluminum
(c) Silicon dioxide
(d) Silicon

Figure 2.4 Energy band diagrams for (a and b) metals, (c) insulator and (d) semiconductor at 0 K

In metals, the conduction band is only partially filled by electrons, as shown in Figure 2.4 (a), alternatively, the energy band diagram for a metal may be seen as in this Figure 2.4 (b), two bands which overlap so that there is no forbidden gap. In insulators, the lower band has just enough states in it to accommodate the number of valance band is completely filled, and the conduction band is empty as shown in Figure 2.4 (c). In a semiconductor, the forbidden gap energy E_g is not too large as shown in Figure 2.4 (d). For example: E_g=1.12eV in silicon and 1.43 ev in GaAs. Its forbidden energy is much smaller than that for an insulator but larger than that for a conductor. This corresponds to the not-so-light bonding of the valence electrons. At room temperature, some electrons in the valence band may receive enough thermal energy to overcome the forbidden gap and reach the conduction band. For each successful transition of a valence electron to the conduction band, a hole is left behind in the valence band. In other words, in the energy band picture, a hole is an unoccupied or empty energy level in the valence band. When an external electric field is applied, the electrons in the conduction band gain kinetic energy, which results in the flow electrons, or current conduction. At the same time the holes in the valence band also gain kinetic energy from the applied field. Thus, electrical conduction in a semiconductor may take place by two distinct and independent mechanisms; transport of negatively charged electrons in the conduction band and transport of positively charged holes in the valence band.

2.3.2.4. Impurities and Extrinsic Semiconductors

Solids are materials that are crystalline in form but not perfectly regular. The irregularities are called imperfections defects or faults. Imperfections are extremely important for the electrical and other transport properties as well as for the structural properties of solids. Basically, there are two general classes of irregularities by which real crystals differ from their idealized models, essential and nonessential imperfections. An essential imperfection is one that always exists regardless of how ideally the solid is prepared. Nonessential imperfections exist because the material can not be prepared with perfect regularity by imperfect men and machines. There are a few types of nonessential imperfections which are called point, line and plane imperfections.

2.3.2.5. Donor and Acceptors

When a semiconductor is doped with impurities, the semiconductor becomes extrinsic and impurity energy levels are introduced. Let us consider silicon and germanium, two elemental semiconductors. Both are in Group IV of the periodic table. The crystals of these elements have the diamond structure in which each atom is surrounded by four nearest-neighbour atoms at the corners of a tetrahedron. A two-dimensional representation of a pure crystal is shown in Figure.1.5(a). If a very small amount of a Group V element such as phosphorus, arsenic, or antimony is introduced into the crystal the lattice will not be significantly affected. The Group V atom will take its place in the lattice just as would another Group IV atom. But it has an extra electron above the number it needs to participate in the crystal bonds as shown in Figure 2.5(b). This extra electron is weakly bound to the impurity atom, for to leave it would mean creating a positive charge in the lattice. If the impurity atoms are sufficiently far apart, these extra, bound electrons form a set of localized states with energy levels just below the conduction band of the host semiconductor as shown in Figure 2.5(c). The Group V atoms are known as donor atoms, the new energy levels as donor levels, an the doped semiconductor is referred to as n-type.

Figure 2.5(d) shows what happens when a Group III element such as boron, aluminium, indium, or gallium is added to the lattice. The foreign atoms have one electron less than they need to complete the crystal bonds and so, effectively, there is a hole or a vacant electron state centred on each atom. The new acceptor levels are shown in Figure 2.5 (e). The Group III atoms are known as acceptor atoms and the doped semiconductor is said to be p-type.

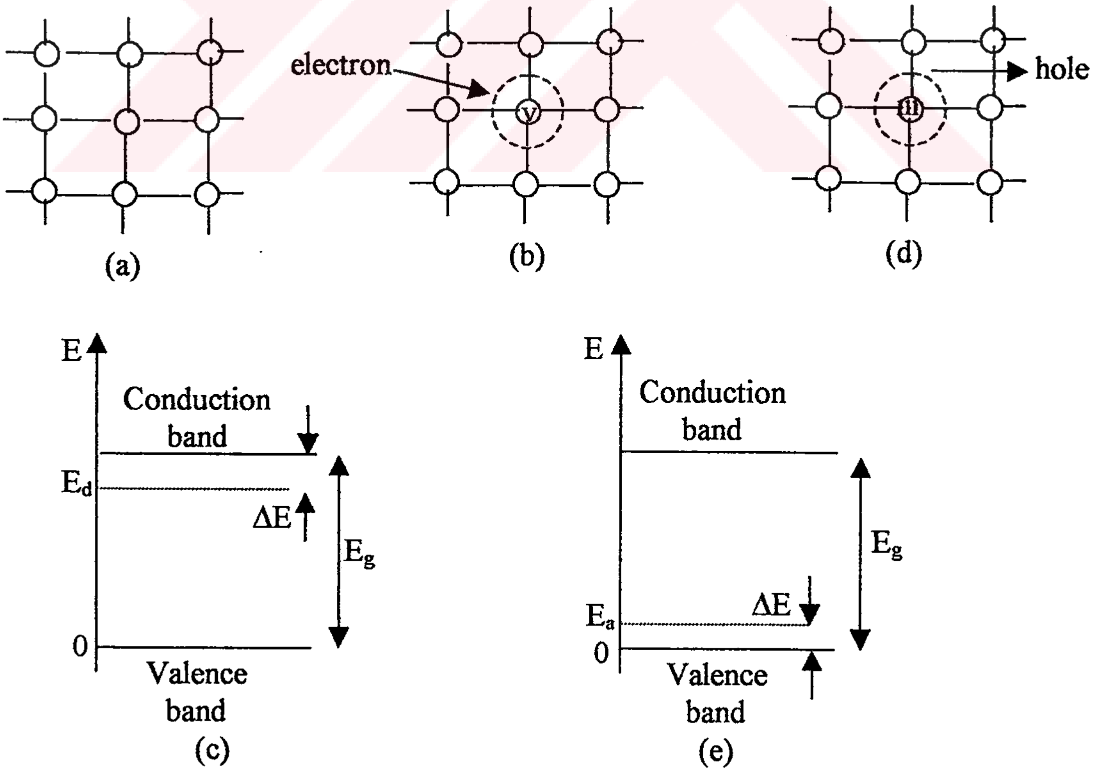

Figure 2.5 Impurities in semiconductors. Open circles represent the host atoms.

2.4. Electronic Transitions

2.4.1. Transitions

Some of the electronic transitions commonly found in photoconductors are shown schematically in the energy-band diagram of Figure 2.6. These transitions can conveniently be divided into three types: (1) absorption and excitation (Fig.2.6 (a)), (2) trapping and capture (Fig.2.6 (b)) and, (3) recombination and generation (Fig.2.6 (c)) [69].

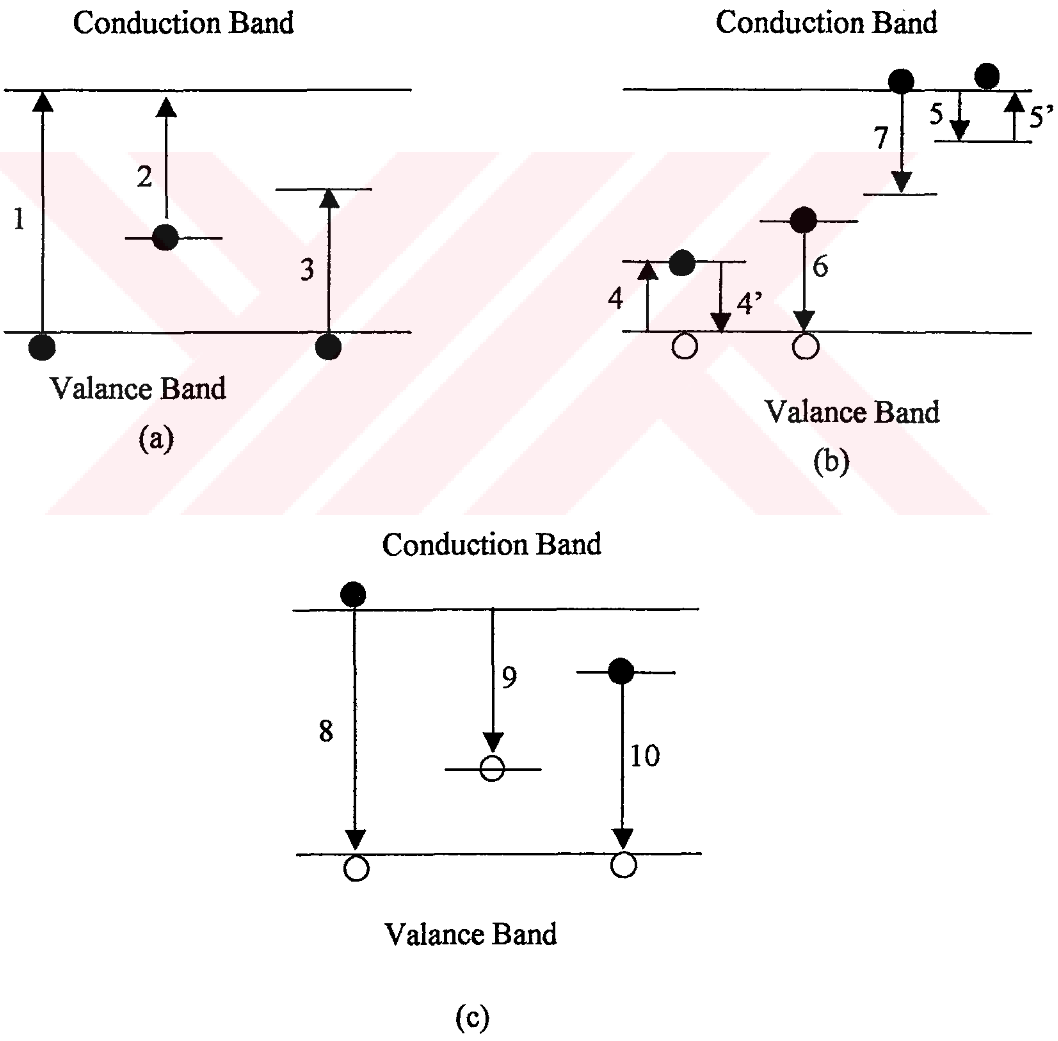

Figure 2.6. Common electronic transitions in photoconductors. (a) absorption and excitation, (b) trapping and capturing, (c) recombination.

2.4.2. Absorption and Excitation

There are three possible types of absorption transitions resulting in photoconductivity. Transition 1 corresponds to absorption by the atoms of the crystal itself, producing a free electron and a free hole for each photon absorbed. Transition 2 corresponds to absorption localized imperfections in the crystal, producing a free electron and a hole bound in the neighborhood of the imperfection for each photon absorbed. Transition 3 correspond to absorption, raising an electron from the valence band to an unoccupied imperfection level, producing a free hole and an electron bound in the neighborhood of the imperfection for each photon absorbed. We have omitted (a) resulting in excitation formation, (b) between the ground state and excited states of an imperfection and (c) within allowed bands since these transitions do not directly produce free carriers.

2.4.3. Trapping and Capture

It has been that transitions from trapping levels to near bands and vice versa are quite likely but there is far less probability of transition between trapping levels and distant bands. Thus as a trapping level gets further away from one band and closer to the other band, it reaches a point where there is an equal probability of transition to either band, although the probability in either case may be relatively low.

Trapping levels near to the valence band are generally refered to as hole-trapping centers since electrons in these levels may easily capture (trap) holes in the valence band. Trapping levels close to the conduction band are generally refered to as electron-trapping centers since these may easily capture electrons in the conduction band. As the center of the energy band is approached by trapping levels, we reach a region where is virtually equal probability of transition in either direction hence the centers can not be really named hole or electron trapping centers specially [69]. At these levels we may draw lines in the gap known as demarcation levels. Thus the upper line is the electron demarcation level and the lower line the hole demarcation level. These are shown in Figure 2.7.

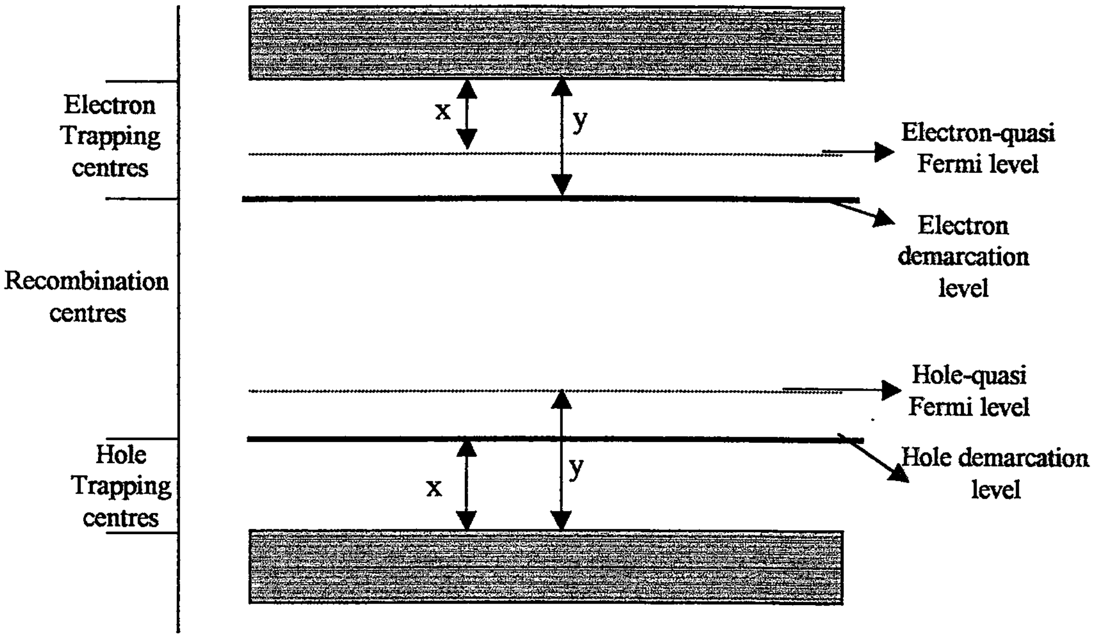

Figure 2.7 Demarcation levels and quasi-Fermi levels

Once electrons and holes have been freed by absorption of a photon of sufficient energy they will remain free until they are captured at an imperfection (omitting for the moment the alternative possibilities that they may recombine directly or pass out of the crystal at the electrodes). We may classify these capturing centers in two groups: (1) trapping centers, if the captured carrier has a greater probability of being thermally re-excited to the free state than of recombining with a carrier of opposite sign at the imperfection, (2) recombination center, if the captured carrier has a greater probability of recombining with a carrier of opposite sign at the imperfection than of being re-excited to the free state. Figure.2.6 (b) pictures trapping and thermal release of electrons in electron traps (transitions 5 and 5') and trapping and thermal release of holes traps (electron transitions 4 and 4') also capture of an electron (transition 7) and of a hole (electron transition 6) in recombination centers [70].

2.4.4. Recombination

Many semiconductor devices are based upon the principle of injection of holes into n-type material or injection of electrons into p-type material. Such injection carriers are called minority carriers to distinguish them from the majority carriers. These minority carriers will sooner or later recombine with the majority carriers and thus be permanently removed. In principle, such a recombination might take place in a single step according to the process;

free electron + free hole ⟷ electron bound

in valence band, but in many cases such a recombination occurs in a two step process involving recombination centers.

Three simple types of recombination transitions are pictured in Figure 2.6 (c) The free electron may combine directly with the free hole, according to transition 8; the probability of this transition is usually rather small. Frequently transitions of type 8 are radiative, i.e., the lost energy is emitted as photons with approximately the energy of the bang gap. Such emission is called edge emission.

Recombination may also occur, as is the more usual case, through recombination centers: either an electron being captured by an excited center containing a hole (transition 9) or hole being captured by an excited center containing an electron (transition 10). Transition 9 and 10 may also be radiative. A recombination center is a center that can act as an electron trap when empty and as a hole trap when filled. Let holes be injected into n-type material a hole trap; in the trapping process the electron combines with the free hole, with release of the excess energy, thus leaving the center empty. The center can now act as an electron trap; in the trapping process an electron from the conduction band makes a transition to the empty center with release of the excess energy [71].

2.5. Excess Carriers in Semiconductors

2.5.1. The Fundamental Absorption Process

Most semiconductor devices operate by the creation of charge carriers in excess of the thermal equilibrium values. These excess carriers can be created by optical excitation or electron bombardment, i.e. The most important absorption process involves the transition of electron from the valence to the conduction band as shown in Figure 2.8. Because of its importance, the process is referred to as fundamental absorption. In fundamental absorption, an electron absorbs a photon (from the incident beam) and jumps from the valence band into the conduction band. The photon energy must be equal to the energy gap or larger. The frequency must therefore be

$$\nu > \left(E_g / h \right) \tag{2-1}$$

The frequency $\nu_0 = E_g/h$ is referred to as the absorption edge frequency.

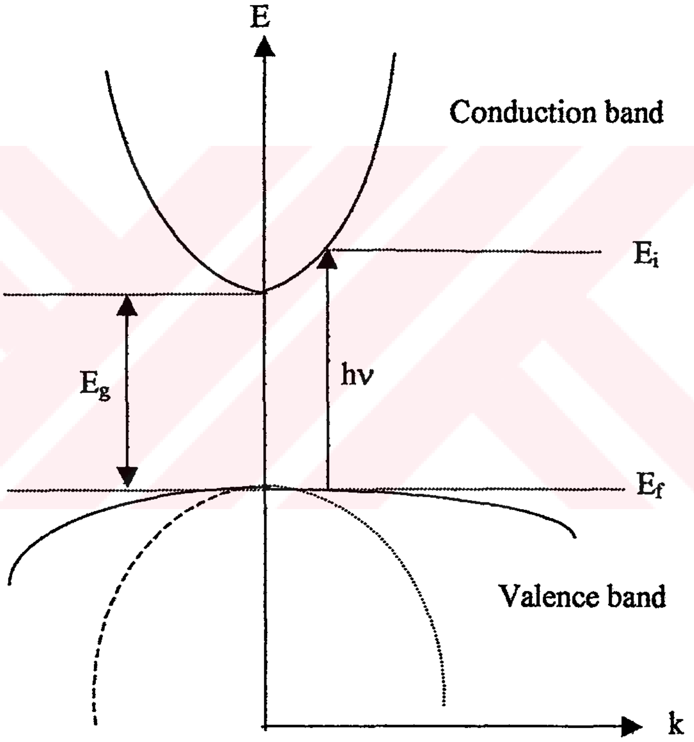

Figure 2.8 The fundamental absorption process in semiconductors (Direct transition, E_i (initial), E_f (final))

In the transition process (photon absorption), the total energy and momentum of the electron-photon system must be conserved. Therefore

$$E_f = E_i + h\nu \tag{2-2}$$

where E_i and E_f are the initial and final energies of the electron in the valence and conduction bands, respectively,

The absorption process occurs in the so-called direct-gap semiconductors. This process is called as direct transitions. In a direct transition, the absorption coefficient (α) is given by following emission spectrum and α is the function of hv

$$\alpha(h\nu) = A(h\nu - E_g)^{1/2} \tag{2-3}$$

where E_g is the energy gap and A is a constant involving the properties of the bands that is given by

$$A = \frac{2q^2 \left(m_r^*\right)^{3/2}}{nch^2 m_e^*} \tag{2-4}$$

where m_r^* is the reduced mass: $1/m_r^* = 1/m_e^* + 1/m_h^*$, n is the diffraction plane, h is the Plank's constant and c is the light speed.

Here the bottom of the conduction band lies at k=0, and hence directly above the top of the valence band.

2.5.2 Optical Absorption

An important technique for measuring the band gap energy of a semiconductor is the absorption of incident photons by the material. In this experiment photons of selected wavelength are directed at the sample, and the relative transmission of the various photons is observed. Since photons with energies greater than the band gap energy are absorbed while photons with energies less than band gap are transmitted, this experiment gives an accurate measure of the band gap energy.

2.5.3. Transmission and Absorption

It is apparent that a photon with energy $h\nu \geq E_g$ can be absorbed in a semiconductor as shown in Figure 2.9. Since the valence band contains many electrons and the conduction band has many empty states into which the electrons may be excited, the probability of photon absorption is high. As Figure 2.9 indicates, an electron excited to the conduction band by optical absorption may have more energy than is common for conduction band electrons (almost all electrons are near E_c unless the sample is very heavily doped).

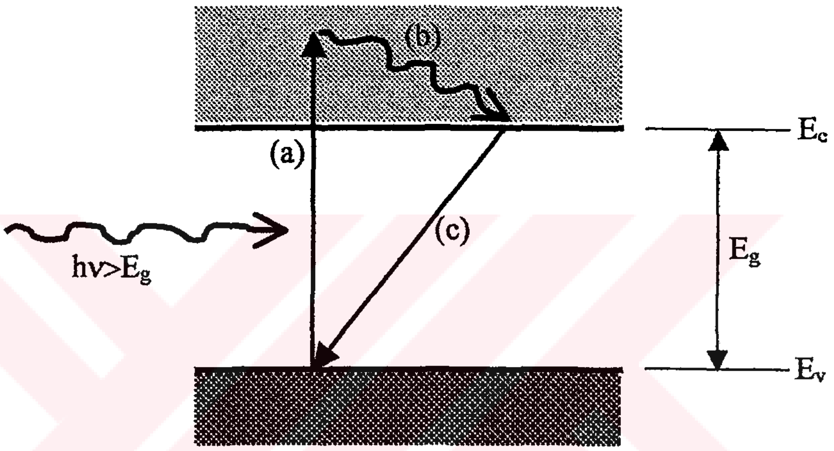

Figure 2.9 Optical absorption of a photon with $h\nu > E_g$: (a) an EHP is created during photon absorption, (b) the excited electron gives up energy to the lattice by scattering events, (c) the electron recombines with a hole in the valence band.

Thus the excited electron losses energy to the lattice in scattering events until its velocity reaches the thermal equilibrium velocity of other conduction band electrons. The electron and hole created by this absorption process are excess carriers; since they are out of balance with their environment, they must eventually recombine. While the excess carriers exist in their respective bands, however, they are free to contribute to the conductivity of the material.

A photon with energy less than E_g is unable to excite an electron from the valence band to the conduction band. Thus in a pure semiconductor, there is negligible absorption of photons with $h\nu < E_g$. One exception to this rule is that a small amount of absorption can occur within a given band (free carrier absorption); for example, a low energy photon can excite a conduction band electron temporarily to a higher state within the conduction band. No excess carriers are created in this process. This component of absorption is usually negligible compared with band-to-band excitation (intrinsic absorption) by photons of higher energy, and most photons with $h\nu<E_g$ are transmitted through the material. This explains why some materials are transparent in certain wavelength ranges.

2.5.4. Absorption Coefficent and Band Gap

If a beam of photons with $h\nu>E_g$ falls on a semiconductor, there will be some predictable amount of absorption, determined by the properties of the material. We would expect the ratio of transmitted to incident light intensity to depend on the photon wavelength and the thickness of the sample. To calculate this dependence, let us assume that a photon beam of intensity I_0 (photons/ cm^2-sec) is directed at a sample of thickness L as shown in Figure 2.10. The beam contains only photons of wavelength λ, selected by a monochromator. As the beam passes through the sample, its intensity at a distance x from the surface can be calculated by considering the probability of absorption within any increment dx. Since a photon which has survived to x without absorption has no memory of how far it has traveled, its probability of absorption in any dx is constant. Thus the degradation of the intensity $-dI(x)/dx$ is proportional to the intensity remaining at x

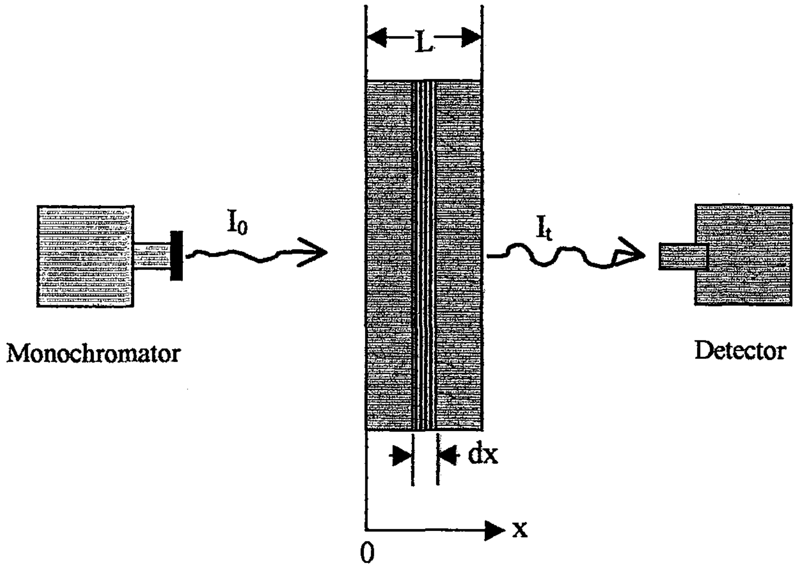

Figure 2.10 Optical absorption experiment

$$-\frac{dI(x)}{dx} = \alpha I(x) \tag{2-5}$$

The solution to this equation is

$$I(x) = I_0 e^{-\alpha x} \tag{2-6}$$

and the intensity of light transmitted through the sample thickness L is

$$I_t = I_0 e^{-\alpha L} \tag{2-7}$$

The coefficient α is called the absorption constant and has units of cm^{-1}. This coefficient will of course vary with the photon wavelength and with the material.

In most cases, the on set of absorption at the band gap is sharp, and a reasonable measurement of E_g can be obtained for wide band gap semiconductors by using the eye as a detector in Figure 2.10. As the monochromator is varied from long to short wavelengths, light will be transmitted through the semiconductor until absorption begins at a fairly well-defined wavelength. Of course, for more accurate measurement a detector must be used which provides an output proportional to light intensity.

Figure 2.11 indicates the band gap energies of some of the common semiconductors, relative to the visible, infrared, and ultraviolet portions of the spectrum. We observe that GaAs, Si, Ge, and InSb lie outside the visible region, other semiconductors, such as GaP and CdS, have band gaps wide enough to pass photons in the visible range. It is important to note here that a semiconductor absorbs photons with energies equal to the band gap, or larger.

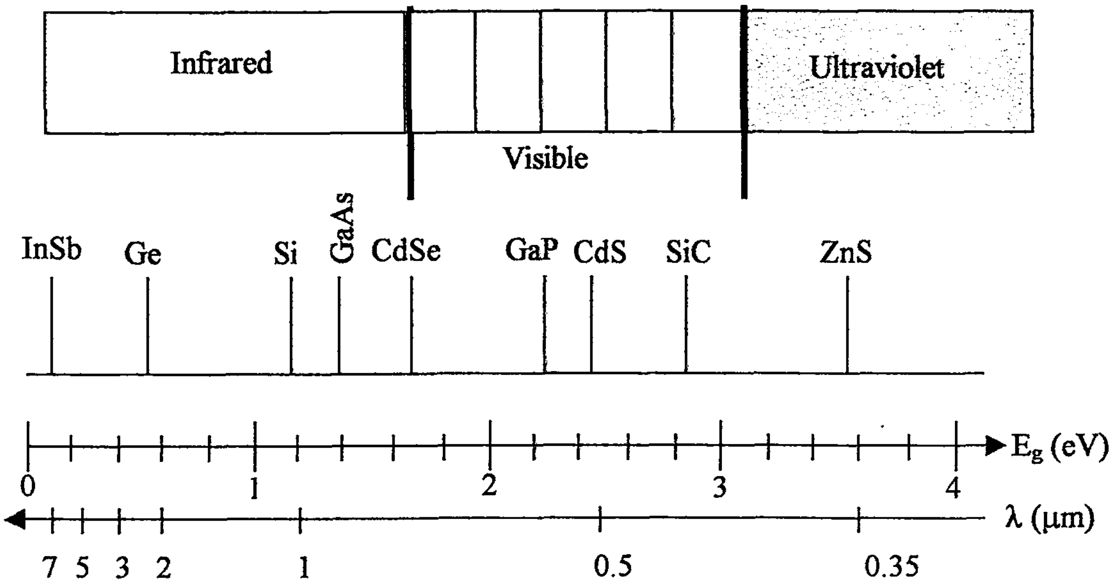

Figure 2.11 Band gaps of some common semiconductors relative to the optical spectrum

2.6. Hall Mobility

The importance of the Hall effect is under scored by the need to determine accurately carrier density, electrical resistivity, and the mobility of carriers in semiconductors. The Hall effect provides a relatively simple method for doing this. Because of its simplicity, low cost, and fast turn around time, it is an indispensable characterization technique in the semiconductor industry and in research laboratories.

The history of the Hall effect begins in 1879 when Edwin H. Hall discovered that a small transverse voltage appeared across a current-carrying thin metal strip in an applied magnetic field. Until that time, electrical measurements provided only the carrier density-mobility product, and the separation of these two important physical quantities had to rely on other difficult measurements. The discovery of the Hall effect removed this difficulty. Development of the technique has since led to a mature and practical tool, which today is used routinely for testing the electrical properties and quality of almost all of the semiconductor materials used by industry.

The basic physical principle underlying the Hall effect is the Lorentz force. When an electron moves along a direction perpendicular to an applied magnetic field, it experiences a force acting normal to both directions, and moves in response to this force and the force effected by the internal electric field. For an n-type, bar-shaped semiconductor shown in Figure 2.12, the carriers are predominately electrons of bulk density n.

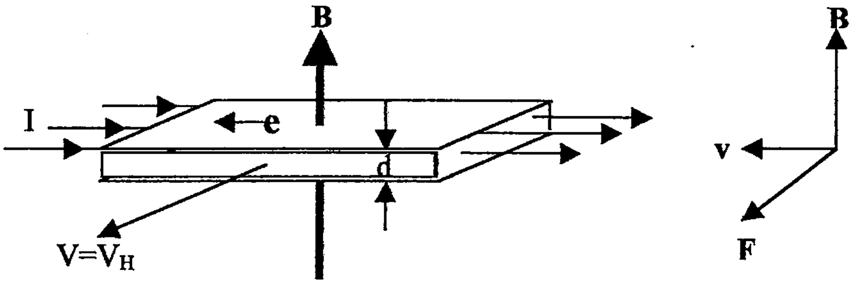

Figure 2.12 The Hall effect measurement set up.

We assume that a constant current I flows along the x-axis from left to right in the presence of a z-directed magnetic field. Electrons subject to the Lorentz force initially drift away from the current flow line toward the negative y-axis direction, thus resulting in an excess surface electrical charge on the side of the sample. This excess surface charge results in the Hall voltage, a potential drop across the two sides of the sample. (Note that the force on holes is toward the same side because of their opposite velocity and positive charge.). This transverse voltage is the Hall voltage V_H and its magnitude is equal to IB/qnd, where I is the applied current, B is the applied magnetic field intensity, d is the sample thickness, and q (1.602×10^{-19} C) is the elementary charge [72].

In some cases, it is convenient to use layer or sheet density ($n_s = nd$) instead of bulk density. One then obtains the equation $n_s = IB/q|VH|$. Thus, by measuring the Hall voltage V_H and from the known values of I , B , and q , one can determine the sheet density ns of charge carriers in semiconductors. If the measurement apparatus is set up the Hall voltage is negative for n-type semiconductors and positive for p-type semiconductors. The sheet resistance R_S of the semiconductor can be conveniently determined by use of the Van der Pauw resistivity measurement technique. Since sheet resistance involves both sheet density and mobility, one can determine the Hall mobility from the equation

$$\mu = |V_H| / R_s IB = 1 / (qn_s R_s) \tag{2-8}$$

If the conducting layer thickness d is known, one can determine the bulk resistivity ($\rho = R_S d$) and the bulk density ($n = n_S/d$).

EXPERIMENTAL STUDIES:
FILM PRODUCTION TECHNIQUES

2.7. Spray Pyrolysis Method

2.7.1 Introduction

The spray pyrolysis technique (or solution spraying) for the growth of semiconducting films is a method of spraying a suitable solution mixture onto a heated substrate. It is a convenient and economical method for the deposition of such materials [31]. This technique is simply consisted of spraying a finely atomised solution onto a suitable hot substrate [33]. The substrate temperature has a great influence on the spraying of thin films. The spray nozzle which is used for strongly affects the spraying rate, the sprayed particle size and the spray distribution. In the spray pyrolysis process the uniformity of the droplet size is one of the primary requirments for a spray system. The chemicals contained in the spray solution are expected to fullfil the following conditions;

(i) The chemicals in the spraying solution provide species/complexes that will undergo a thermally activated chemical reaction to yield the desired thin film material,

(ii) the remainder of the constituents including the carrier liquid should be volatile at the substrate temperature

2.7.2 Experimental set-up of Spraying System

In this study, the apparatus which is used for the development of thin film samples based on the spraying pyrolysis technique was designed and developed in our laboratory [10]. A schematic block diagram of this apparatus is shown in Figure 2.13. This system consists of a spraying system, heater, temperature control system, and timer. The system is enclosed by a glass chamber .

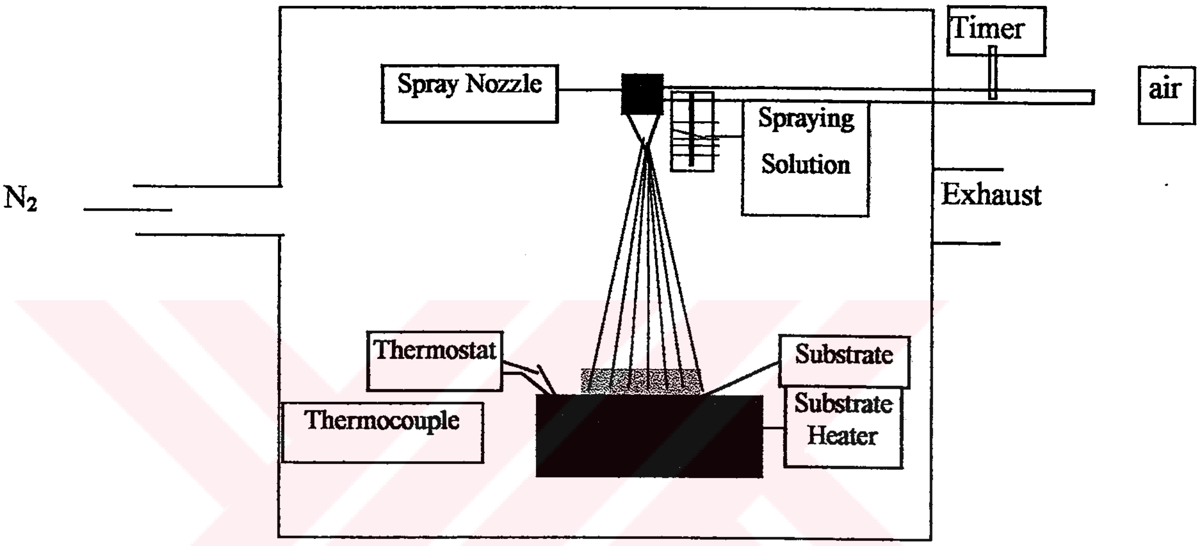

Figure 2.13 Schematic diagram of the spray pyrolysis system

Spraying system: This is used to produce the bubbles from the spraying solution.

Heater: This is used to heat the substrates. It consists of a steel plate with a resistance coil lying under it. The power of the heater is 2500 watts and it operates at 220 volts and 50 Hz (AC).

Temperature control system : A thermostat is used to keep the substrates at a required temperature.

Glass chamber: The spraying system and the heater are placed in a glass chamber and nitrogen gas is passed through it during the growth of thin film.

2.8 Growth Mechanism of Semiconducting Thin Films by The Spraying Pyrolysis Method

2.8.1 Introduction

General information about the spraying system and its apparatus was given and explained in the previous section. The spray pyrolysis technique for the production of semiconducting films is a method of spraying suitable solution mixtures onto a heated substrate. This method is convenient and economical method for the deposition of such materials. Several factors influence the proper peformance and the quality of semiconducting thin film produced by the spraying pyrolysis method.

These factors are as follows: (i) the properties of substrate, (ii) the substrate temperature, (iii) the spray nozzle, (iv) the uniformity of the droplet size of solution, (v) the flow rate of spraying solution, (vi) the height of the nozzle from the substrate surface.

2.8.2. Substrate Preparation

The physical properties of substrates on to which thin films is deposited, play a vital role in the growth of good quality thin film samples. The film properties are very strongly dependent on the crystal structure of substrate. The crystalline films can be deposited on a noncrystalline material such as glass, ceramic and mica. For example, a highly crystalline film obtained from the cadmium chloride ($CdCI_2$) - thiouria ($SC(NH_2)_2$) and zinc cloride ($ZnCI_2$) - thiouria ($SC(NH_2)_2$) solutions can be developed on an amorphous substrate.

In this study, glass is used as substrate for developing the thin film samples because of its cheapness when compared to other types of substrates. The preparation of a glass substrate is as follows; firstly, the glass substrates are cut into 1 cm^2 in size. Then cleaning process is applied to the glass substrate in four steps as seen in Figure 2.14.

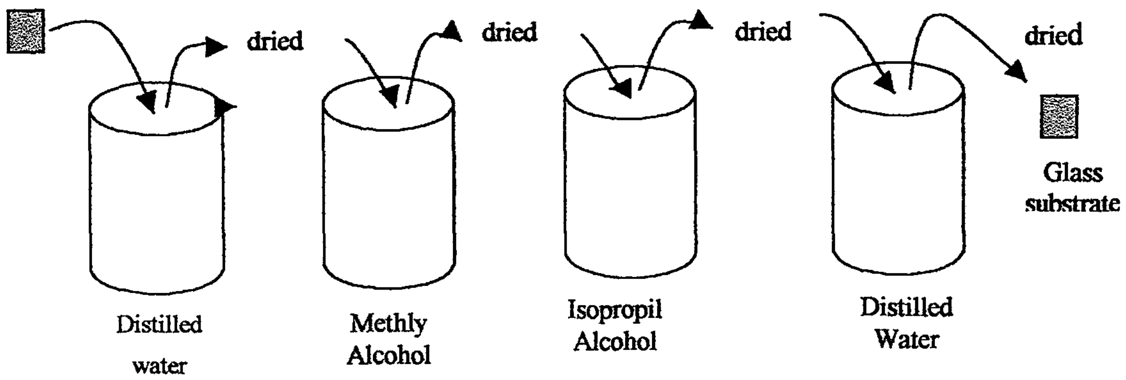

Figure 2.14 Cleaning process of the glass substrate

The cleaning process is as follows:

1- The glass substrate is immersed into the distilled water to clean the dust on its surface for 15 minutes. Then it is taken out from the distilled water and dried.
2- The substrate which is taken from the first cup is dried and it is immersed into the methyl alcohol and left there for 15 minutes to clean the oil substances on the surface of the substrate, and then it is taken out from this liquid and dried in air.
3- The dried substrate is immersed into the third cup filled with isopropil alcohol and it is treated again for 15 minutes to obtain a smooth surface.
4- Finally, the substrate is treated with the distilled water as in the first step to clean all the residues remaining on the surface of substrate during the other processes.

2.8.3. Spraying Solution Preparation

Different spraying solutions were prepared for the production of ZnSe, CdSe and, CdS thin films. The spraying solution is prepared for the production of ZnSe thin film as follow; firstly, the required amounts of $ZnCl_2$ and SeO_2 salts are weighed and stirred together into a cup containing the distilled water of 100 mlt to form the solution. A similar procedure is applied for the preparation of the spraying solution of ZnSe film and the spraying solution of CdSe. The spraying solution for the production of the CdS thin film was prepared as follows; firstly, the required amount of $CdCl_2$ and $SC(NH_2)_2$ (thiourea) salts are weighed and stirred together into a cup containing the distilled water of 100 mlt to obtain the solution. Different spraying solutions were used for the production of semiconducting CdS, CdSe and ZnSe thin films using the solutions having different composition.

2.8.4. Development of CdS Thin Film

To develop polycrystalline CdS thin film samples, firstly a 100 mlt spraying solution of $CdCl_2$ (0.05 moles/liter) and $SC(NH_2)_2$ (0.05 moles/liter) was used. The spray flow rate was adjusted to about 0.5 ml per min and the height of the nozzle was fixed to 20 cm from the substrate surface placed on the heater. Then the spraying solution was sprayed onto the glass substrate which was kept at the required temperature. When the solution droplets reach to the heated glass substrate surface, the following chemical reaction occurs,

$$CdCl_2 + SC(NH_2)_2 + 2H_2O \longrightarrow CdS + 2NH_4Cl + CO_2 \qquad (2\text{-}9)$$

As seen from this reaction, a CdS thin film is formed on the substrate surface while the NH_4Cl and CO_2 gases leave the system. The CdS thin films were developed at the different substrate temperatures of 340°C, 380°C and, 420°C. All spraying processes were carried out in air.

2.8.5 Development of CdSe Thin Film

To develop polycrystalline CdSe thin film samples, a 100 mlt spraying solution of $CdCl_2$ (0.05 moles/liter) and SeO_2 (0.05 moles/liter) was used. The spray flow rate was adjusted to about 0.5 ml per min and the height of the nozzle was fixed to 20 cm from the substrate placed on the heater. Then the spraying solution was sprayed onto the glass substrate which was kept at the required temperature. When the solution droplets reach to the heated glass substrate surface, the following chemical reaction occurs,

$$CdCl_2 + SeO_2 + H_2O \longrightarrow CdSe + 2HCl + (3/2)O_2 \qquad (2\text{-}10)$$

As seen from this reaction, a CdSe thin film is formed on the glass substrate surface. The CdSe thin films were developed at the different substrate temperatures of 380^0C, 400^0C and, 420^0C. All spraying processes were carried out in air.

2.8.6. Development of ZnSe Thin Films

To develop polycrystalline ZnSe thin film samples, a 100 mlt spraying solution of $ZnCI_2$ (0.05 moles/liter) and SeO_2 (0.05 moles/liter) was used. The spray flow rate was adjusted to about 0.3 ml per min and the height of the nozzle was fixed to 20 cm from the substrate placed on the heater. Then the spraying solution was sprayed onto the glass substrate which was kept at the required temperature. When the solution droplets reach to the heated glass substrate surface, the following chemical reaction occurs,

$$ZnCl_2 + SeO_2 + H_2O \longrightarrow ZnSe + 2HCl + (3/2)O_2 \qquad (2\text{-}11)$$

As seen from this reaction, a ZnSe thin film is formed on the glass substrate surface. The ZnSe thin films were developed at the different substrate temperatures of 400^0C, 430^0C and, 450^0C. All spraying processes were carried out in air.

2.9. Growth Mechanism of The Semiconducting Thin Films by Electrodeposition Method

2.9.1. Introduction

General information about the electrodeposition system and its apparatus were given and explained step by step with the relation figures in section 3.8. Electrochemical deposition occurs when ions in a solution become part of the surface of an electrode by accepting electrons and becoming neutral. In this manner, metallic or semiconductor thin films can be deposited on an electrode by passing current through the solution. Several factors in electrodeposition process influence the proper performance and quality of the produced semiconducting and conducting thin films. These factors are as follows; (i) the properties of substrate, (ii) the composition of solution, (iii) current density, (iv) the pH value of solution, (v) deposition time, (vi) stiring rate, (vii) solution temperature, (viii) the applied potential or current during deposition process.

2.9.2. Preparation of The Substrate

All the II-VI compound ZnSe, CdSe and CdS semiconducting thin film samples were grown on to the nickel thin layer which is developed onto a copper plate. Nickel is a proper substrate because of its electrochemical passivity. Even a low potential is applied to a nickel electrode a little current passed through it. So that nickel is matched with semiconducting and conducting thin films better than other metals. Before the deposition of nickel thin layer onto a copper substrate some cleaning processes are applied as follow:

1- Copper plates are cut into 1x2 cm in dimension.
2- Copper plates are mechanically polished with a zero number emery paper.
3- The polished surface of the copper plates are washed a few times with distilled water.
4- Then, the copper plates are rinsed in the distilled water. In this way, its surface is freed from some kind of dirt and dusts.
5- Finally, the surfaces of the copper plates are dried with a dry paper.

At the end of the all these processes, the copper substrates were ready for the application of electrodeposition of nickel film.

2.9.3. The Development of The Nickel Thin Layer onto The Copper Plate

Firstly, a chemical solution was prepared by the required chemical salts ($NiSO_46H_2O$ and H_3BO_3) mixing with distilled water. To the this the required amounts of $NiSO_46H_2O$ and H_3BO_3 chemical salts of 6.5 gr and 1.2 gr respectively, were weighed and stirred into a cup containing the 50 mlt of distilled water to form the solution. The pH value of the solution was adjusted to 5 adding the concentrated sulfuric acid. After then, the electrodeposition process is applied using this solution (electrolyte) as follows: the deposition were carried out using a computer controlled potantiostat-galvanostat device.

A platinum plate and a copper plate were used as an anode and cathod, respectively. These electrodes were dipped vertically in the solution and the temperature of the bath was kept at room temperature. The nickel thin film layer was cathodically deposited onto the copper plate using an 18 mA constant current for 5 minutes.

2.9.4. Deposition of CdS Thin Film onto Nickel Thin Layer by The Electrodeposition Method

Thin films of CdS were electrodeposited onto a nickel thin layer from the electrolyte containing $CdCI_2$ (0.5 M) as cadmium source and $SC(NH_2)_2$ (0.5 M) as a sulphur source. All of them were stirred in a cup contaning 50 mlt distilled water to form a solution. Then, the pH value of the solution was adjusted between 1.50-2.00 adding the concentrated suphuric acid droplets in to the solution. Finally, two electrodes are immersed into the solution as seen in Figure 1.15, and electrodeposition process was started.

During the deposition process, the temperature of the solution was maintained at $70^0C \pm 3$ and the chemical solution was stirred at 400 rpm using a magnetic stirrer-heater device. The deposition was carried out by using a potantiostat-galvanostat device. During the deposition, a current of 0.14 mA was applied. This kind of deposition is called as galvonastatic. The desired current was immediately applied upon insertion of the electrode into the chemical solution and the deposition time was maintained for 30 min.

The pH of the solution plays a major role in the electrolyte stability and, as well as the current density. When the pH is greater than 2, the solution becomes turbid and the current passing through the solution increases, therefore, the color of the CdS shifts from yellowish to dark-brown. When the pH is less than 1, the CdS thin film is insufficently grown onto the nickel substrate.

For this reason, the pH of the solution affects also the composition of electrodeposited thin films. So it is always better to have a pH value of the solution in the 1-2 range. When the solution temperature is increased, the deposition time is decreased and also, the deposition of thin film increases with increasing temperature, as polarization decreases.

During the deposition process, the positively charged Cd^{+2} and S^{+} ions are accelerated under the influence of the applied potential towards the cathodic electrode (working electrode). When the positive ions reach to the cathode they bond at the cathode by taking electrons from the nickel electrode, so that a CdS alloy film deposite in a yellowish colour form. And also during this process, an amount of hydrogen gas is formed therefore at least a part of the current which is passing through the electrolyte is used consumed in this hydrogen formation.

By taking into account the conditions given below, a good quality film of CdS can be deposited by the galvanostatic method.

i) pH : 1- 2.
ii) Deposition time: 30 - 60 min.
iii) Applied potential: 0,65 - 0,75 V.
iv) Current intensity: 0.14 mA.
v) Solution temperature: 70 - 75 ^{0}C.
vi) Stiring rate: 400 - 600 rpm.

2.9.5. Deposition of CdSe Thin Film onto The Nickel Thin Layer by The Electrodeposition Method

Semiconducting thin films of polycrystalline CdSe were grown onto a nickel thin layer by cathodic deposition. The CdSe thin films have been electrodeposited from a 30 mlt electrolyte containing the solutions of $CdCl_2$ (0.6 gr) salt and %10 SeO_2 (3mlt) . All of them was stirred into the distilled water to form a solution. Then, the pH range of the solution was adjusted to 2.00-2.30 using concentrated hydrochloric acid (HCl) which was added dropwise and then the temperature of the solution was maintained at 50-65^{0}C.

Two electrodes were immersed into the solution as seen in Figure 1.15. One of them is a carbon electrode used as an anode (counter electrode) and, the other is a nickel electrode used as a cathode (reference electrode). During the deposition process, the temperature of the solution was maintained at 60^0C ±3 and the chemical solution was stirred at 500 rpm using a magnetic stirrer-heater device. The deposition was carried out by using a potantiostat-galvanostat device.

During the deposition, the potential difference between the substrate with and the anodic electrode was kept constant at 0.50-0.55 V. This kind of deposition is called as potantiostatic deposition. The desired potential was immediately applied upon insertion of the electrode into the chemical solution and the deposition time was maintained for 60 min.

The pH of the solution plays a major role in the electrolyte stability and in the magnitude current density. When the pH is greater than 3, the solution becomes turbid and the current passing through the solution increases, therefore the color of the CdSe thin film was shifts from yellowish-brown to dark-brown. When the pH is less than 2, the CdSe thin film is insufficently grown onto the nickel substrate.

For this reason, the pH of the solution affects also the composition of electrodeposited thin films. So it is always better to have the pH of the solution liying in the 2-3 range. When the solution temperature is increased, the deposition time decreases, and also the deposition of CdSe thin film increases with increasing temperature, as the polarization decreases.

During the deposition process positively charged Cd^{+2} and Se^{+} ions are accelerated under the influence of the applied potantial towards the cathodic electrode (reference electrode). When positive ions reach to the cathodic electrode, they take two electrons from the nickel electrodes and they bond to it. Hence, CdSe alloy deposits as a yellowish-brown colour film.

And also during this process, an amount of hydrogen gas is formed therefore at least a part of the current passing through the electrolyte is used in this hydrogen formation.

To produce a good quality film of CdSe through the potentiostatic growth method, the following deposition conditions should be considered;

i) pH : 2.1, 2,6.
ii) Deposition time: 30 - 60 min.
iii) Applied potential: 0,55 - 0,60 V.
iv) Solution temperature: 60 - 65 ^{0}C.
v) Stiring rate: 400 - 600 rpm.

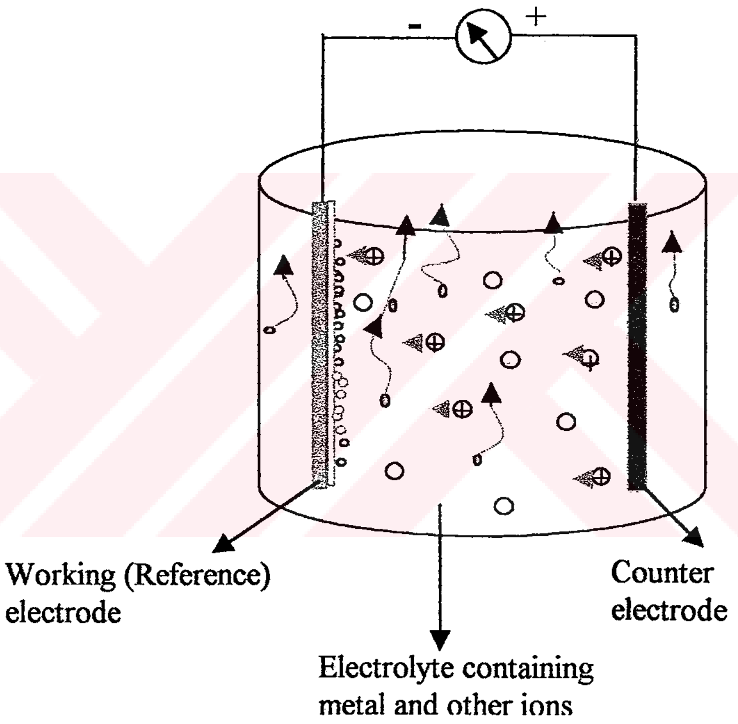

Figure 2.15. Schematic representation of a set-up for electrodeposition

2.9.6. Deposition of ZnSe Thin Film onto The Nickel Thin Layer by The Electrodeposition Method

To deposite the polycrystalline ZnSe thin film onto the nickel substrate, firstly, a chemical solution is prepared by using required chemical salts. The ZnSe thin film was grown from the solutions of $ZnSO_47H_2O$ (28.76 gr/liter for 0.1 M) and SeO_2

(%10) (0.00095 gr/liter for 10^{-5} M). All of them were stirred in the 45 mlt distilled water to form the solution.

Then, the pH range of the solution was adjusted 1.9-2.2 using a concentrated suphuric acid solution which was added as droplets. Two electrodes were immersed into the solution as seen in Figure 2.15. One of them is a carbon electrode used as an anode (counter electrode) and, the other is nickel electrode (its immersed size into the solution was 1x1 cm^2) used as a working electrode (cathodic electrode). During the deposition process, the temperature of the solution was maintained at 65^0C ±3 and the chemical solution was stirred at 500 rpm using a magnetic stirrer-heater device. The deposition was carried out by using a potantiostat-galvanostat device. The ZnSe thin film was cathodically deposited onto the nickel layer.

During the deposition the potential of the substrate with respect to the anodic electrode was kept constant at 0.60-0.66 V. The deposition is called as potantiostatic deposition. The desired potential was immediatly applied upon insertion of the electrode into the chemical solution and the deposition time was maintained for 90 min.

The pH of the solution plays a major role in the electrolyte stability and, in the magnitude of current density. If the pH is greater than 3, the solution becomes turbid and the current passing through the solution increases therefore the color of the ZnSe thin film is shifts from yellowish to dark.

If the pH is less than 2, the ZnSe thin film is insufficently grown onto the nickel substrate. For this reason, the pH of the solution affects the composition of electrodeposited thin films. So it is always better to have the pH of the solution lying in the 2-3 range.

The temperature of the solution also plays a major role in the deposition of ZnSe film.. When the solution temperature is increased, the deposition time decreased and, the deposition of the thin film also increases with increasing temperature.

During the deposition process positively charged Zn^{+2} and Se^{+} ions are accelerated under the influence of the applied potential through the cathodic electrode (working electrode).

When the ions reach to the nickel electrode they take electrons from the nickel electrode and hence they bond to substrate surface, so that Zn and Se deposite simultanously on the substrate and an yellowish colour thin film forms as ZnSe.

During this process, an amount of hydrogen gas is formed therefore at least a part of the current which is passing through the electrolyte is used consumed in this hydrogen formation.

The following conditions must be maintained for a potentiostatic growth of the good quality ZnSe thin film;

i) pH : 2.0 - 2.5.
ii) Deposition time: 80 - 120 min.
iii) Applied potential: 0,60 - 0,70 V.
iv) Solution temperature: 65 - 70 ^{0}C.
v) Stiring rate: 400 - 600 rpm.

MEASUREMENTS AND RESULTS

2.10 Measurement Techniques

In this section, we will deal with measurements techniquies used to obtained the measurement results which will be used for the investigation of the optical and the electrical properties and crystal structure of the semiconducting CdS, CdSe and ZnSe thin films which are grown by using spraying and electrodeposition methods.

2.10.1 Optical Measurements

An important technique used for the determination of the band gap energy of a semiconductors is the absorption of incident photons by material. In this experiment, photons of selected wavelength are directed at the sample, and the relative transmission of the various photons is measured. Since photons with energies greater than the band gap energy are absorbed while photons with energies less than band gap are transmitted, this experiment gives an accurate measure of the band gap energy.

To determine the energy band gap values of the samples, it is necessary to determine the value of the absorption coefficients of the samples corresponding to different wavelengths of the photons. For this purpose, a Jasco 7800 Model UV-VIS Spectrofotometer (wavelength range is 200-1100 nm) was used for the transmission and absorption measurements. The absorption coefficient (α) of sample corresponding to different wavelengths can be calculated from the value of transmission using the following equations:

$$\frac{I}{I_0}(transmission) = e^{-\alpha t} \qquad (2\text{-}12)$$

from this equation,

$$\alpha = \frac{1}{t\ln(\frac{I}{I_0})} \tag{2-13}$$

where t is the thickness of the thin film sample, $T=I/I_0$ is transmittance. (I_0 is incident light intensity and I is transmitted light intensity)

By using α values, the optical band gap of the thin film sample can be determined by using of the following equation

$$\alpha(h\nu) = A(h\nu - E_g)^{\frac{1}{2}} \tag{2-14}$$

where A is a constant, E_g energy band gap of thin film, h is Planck constant, $\nu=c/\lambda$, c is light speed and λ is wavelength of light.

The bandgap energies (Eg) of the semiconducting thin films can be estimated from a plot of $(\alpha h\nu)^2$ versus hν and the direct bandgap of the semiconducting thin films are determined by extrapolating the straight line to the energy axis. The band gap energy values of the samples of CdS, CdSe and, ZnSe grown by the spraying and electrodeposition methods on different substrates were evaluated from the absorption coefficient graphics.

2.10.2 The Crystal Structure of The Thin Film Samples

The crystallinities of CdS, ZnSe, CdSe semiconducting thin films, grown by using spraying and electrodeposition technique were studied by using a Philips X-Ray Powder diffractometer with monochromated high intensity CuKα radiation ($\lambda=1.5405A^0$). The peaks (2θ) of the XRD patterns of the thin film samples were identified by using Bragg diffraction law equation as given follows;

$$\sin^2\theta = \frac{\lambda^2}{4a^2}\left(h^2 + k^2 + l^2\right) \tag{2-15}$$

Diffraction spectra of all the samples are given in section 2.11.2.

2.10.3 Electrical Measurements

In this study, the Van der Pauw method was used to measure the resistivity, conductivity and Hall coefficient of the thin film samples. To apply this method, four indium ohmic contacts A,B,C and D were prepared on the semiconducting samples by the evaporation method as seen in Figure 2.16.

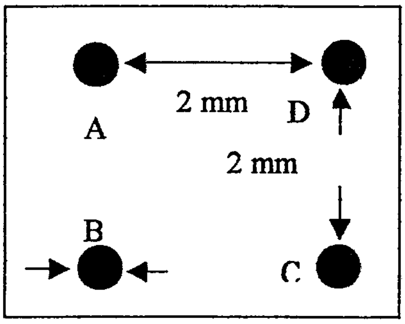

Figure 2.16 The Indium-ohmic contacts prepared on thin film samples.

2.10.3.1 Resistivity and Conductivity Measurements

The resistivity measurement was carried out in two steps establishing an experimental set-up as seen in Figure 2.17.

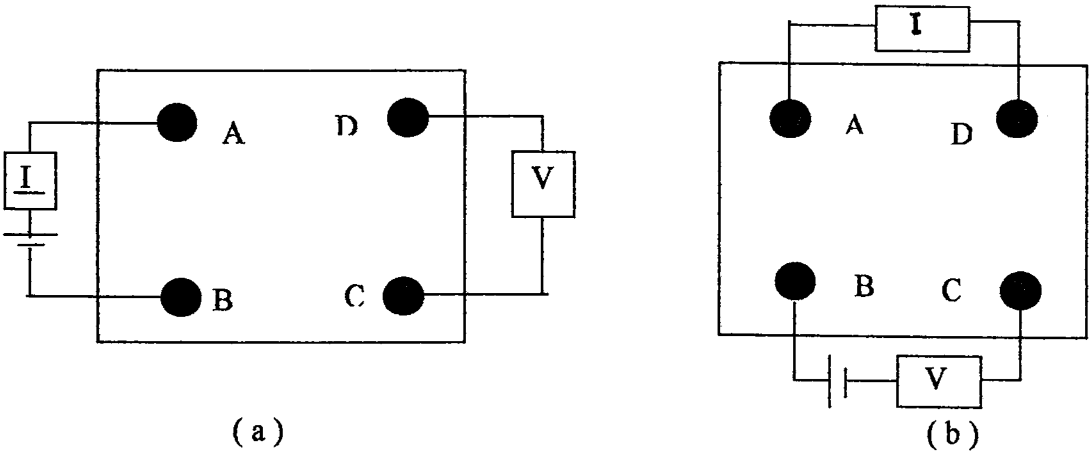

Figure 2.17 The experimental set-up of the resistivity measurement

Applying an input potential V_{in} across the contacts A and B, as seeen in Figure 2.16-a current I_{AB} is measured. On the other hand, a potential V_{CD} appears between the contacts C and D. $R_{AB,CD}$ denotes the ratio of voltage V_{CD} measured between contacts C and D, to the current I_{AB} flowing between A and B. To determine the resistance $R_{BC,DA}$ at this time, the input potential is applied across the contacts B and C, as seen in Figure 2.16-b. Then, the current I_{BC} flows across the contacts B and C and the potential V_{DA} between these contacts is measured.

The resistivity of sample is calculated by using the following equation :

$$\rho = \left(\frac{t}{\ln 2}\right)(R_{AB,CD} + R_{BC,DA})F\left(\frac{R_{AB,CD}}{R_{BC,DA}}\right) \tag{2-16}$$

where t is the thickness of the thin film and F is a function. If $R_{AB,CD}$ and $R_{BC,DA}$ are nearly equal to each other, the approximate value of F can be obtained from following expression [87]:

$$F = 1 - \left(\frac{R_{AB,CD} - R_{BC,DA}}{R_{AB,CD} + R_{BC,DA}}\right)^2 \left(\frac{\ln 2}{2}\right) - \left(\frac{R_{AB,CD} - R_{BC,DA}}{R_{AB,CD} + R_{BC,DA}}\right)^4 \left(\frac{(\ln 2)^2}{4} - \frac{(\ln 2)^3}{12}\right) \tag{2-17}$$

The thicknesses of the samples were obtained by using the weighing method. This method is explained by the following expression:

$$t = \frac{(m_2 - m_1)}{\rho A} \tag{2-18}$$

where m_1 is the weight of the glass substrate, m_2 is the weight of the same glass substrate after thin film grown on it, A is the area of the glass substrate and ρ is the density of the thin film material.

2.10.3.2 Hall Mobility Measurements

The experimental configuration for the Hall Mobility measurement set up is seen in Figure 2.18 a. Then, thin film sample is placed in a magnetic field perpendicular to the sample plane and the $R_{AC,DB}$ resistance value is measured for a few times and the average value of the $R_{AC,DB}$ is taken.

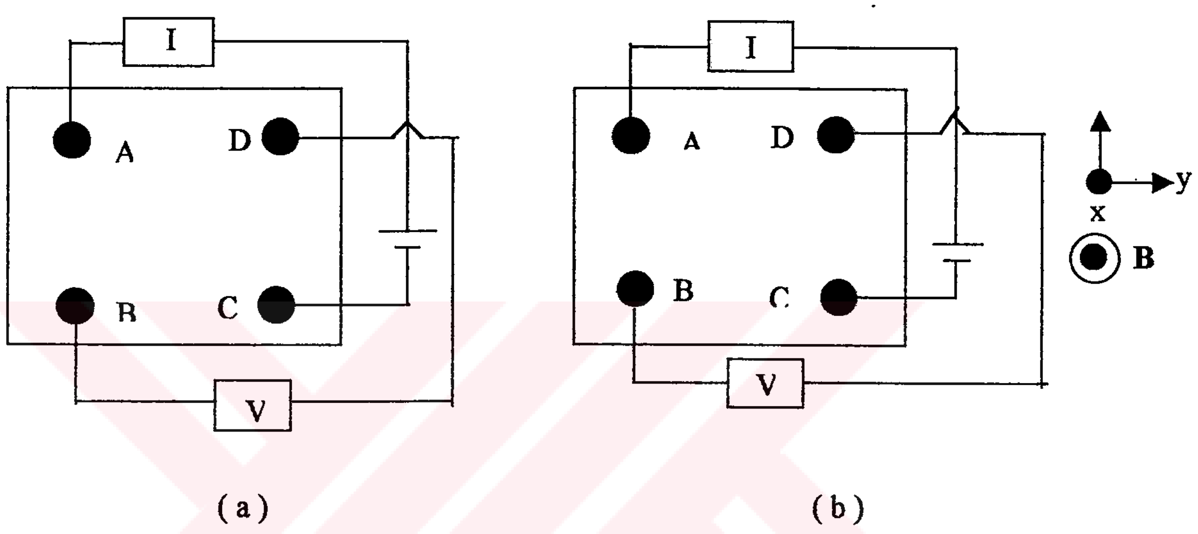

Figure 2.18 The standart configuration used for hall effect measurement

The Hall Mobility can be calculated substituting the measured values of $R_{AC,DB}$, the applied magnetic field, B, and thickness of the thin film layer, t,in the following expression;

$$\mu = \left(\frac{t}{B}\right)\left(\frac{R_{AC,DB}}{\rho}\right) \tag{2-19}$$

where ρ is the resistivity of the thin film material [87].

2.11. Results and Discussion

2.11.1. Optical Measurement Results of The Semiconducting Thin Films

For the determination of the electronic band-edge structure of the thin film samples (sprayed CdS, CdSe and ZnSe), the best method is to study the absorption gap through the measurement of transmission spectra. For this process, we need to spray the samples onto an optically transparent substrate. Therefore, all of the thin films were sprayed onto the glass substrate which is transparent in a spectral region that includes the visible wavelengths.

The bandgap of the resulting films were estimated from the transmission spectra using the extrapolation of $(\alpha h\nu)^2$ versus $h\nu$. The value of the absorption coefficient (α) was obtained from the value of the transmission by using the Eq.2.13. The transmission spectra and bandgap energy (E_g) graphs of the semiconducting CdS, CdSe and ZnSe thin films are given in figures. (Fig.2.19-2.24).

2.11.1.1. The Transmission Spectra and Band gap Energy Graphs of The Sprayed CdS, CdSe and ZnSe Thin Films

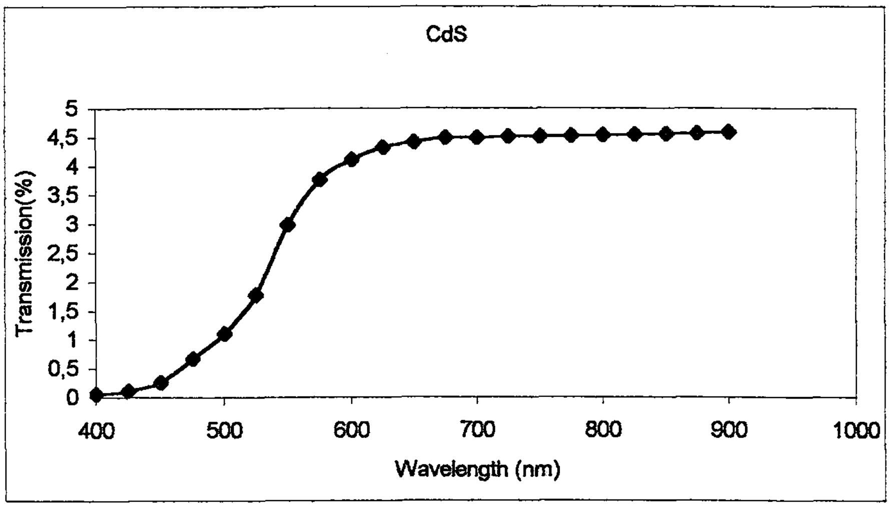

Figure 2.19 (a) The optical transmittance spectra versus the wavelength of the CdS thin film grown by using spraying pyrolysis method

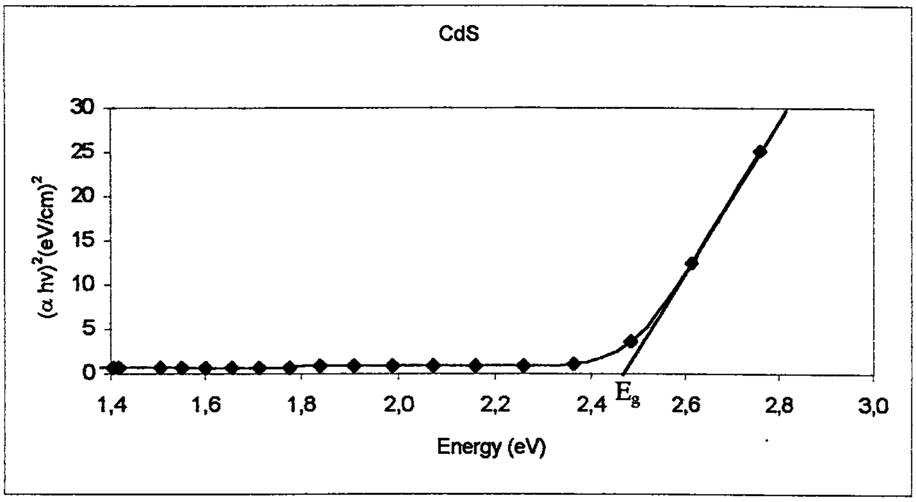

Figure 2.19 (b) Plot of $(\alpha h\nu)^2$ versus photon energy ($h\nu$) for film the CdS thin film grown by using spraying pyrolysis method

Figure 2.19 (a) shows the direct band gap material CdS is capable of emitting light in the green region of the visible spectrum with wavelength about 506 nm and Figure 2.19 (b) shows the average band gap energy values for CdS is obtained 2.44 eV. This means that the threshold energies for the photon absorption by CdS semiconducting thin films at room temperature is about 2,44 eV.

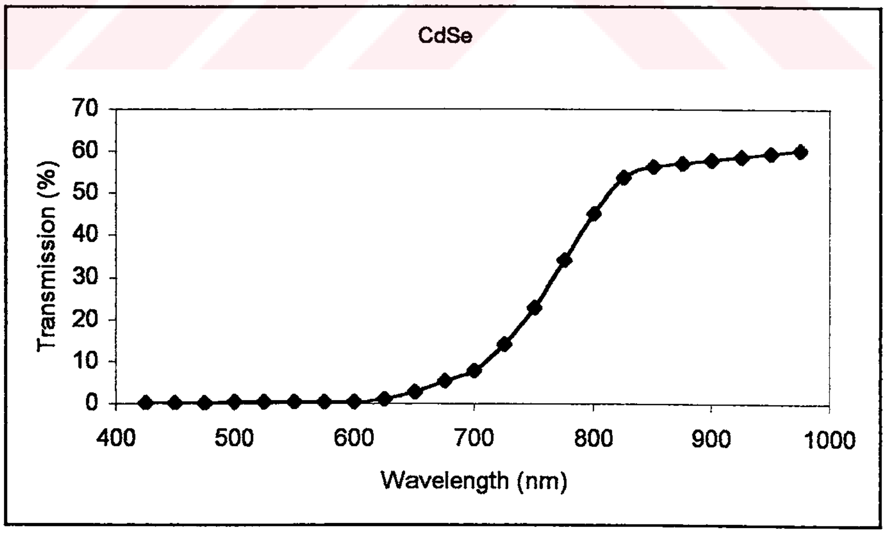

Figure 2.20 (a) The optical transmittance spectra versus the wavelength of the CdSe thin film grown by using spraying pyrolysis method

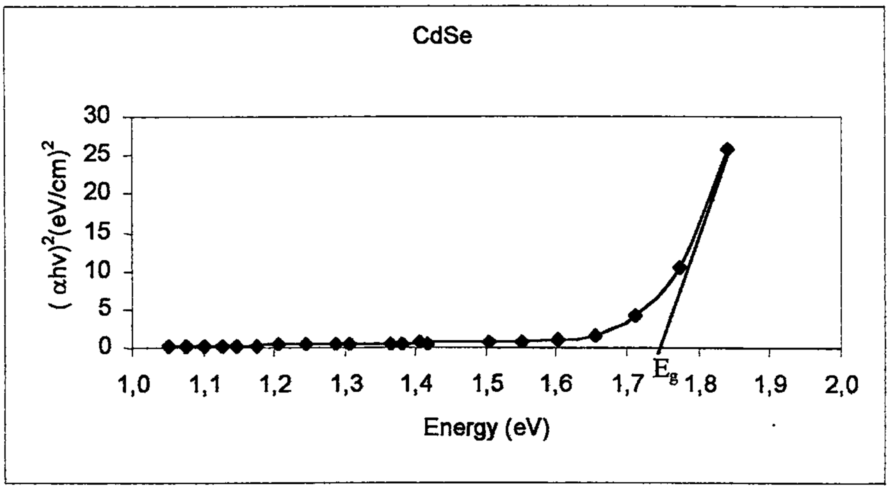

Figure 2.20 (b) Plot of $(\alpha hv)^2$ versus photon energy (hv) for the s the CdSe thin film grown by using spraying pyrolysis method

As seen from Figure 2.20 (a), the direct band gap material CdSe is capable of emitting light in the red region of the visible spectrum with a wavelength about 700 nm and other Figure 2.20 (b) shows the average band gap energy values for CdSe were obtained 1,76 eV. This means that the threshold energies for the photon absorption by CdSe semiconducting thin films at room temperature is about 1,76 eV.

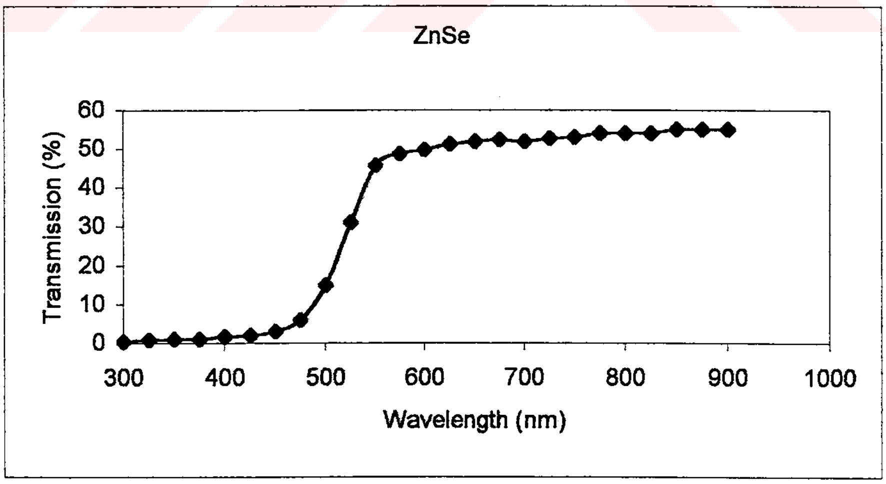

Figure 2.21 (a) The optical transmittance spectra versus the wavelength of the ZnSe thin film grown by using spraying pyrolysis method

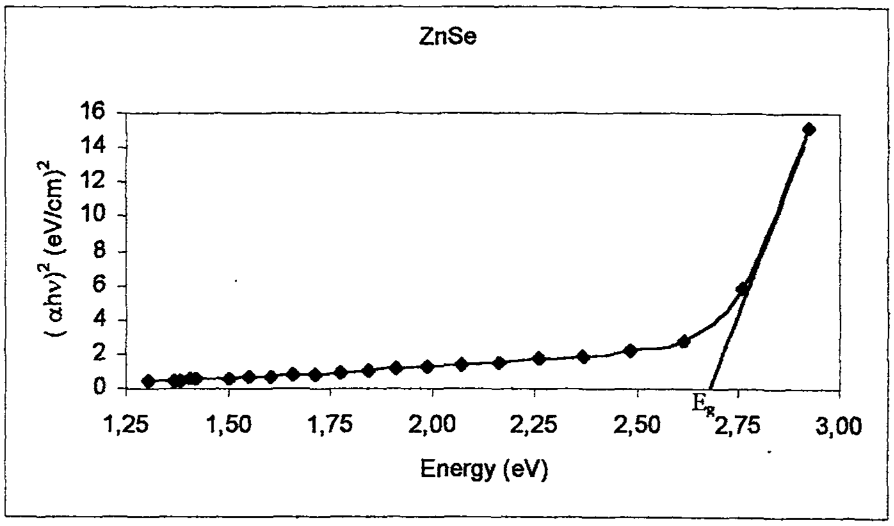

Figure 2.21 (b) Plot of $(\alpha h\nu)^2$ versus the photon energy (hv) for the ZnSe thin film grown by using spraying pyrolysis method

Figure 2.21 (a) shows the direct band gap material ZnSe is capable of emitting light in the blue-green region of the visible spectrum with wavelength of 475 nm, and Figure 2.21 (b) shows average band gap energy values for ZnSe thin film is 2,6 eV. This means that the threshold energies for the photon absorption by ZnSe semiconducting thin films at room temperature is about 2,6 eV. Optical characterization of ZnSe thin film sprayed on glass substrate gives us an energy band gap of 2.6 eV, it is quite close to the accepted room temperature value of 2.68 eV [72]. This result could be attributed to the size effect observed in ZnSe thin films.

2.11.1.2. The Transmission Spectra and Band-gap Energy Graphs of The Electrodeposited CdS, CdSe and ZnSe Thin Films

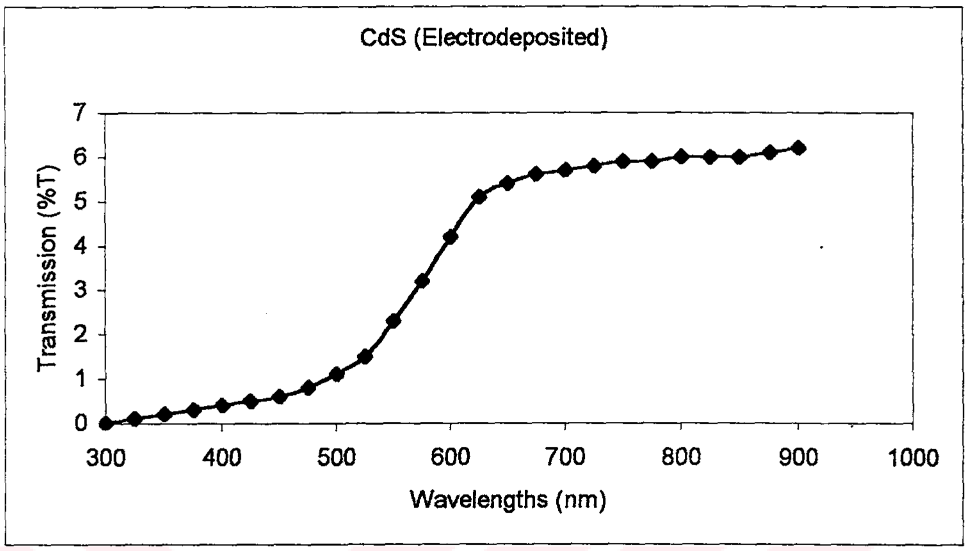

Figure 2.22 (a) The optical transmittance spectra versus the wavelength of the CdS thin film grown by using electrodeposition method

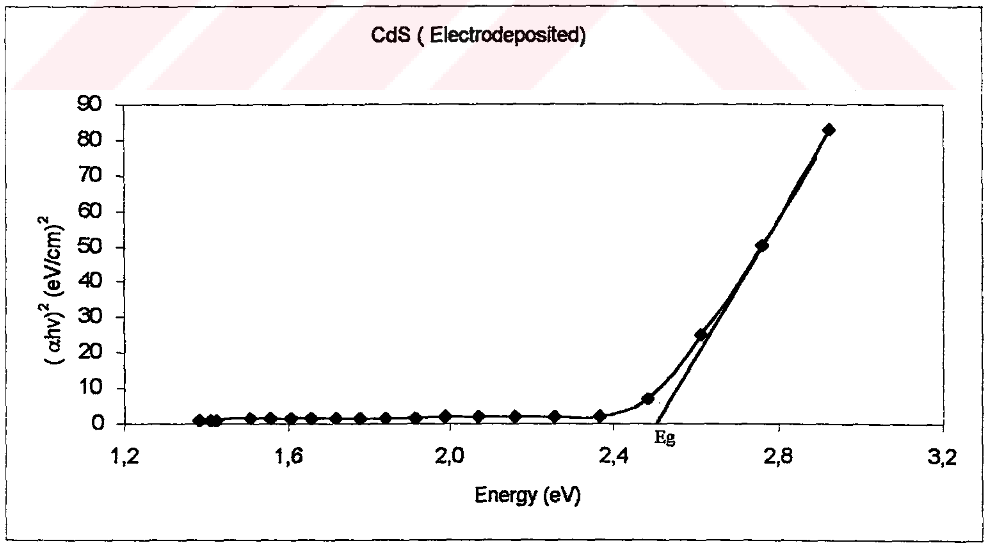

Figure 2.22 (b) Plot of $(\alpha h\nu)^2$ versus photon energy ($h\nu$) for the CdS thin film grown by using electrodeposition method

Figure 2.22 (a) shows the direct band gap material CdS of emitting light in the green region of the visible spectrum with wavelength about 496 nm and Figure 2.22 (b) shows the average band gap energy values of the for electrodeposited CdS is obtained about 2,49 eV. This means that the threshold energies for the photon absorption by CdS semiconducting thin films at room temperature is about 2.49 eV.

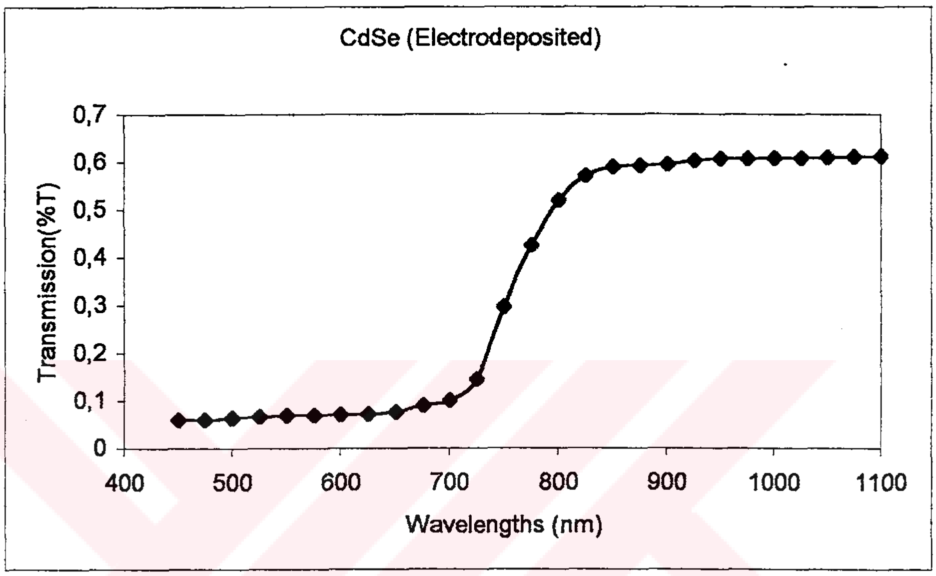

Figure 2.23 (a) The optical transmittance spectra versus the wavelength of the CdSe thin film grown by using electrodeposition method

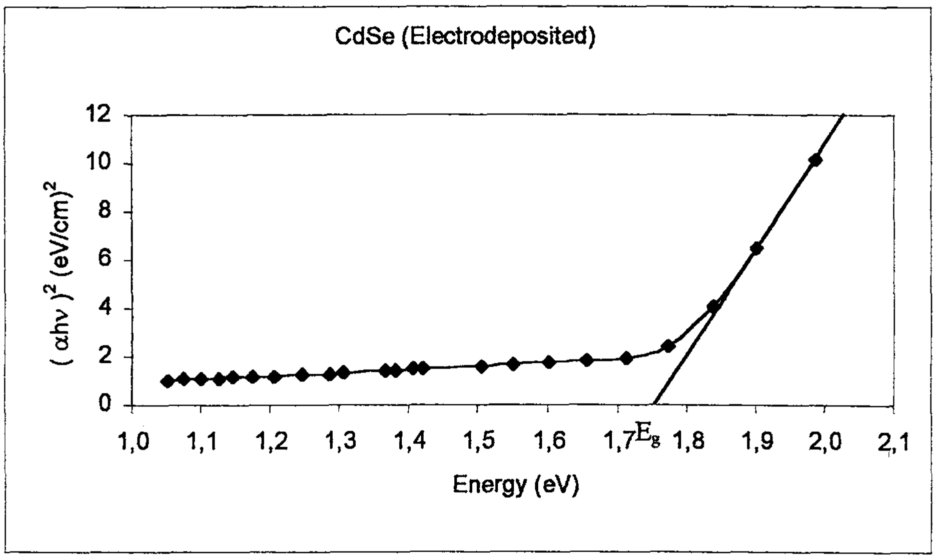

Figure 2.23 (b) Plot of $(\alpha h\nu)^2$ versus photon energy ($h\nu$) for the CdSe thin film grown by using electrodeposition method

As seen from Figure 2.23 (a) the direct band gap material CdSe is capable of emitting light in the red region of the visible spectrum with a wavelength about 710 nm and other Figure 2.23 (b) shows the average band gap energy values for electrodeposited CdSe is obtained about 1.74 eV. The band gap energy and also called as the threshold energy measurements have been carried out at room temperature.

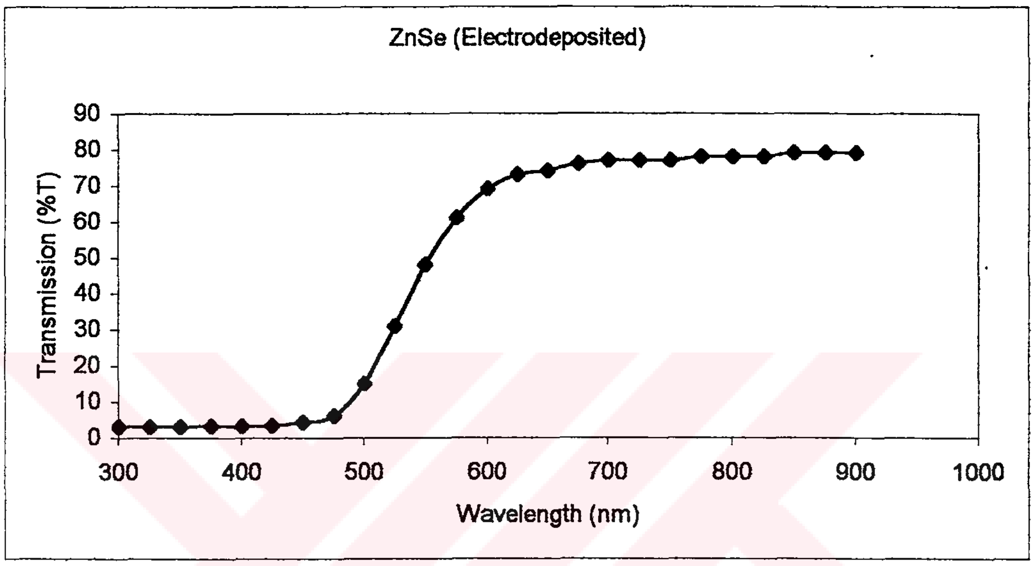

Figure 2.24 (a) The optical Transmittance spectra versus the wavelength of ZnSe thin film grown by using electrodeposition method

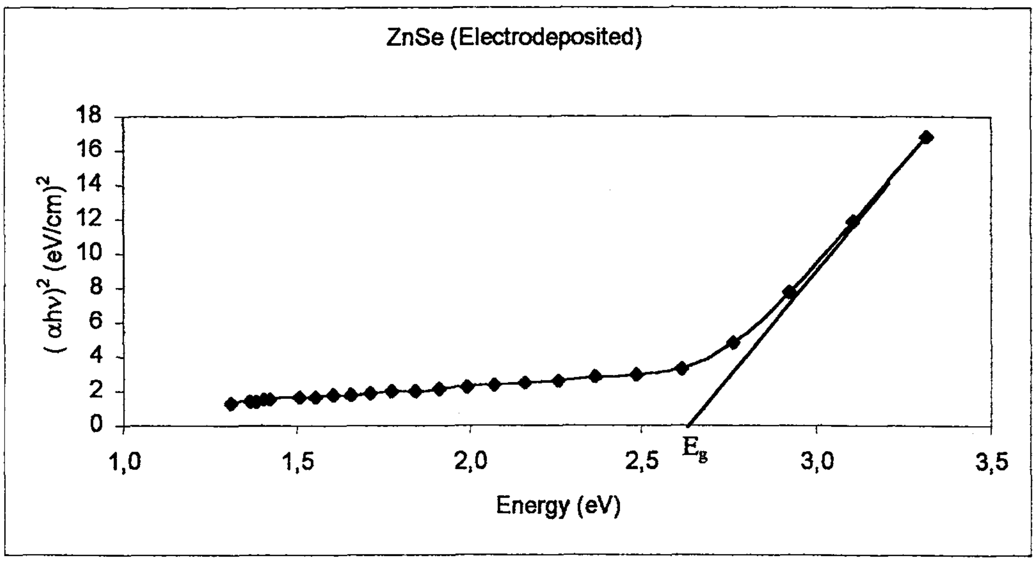

Figure 2.24 (b) Plot of $(\alpha h\nu)^2$ versus the photon energy ($h\nu$) for the ZnSe thin film grown by using electrodeposition method

Figure 2.24 (a) shows the direct band gap marerial ZnSe is capable of emitting light in the blue-green region of the visible spectrum with wavelength of 470 nm, and Figure 2.24 (b) shows the average band gap energy values for electrodeposited ZnSe thin film is about 2,64 eV. Therefore the threshold energy for the photon absorption by ZnSe semiconducting thin films at room temperature is about 2.64 eV.

2.11.2. The X-Ray Diffraction Spectra of Thin Films Grown by Spraying and Electrodeposition Method

The crystallinities of CdS, CdSe and ZnSe semiconducting thin films, grown by using spraying and electrodeposition technique were investigated using Philips X-Ray Powder Diffractometer with monochromated high intensity CuKα radiation (λ=1.5405 A^0). The orientations of the crystallites in the films were determined by using the Bragg diffraction law equation which is given in section 2.10.2. The diffraction spectra of all the samples are given in following figures. (Fig.2.25-2.27).

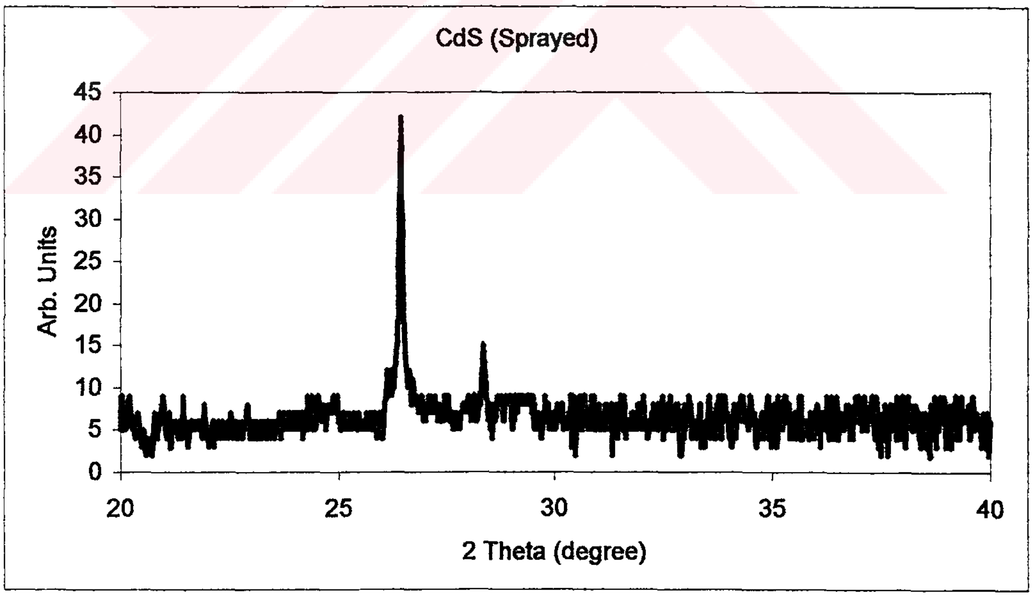

Figure 2.25 (a) X-ray diffraction pattern of the CdS thin film sample grown by using spraying pyrolysis method

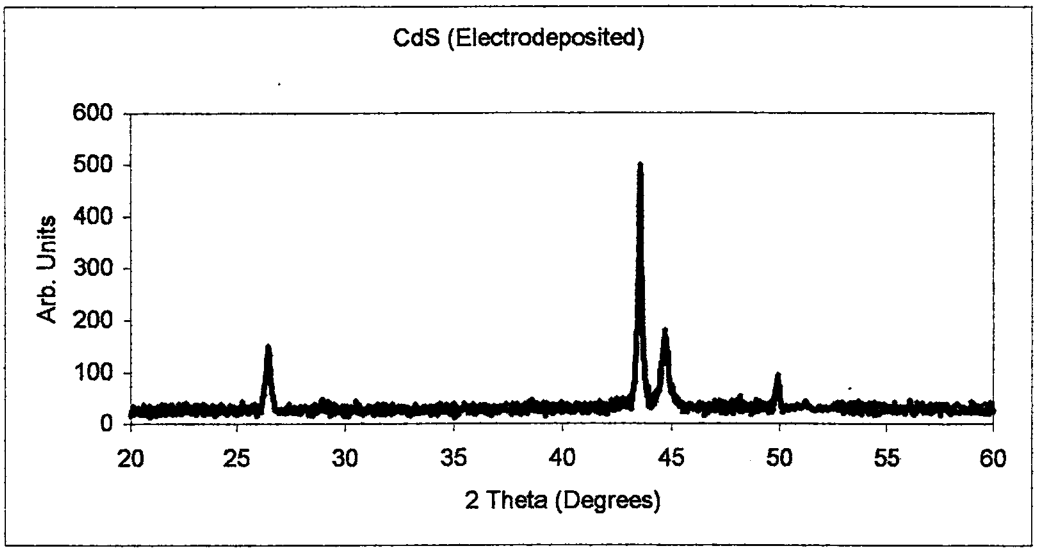

Figure 2.25 (b) X-ray diffraction pattern of the CdS thin film sample grown by using electrodeposition method

Figure 2.25(a) shows the x-ray diffraction spectrum of CdS thin film grown on glass substrate by using spraying pyrolysis method. The spectrum of the film shows a sharp peak at $2\theta = 26.42^0$ is polycrystalline with (002) planes corresponding to CdS hexagonal phase. Figure 2.25(b) shows the x-ray diffraction spectrum of the CdS thin shows sharp peaks at $2\theta = 26.46^0$, 43.52^0, 44.18^0 and 49.92^0. First and second peaks correspond to the diffraction (002) and (110) plane of the CdS hexagonal phase. Third peak is resulted from the nickel substrate which corresponds to diffraction film grown on nickel substrate by electrodeposition technique. The spectrum of the film from (111) plane fcc phase and fourth peak at $2\theta = 49.92^0$ resulted from the copper plate which is under the nickel substrate.

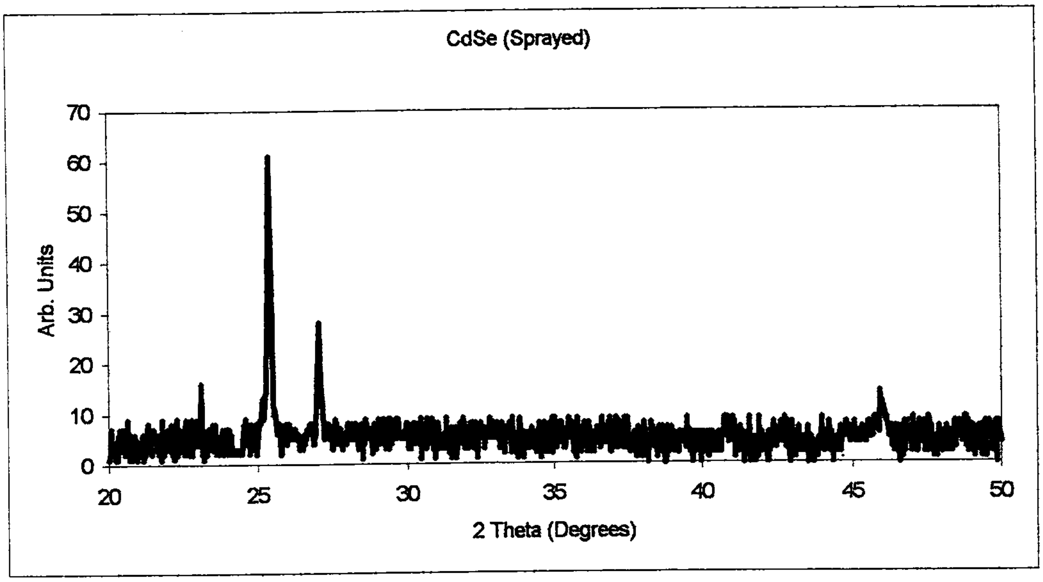

Figure 2.26 (a) X-ray diffraction pattern of the CdSe thin film sample grown by using spraying pyrolysis method

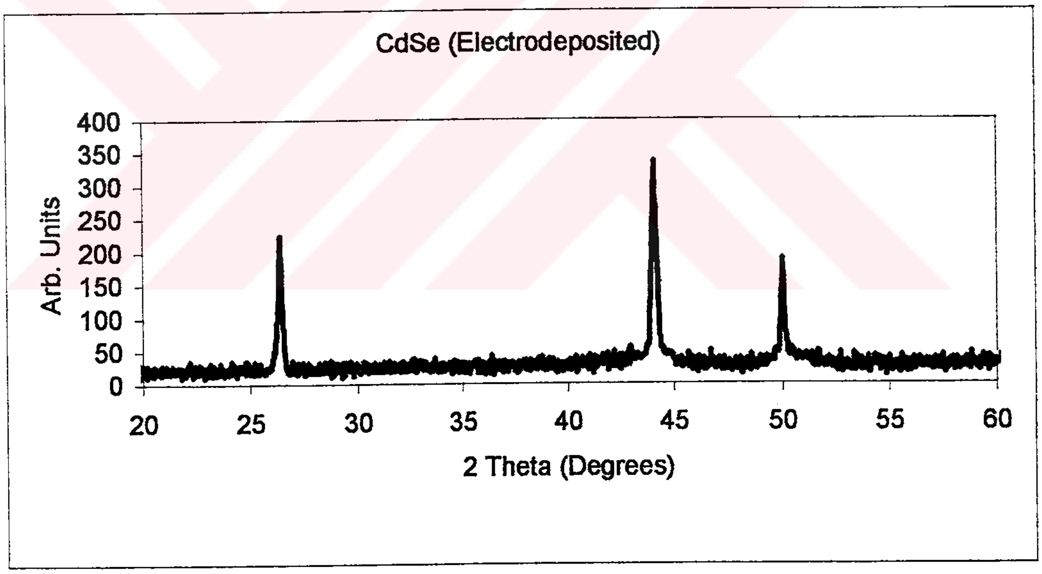

Figure 2.26 (b) X-ray diffraction pattern of the CdSe thin film sample grown by using electrodeposition method

Figure 2.26(a) shows the x-ray diffraction patterns of CdSe thin film grown on glass substrate by using spraying pyrolysis method. The CdSe thin film powder spectrum exhibits sharp peaks at $2\theta = 25.4^0$ and 27.04^0 which correspond to diffraction from (002) and (101) planes of hexagonal CdSe phase, the stable structure of CdSe at room temperature is normally the hexagonal wurtzite. Figure 2.26(b) shows x-ray diffraction patterns of CdSe thin film grown on nickel substrate by using electrodeposition technique. The spectrum of the CdSe thin film shows sharp peaks at 2θ = 26.36^0, 44.06^0 and 50.2^0. The first peak corresponds to the diffraction (002) plane of the CdSe hexagonal. The second peak is resulted from the nickel substrate which corresponds to diffraction from (111) plane fcc phase and the third peak is produced by the copper plate which is put under the nickel substrate.

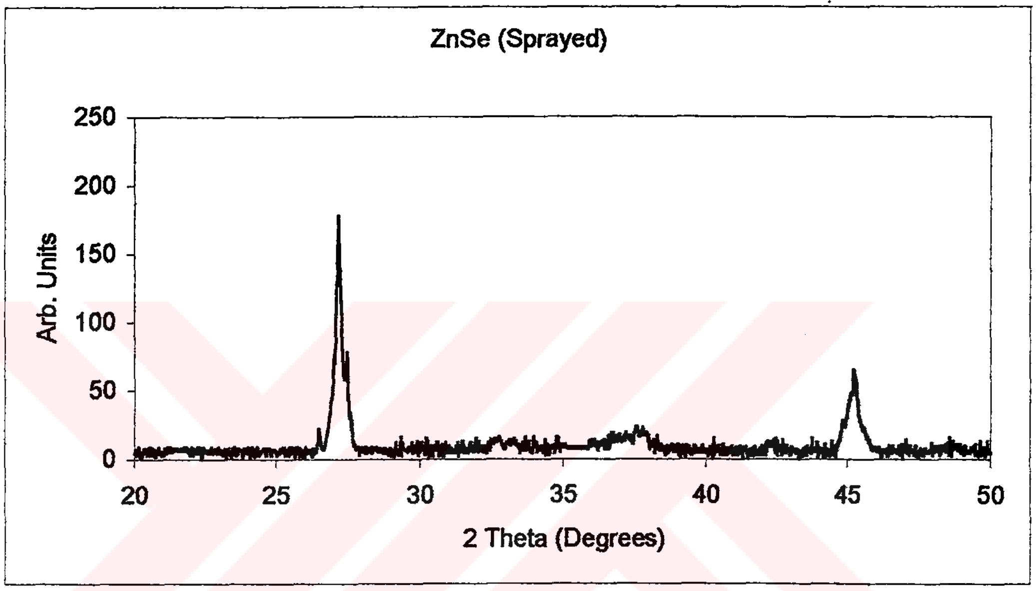

Figure 2.27 (a) X-ray diffraction pattern of the ZnSe thin film sample grown by using spraying pyrolysis method

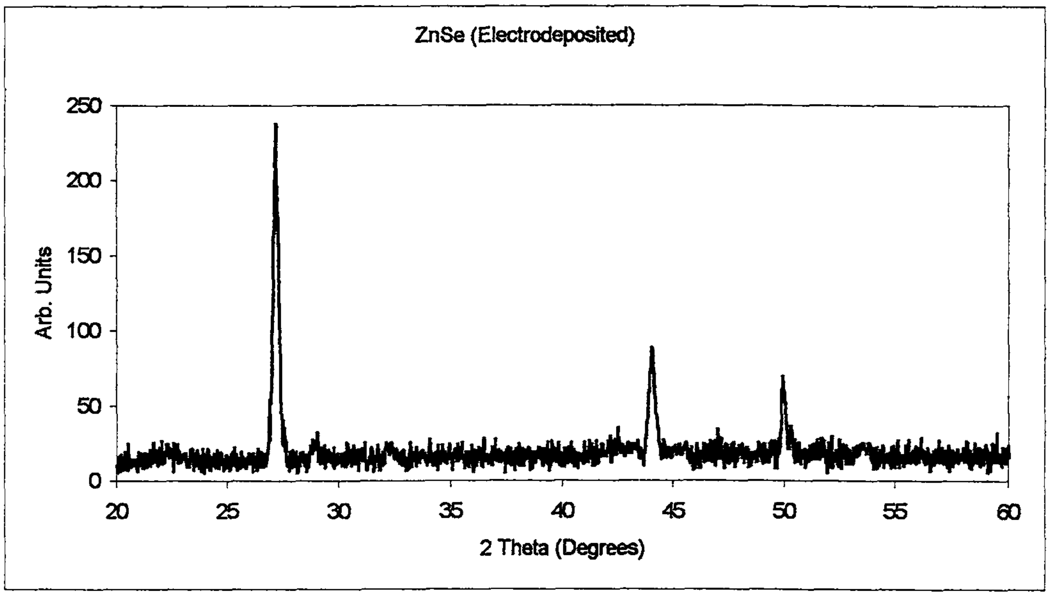

Figure 2.27 (b) X-ray diffraction pattern of the ZnSe thin film sample grown by using electrodeposition method

Figure 2.27 (a) shows the x-ray diffraction patterns of ZnSe thin film grown on glass substrate by using spraying prolysis method. The ZnSe thin film powder spectrum exhibits sharp peaks at $2\theta = 27.16^0$ and 44.72^0 which correspond to diffraction from (111) and (220) planes of cubic zinc blende structure. Figure 2.27 (b) shows x-ray diffraction patterns of ZnSe thin film grown on nickel substrate by using electrodeposition technique. The ZnSe thin film powder spectrum exhibits sharp peaks at $2\theta = 27.18^0$, 44.02^0 and 49.99^0. The first peak corresponds to diffraction from (111) plane of the ZnSe cubic phase. The second peak is resulted from the nickel substrate which corresponds to diffraction from (111) plane fcc phase. The third peak is resulted from the copper plate which lies under the nickel substrate. Both of types of x-ray diffraction patterns show that ZnSe thin films are polycrystallines having fcc zincblende structure.

2.11.3. Electrical Measurement Results of Semiconducting Thin Film Samples

The electrical measurements of the CdS thin film samples were carried out by using the Van der Pauw Method at room temperatureas explained in section 2.10.3. The resistivity and conductivity values were calculated from Eq.2.16 and the Hall Mobility values of the thin film samples were calculated from Eq.2.19 and all the calculated results are given in Table.2.2.

Table 2.2 Electrical measurement results of the CdS thin films grown by spraying pyrolysis technique on glass substrate at different substrate temperature

Substrate temperature (^{0}C)	Resistivity (10^5 ohm-cm)	Conductivity (10^{-6} (ohm-cm)$^{-1}$)	Hall Mobility (cm^2/V sec)
340	5.32	1.87	19
380	3.93	2.5	28
420	5.44	1.83	25

As seen in Table 2.2, electrical properties of CdS semiconducting thin films which have been developed with the ratio Cd:S=1:1 and at different substrate temperatures 340, 380 and 420^{0}C, respectively, are given. In Figure 2.28 (a), (b) and (c) show the resistivity, Hall Mobility and conductivity curves against the substrate temperature.

As seen from these curves the resistivity of the CdS thin film samples has a minimum value at about 380^{0}C but the Hall Mobility has a maximum value at the same substrate temperature. It can be seen that the resistivity of CdS thin film decreases first with increasing substrate temperature up to 380^{0}C, and then the resistivity increases with increasing substrate temperature. And also that the Hall Mobility of the CdS thin films increases with increasing substrate temperature up to 380^{0}C then the Hall Mobility decreases with increasing substrate temperature.

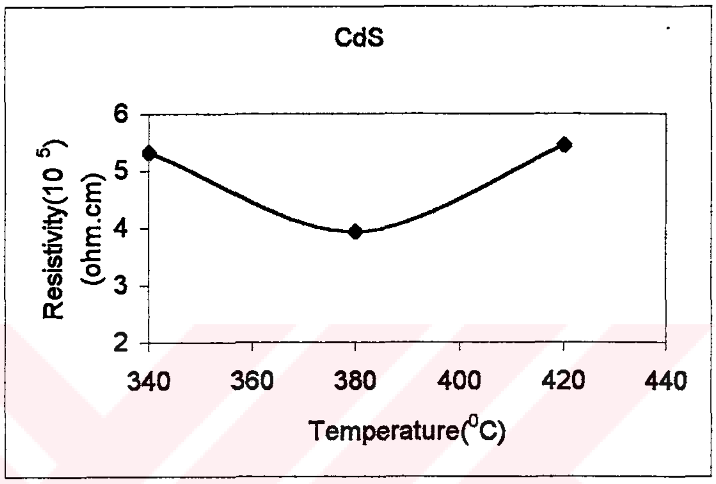

Figure 2.28 (a) Variation of the resistivity versus substrate temperature of the CdS thin film samples grown by using spraying pyrolysis method

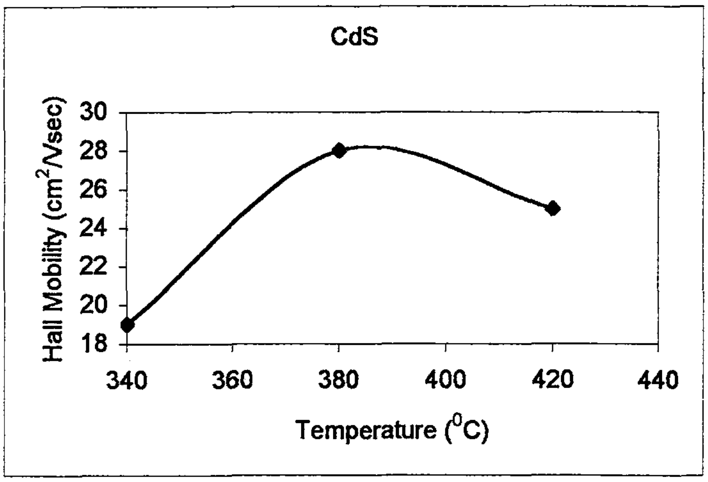

Figure 2.28 (b) Variation of the Hall Mobility versus substrate temperature of the CdS thin film samples grown by using spraying pyrolysis method

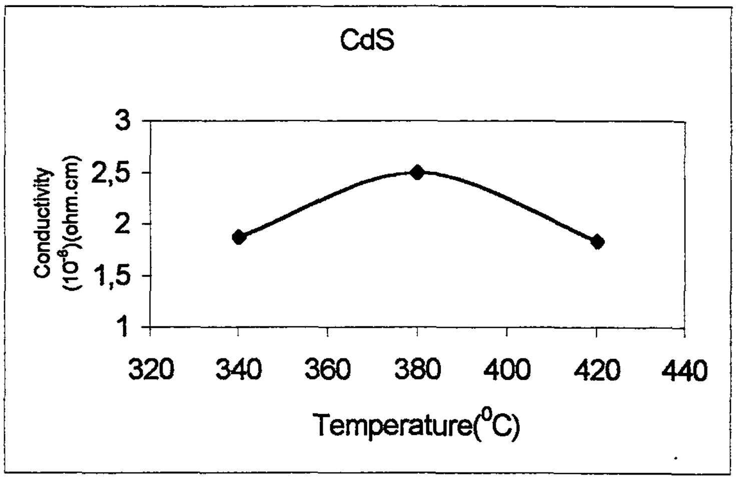

Figure 2.28 (c) Variation of the conductivity versus substrate temperature of the CdS thin film samples grown by using spraying pyrolysis method

It can be shown from these results that, if the CdS thin film samples are prepared at substrate temperature of lower and higher than 380^{0}C they may have a high resistivity and low Hall Mobility. When they are prepared at a substrate temperature of about 380^{0}C, CdS thin film samples show a low resistivity (3,93x10^5 ohm-cm) and high Hall Mobility (28 cm^2/V-sec).

Another important result seen from these figures is that the resistivity, the Hall Mobility and conductivity of the CdS thin films are strongly dependent on the substrate temperature. Remembering that the samples were grown using the spraying solution with the ratio Cd:S=1:1. It may be concluded that this result is because of the number of the cadmium and sulphur atoms which form the crystal structure of the thin film.

If the ratio of the cadmium and sulphur atoms are equal to each other, all cadmium and sulphur atoms make covalent bonds with each other. This means that there will be either no free cadmium or sulphur atoms in crystal. If the ratio of the atoms differs from the ratio of Cd:S=1:1, there will be free cadmium atoms or sulphur atoms in crystal. The excess cadmium or sulphur atoms in CdS thin films cause the grain size to increase. It is known that the resistivity of the CdS thin film decreases with increasing grain size. And also the resistivity and Hall Mobility of sprayed CdS thin films are very sensitive to absorbed oxygen since chemisorbed oxygen acts as an acceptor impurity.

Because of this, it causes an increase in the resistivity but a decrease in the Hall Mobility of the thin films. The increase in the resistivity of the thin films results from the increase of the potential barrier. This increase in the potential barrier results due to the interaction of the absorbed oxygen with the grain boundaries. So, regarding the comments above it may be attributed that the cause of high resistivity and low Hall mobility above and below a certain temperature (eg. 380^0C) may be because of the grain size, grain boundry or absorption of oxygen.

The electrical resistivity, conductivity and Hall Mobility of the sprayed CdSe thin films were measured by using Van der Pauw method at room temperature. The electrical resistivity of the thin film samples vary from $7.32\mathrm{x}10^5$ ohm-cm to $5.8\mathrm{x}10^5$ ohm-cm, the conductivityof the thin film samples vary from $1.366\mathrm{x}10^{-6}$ $(\text{ohm-cm})^{-1}$ to $1.72\mathrm{x}10^{-6}$ $(\text{ohm-cm})^{-1}$, and the Hall mobility of the thin film samples from 39 cm^2/Vsec to 44 cm^2/Vsec, as the substrate temperature of the sprayed CdSe thin films increases from 380^0C to 420^0C. The electrical resistivity, conductivity, and Hall mobility of the CdSe thin film samples developed at different substrate temperatures are given in Table 2.3.

Table 2.3. Electrical measurement results of the CdSe thin films were grown by spraying pyrolysis technique on glass substrate at different substrate temperature

Substrate temperature (^{0}C)	Resistivity (10^5 ohm-cm)	Conductivity (10^{-6} $(\text{ohm-cm})^{-1}$)	Hall Mobility ($\text{cm}^2/\text{V sec}$)
380	7.32	1.366	39
400	6.73	1.48	43
420	5.8	1.72	44

CdSe semiconducting thin films were developed with the ratio Cd:Se=1:1 and at different substrate temperatures 380, 400 and 420^0C, respectively. The high value of resistivity or the low value of conductivity at low substrate temperature is attributed to the fine grains of CdSe thin films. The decrease in resistivity at higher substrate temperature is due to the increase in the grain size of CdSe thin films.

This observation is attributed to the size-dependent effect in semiconductor thin film and fine grain size of crystallites. In Figure 2.29 (a), (b) and (c), the resistivity, Hall Mobility and conductivity curves against to the substrate temperature of the sprayed CdSe thin film samples are given.

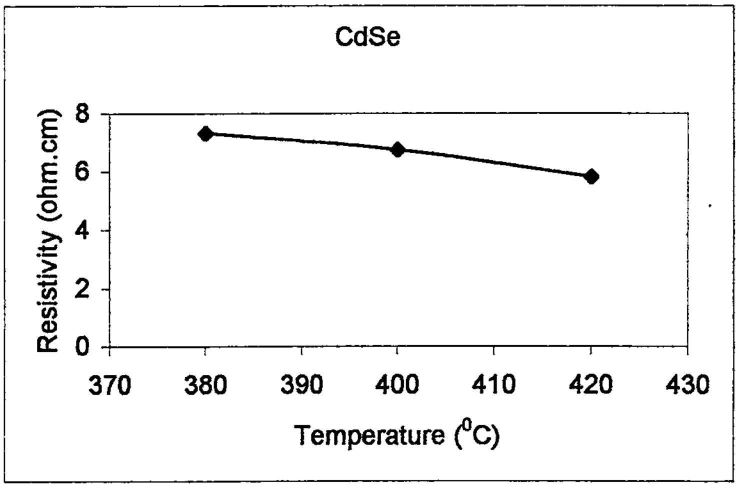

Figure 2.29 (a) Variation of the resistivity versus substrate temperature of CdSe thin film samples grown by using spraying pyrolysis method

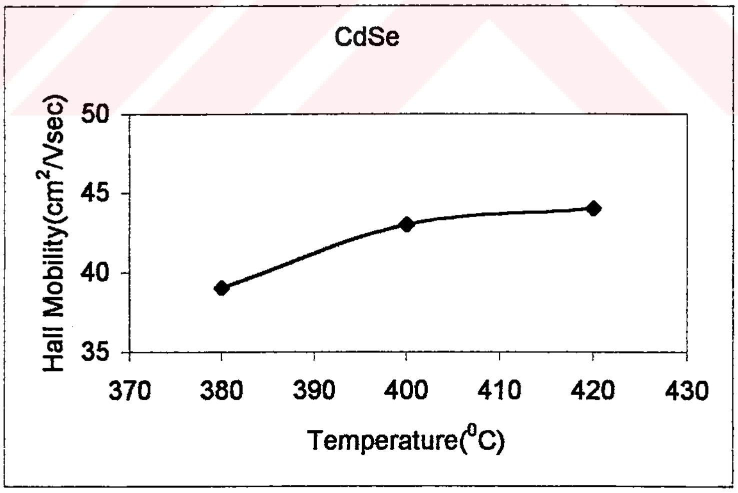

Figure 2.29 (b) Variation of the Hall Mobility versus substrate temperature of CdSe thin film samples grown by using spraying pyrolysis method

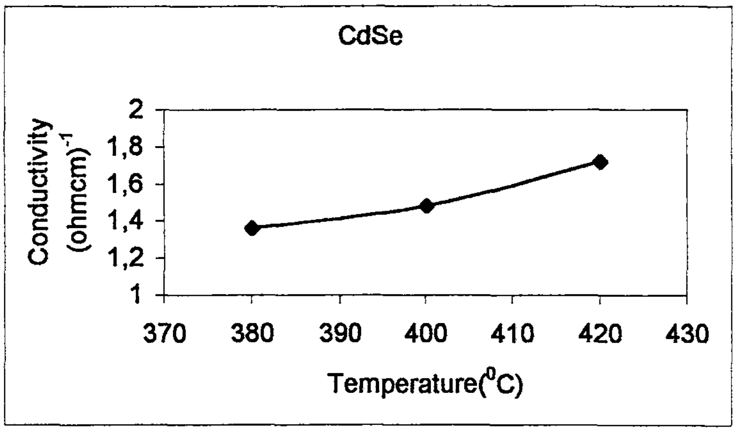

Figure 2.29 (c) Variation of the conductivity versus substrate temperature of CdSe thin film samples grown by using spraying pyrolysis method

It can be seen that from Figure 2.29 (a), (b) and (c), the resistivity, conductivity and Hall mobility of sprayed CdSe thin films are strongly dependent on the substrate temperature All films have the same ratio of the cadmium and selenium atoms. Therefore, there will be either no free cadmium or selenium atoms in the crystal. It is known that the excess cadmium or selenium atoms has an important effect on the growth of the grain size of the films. It can be seen that the resistivity of the CdSe thin films decreases with increasing substrate temperature as the increasing grain size of the films. As seen from the Figure 2.29 (c), Hall Mobility of the CdSe thin film increases with increasing substrate temperature.

All properties of the CdSe thin films are strongly dependent on the substrate temperature which affects the structure of the films. And also it is suggested that the observed changes in resistivity and Hall Mobility may be a consequence of the variation of the chemisorption effect which is associated with changes in the grain size and boundary. Chemisorption of oxygen is known to occur in cadmium selenium crystals and in chemically sprayed films [88]. This effect is very significant for thin films of CdSe.

The electrical properties of the sprayed ZnSe semiconducting thin film samples, resistivity, conductivity and Hall mobility values, have been investigated by employing the same methods used for the CdS and CdSe thin film samples in the previous section (1.10.3). The calculated values of these parameters for ZnSe thin film samples are given in Table 2.4.

Table 2.4 Electrical measurement results of the CdSe thin films grown by using spraying pyrolysis technique on glass substrate at different substrate temperatures

Substrate temperature (^{0}C)	Resistivity (10^5 ohm-cm)	Conductivity (10^{-6} (ohm-cm)$^{-1}$)	Hall Mobility (cm^2/V sec)
400	89.5	1.11	0.32
430	57.9	1.72	0.51
450	65.2	1.53	0.49

The ZnSe Semiconducting thin film samples were grown with the ratio of Zn:Se= 1:1 at different substrate temperatures of 400, 430 and 450^{0}C, respectively. The substrate temperature effect on the electrical properties of the ZnSe thin film samples have been investigated. Figure 2.30 (a), (b) and (c) show the resistivity, conductivity and Hall Mobility curves against the substrate temperature of sprayed ZnSe thin film samples.

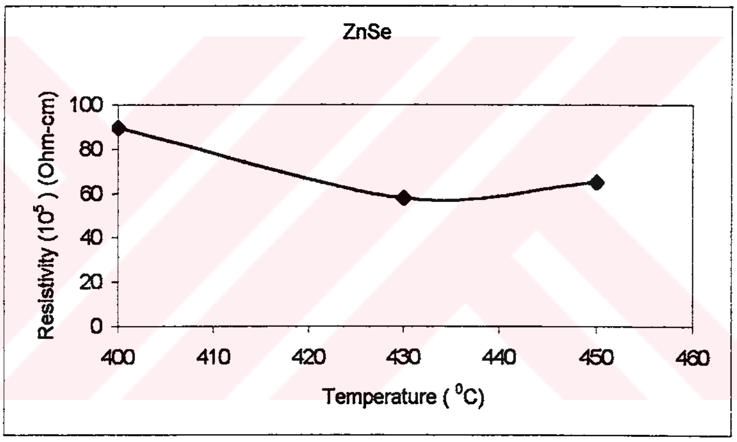

Figure 2.30 (a) Variation of the resistivity versus substrate temperature of CdSe thin film samples grown by using spraying pyrolysis method

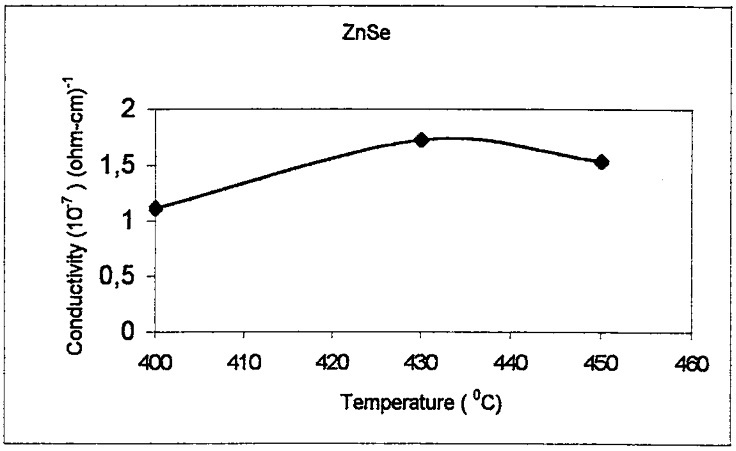

Figure 2.30 (b) Variation of the conductivity versus substrate temperature of CdSe thin film samples grown by using spraying pyrolysis method

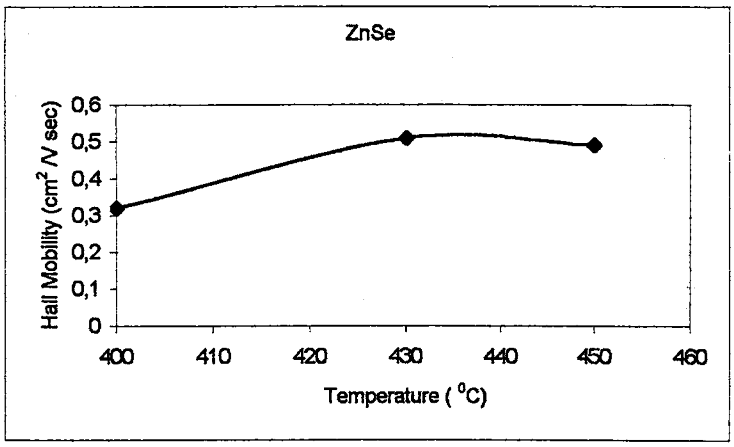

Figure 2.30 (c) Variation of the Hall mobility versus substrate temperature of CdSe thin film samples grown by using spraying pyrolysis method

As seen from Figure 2.30 (a), (b) and (c), while the resistivity has a minimum value at 430°C, the conductivity and Hall mobility of the ZnSe thin film samples has maximum values at the substrate temperature of 430°C. As the substrate temperature is increased the resistivity decreases and reaches its minimum value of 57.9×10^5 ohm-cm at 430°C. On the other hand, as the substrate temperature is increased the Hall mobility increases and reaches its maximum value of 0.51 $cm^2/Vsec$ at 430°C. These results indicate that a relatively good thin film can be obtained at a substrate temperature of 430°C and the resistivity, conductivity and Hall mobility of the ZnSe thin films are strongly dependent on the substrate temperature. And also the crystallinity of the samples are dependent on the substrate temperature. It means that all properties of the ZnSe thin films are dependent on the substrate temperature which closely affects the structure of the films. And also it is suggested that the observed changes in resistivity, conductivity and Hall mobility may be consequence of the variation of the substrate temperature which is associated with the changes in grain size and boundry.

The main effect of oxygen absorption causes a decrease in the Hall Mobility and a increasein the resistivity of thin films. Therefore, the observed low mobility and high resistivity seem to be a consequence of the effect of chemisorption although the smaller grain size is crucial in providing the larger surface area for the process to take place effectively. Oxygen molecules are known to be first physically adsorbed onto the CdS, CdSe and ZnSe thin film surface and transition from physical to chemical adsorption then takes place by the capture of conduction band electrons. Therefore, chemisorption effects on the mobility are attributed to the chemisorption of oxygen at the grain boundaries which alters the barrier height and barrier width. Because of the small grain boundary area compared to the film surface, however, the change in the electron density should be attributed to the chemisorption of oxygen at the film surface. Under photoexcitation, the adsorbed oxygen at the film surface and at the grain boundaries acts as additional recombination centers [108].

2.12 Conclusions

In this work, semiconducting CdS, CdSe and ZnSe thin films were fabricated for different substrate temperature by using spraying plyrolysis and electrodeposition method and their growth conditions, crystal structure, optical and electrical properties were investigated in detail using different techniques.

In the spraying pyrolysis method, the thin film quality is strongly dependent on the substrate, the substrate temperature, the distance between the nozzle and substrate and the flow rate of the chemical solution. It was found that the high quality sprayed semiconducting CdS, CdSe and ZnSe thin films could be obtained on a glass substrate at 380^0C, 420^0C and 430^0C substrate temperature and the corresponding flow rates of 0.5 ml, 0.5ml and 0.3.ml per min, respectively. The distance between nozzle and substrate in all the processes was adjusted to be 20 cm.

In the electrodeposition process, the film quality is strongly dependent on the applied potential during the deposition process, pH value of the chemical solution, deposition time, the temperature of chemical solution and the quality of the substrate and stirring rate of the chemical solution during the deposition process. It was observed that the high quality CdS thin films could be obtained at the applied potentials of 0.65-0.75 V, for a deposition time of 30-60 min, at a pH value of 1-2, at the temperature of the solution at 70-75^0C and for the stirring rate at 400-600 rpm. For high quality CdSe thin films could be obtained at the applied potential of 0.55-0.60 V, for a deposition time of 30-60 min, at a pH value of 2.1-2.6, for the temperature of the solution at 60-65^0C and the stirring rate at 400-600 rpm. A high quality ZnSe thin film could be obtained at applied potential of 0.60-0.70 V, a deposition time of 80-120 min, a pH value of 2.0-2.5, the temperature of the solution at 65-70^0C and the stirring rate at 400-600 rpm.

The optical properties of the semiconducting CdS, CdSe and ZnSe thin films were calculated from optical measurement data. The band gaps of CdS, CdSe and ZnSe thin film samples were found as 2.44 eV, 1.76 eV and 2.68 eV, respectively. The crystal structures of the CdS, CdSe and ZnSe semiconducting thin films were investigated by x-ray powder diffractometer and their main diffraction peaks are found to be in agreement with other studies [21, 28, 64, 65].

The electrical properties of sprayed CdS, CdSe and ZnSe thin films were investigted by using Van der Pauw method. It is found that, the high quality semiconducting CdS, CdSe and ZnSe thin films were developed at 380^0C with $3.93x10^5$ ohm-cm resistivity and 28 $cm^2/Vsec$ Hall mobility, at 420^0C with $5.8x10^5$ ohm-cm resistivity and 44 $cm^2/Vsec$ Hall mobility and at 430^0C with $57.9x10^5$ ohm-cm resistivity and 0.51 $cm^2/Vsec$ Hall mobility, respectively.

In this study, all semiconducting sprayed thin films were developed under the influence of the atmospheric conditions, therefore, the quality of the thin films samples are affected from the oxygen absorption during the deposition process. The main effect of oxygen absorption on the samples is a reduction of the Hall mobility and an increase of the resistivity. Oxygen molecules are known to be first physically adsorbed onto the CdS, CdSe and ZnSe thin film surface and transition from physical to chemical adsorption then takes place by capture of conduction band electrons [39]. Therefore, chemisorption effects on the mobility are attributed to the chemisorption of oxygen at the grain boundaries, which alters the barrier height and barrier width. Because of the small grain boundry area compared to the film surface, however, the charge in electron density should be attributed to the chemisorption of oxygen at the film surface. Under photoexcitation, the adsorbed oxygen at the film surface and at the grain boundaries acts as additional recombination centers [40]. And also it is suggested that the resistivity and the Hall mobility of the samples are strongly dependent on the substrate temperature.

And also in this work, electrodeposition and spraying pyrolysis method are found to be very suitable methods for high quality and low cost semiconducting thin film growth. These methods don't require complex systems and sophisticated equipments. Electrodeposited CdS, CdSe and ZnSe thin films were developed on conducting substrate (nickel plate) which causes a short cut effect in the current flow therefore it was not possible to measure the electrical properties of these films and it was not possible to investigate the required properties of the samples. As mentioned in the previous section we could'nt measured the electrical properties of the electrodeposited semiconducting thin films grown on to conducting substrates. So our recommendation will be that the ITO substrate must be used as a substrate to able to measure the electrical properties of these kind of thin film samples.

In recent years, electrodeposited and sprayed semiconducting thin films have been investigated intensively, in part because of its low cost industrial importance in the microelectronic, solar cells, detectors, light emitting devices industry. Hence, it is our recommendation that a new study should be under taken to determine the optimum conditions on the film growth of the CdS, CdSe and ZnSe and other II-VI compound thin films by changing some growth parameters and substrate.

The sprayed and electrodeposited CdS, CdSe and ZnSe thin films obtained in this work exhibited a near-ideal direct band gap, and high photosensitivity in the visible range of the solar spectrum. Therefore, these materials can be advantageously used in the applications of low cost solar cells and photo-electronic materials, detectors, light emitting devices.

CHAPTER III

METALIC FILM

3.1. Introduction

Thin films show different physical properties from bulk materials. So far a number of theoretical and experimental investigations have been carried out to develop different types of thin films for various purposes. Different techniques have been used to produce thin films such as moleculer beam epitaxy, screen printing, chemical vapor deposition, evaporation, elecrodeposition, spraying pyrolysis and sputtering techniques [22,24]. Every process has some distinct advantages and disadvantages in terms of material quality and suitability to device fabrication and cost. Electrodeposition and spraying pyrolysis methods are simple techniques which have been gaining importance in recent years for producing relatively cheap good quality films for device applications [5,10].

In recent years, electrodeposition has become a mature technology for materials deposition in microelectronics fabrication and for related applications. Whereas 10-15 years ago, electrodeposition was looked upon as a dirty, low-cost method, it is now considered to be a clean technique while it has maintained its cost advantage over more traditional methods such as sputtering or evaporation [73].

Electrodeposition is a very attractive method for the growth of metallic and semiconducting thin film materials. It is a simple technique which lends itself to large-scale production. It does not require specialized expensive equipment. Material utilization in the electrodeposition technique is extremily good since plating takes place only on the substrate. Electrodeposition can produce high purity materials if special attention is paid to the purification of the plating solutions which can be achieved by pre-electrolysis [2,8,20].

Electrodeposited magnetic thin films are important in computer read/write heads and microelectromechanical systems due to their flexibility, capability, quality, and low cost. Electrodeposited permalloy (80Ni20Fe) has been the alloy of choice in thin film recording heads. However, as the real density of computer drives has increased dramatically (60% per year), new higher performance soft magnetic materials are needed. Some resourcers reviewed requirements for improved thin film recording heads. These include: (i) high magnetic saturation (B_s>>1 T), (ii) low coercivity (H_c<1 Oe), (iii) optimal anisotropy field (H_k), for high permeability (μ), (iv) close to zero magnetostriction (λ), (v) high electrical resistivity (ρ), and (vi) good corrosion resistance [74].

The electrodeposition of NiFe has been investigated intensively over the last few decades, in part because of its industrial importance in the microelectronic industry. An increase in recording media coercivity leads to an increase in the required saturation magnetization, B_s, of the pole materials beyond those of conventionally used magnetic materials (1.0 T $Ni_{80}Fe_{20}$ or 1.6 T $Ni_{45}Fe_{55}$) in the magnetic recording head. NiFe alloys have important magnetic properties. Permalloy ($Ni_{80}Fe_{20}$) is the most common soft magnetic film, which has zero magnetostriction (λ=0), a large magnetoresistive effect (~5%), relative high magnetic saturation (M_s=1.0 T) with low coercivity, high magnetic permeability, and low hysteresis loss [75,76].

In this study, NiFe films are prepared using electrodeposition technique. The compositions, structures, magnetoresistance and magnetic properties were investigated by using different techniques..

3.2 Literature Survey of NiFe Alloy Films

The magnetic properties and the magnetoresistance in correlation with microstructural properties of permalloy monolayer and [NiFe(t)/Cu(s)/NiFe(t)] or [NiFe(t)/Mo(s)/NiFe(t)] multilayers have been investigated by J.Neamtu and M.Volmer [76]. The thickness (t) of NiFe layers was ranged from 4 to 12 nm, while the copper and molybdenum layers (s) were ranged from 3 to 8 nm. The multilayers exhibit magnetoresistive properties different from those of permalloy film. By decreasing the NiFe layer thickness and increasing the non-magnetic interlayer thickness, the influence of interfacial (intermixing) effects on magnetic properties become more important. Although the thickness of layers is the leading part for magnitude of GMR effect, the microstructural properties of interfaces and the grain boundaries scattering must not be neglected.

The oxidation of sputtered NiFe(20 wt.%, Permalloy) thin films with a thickness of 180 nm was studied during annealing up to 400^0C for 2 h in air [77]. The composition and the thickness of the oxide layer and the compositional change in the NiFe alloy layer as well as the microstructure of the film were investigated by Auger electron spectroscopy, X-ray diffraction, and transmission electron microscopy. Distinct oxidation starts at about 300^0C. The formed oxide layer consists of Fe_2O_3. The Fe concentration in the NiFe layer decreases with the oxidation which leads to changes of the properties of this layer.

L.Vila, W.Park, and their co-workers have been studied the current perpendicular magnetoresistances properties of NiFe and NiFeCo Permalloys. They measured the specific resistances of NiFe and NiFeCo. They concluded that the low temperature GMR parameters of $Ni_{66}Fe_{13}Co_{21}$ are similar to the Ni_{80} Fe_{20}. More detailed analysis gives that the resistivity of $Ni_{66}Fe_{13}Co_{21}$ is 90 nΩm is slightly smaller than the equivalent value for $Ni_{84}Fe_{16}$. Since there is no a priori reason to expect the GMR performance of NiFeCo to decrease more rapidly with temperature than that of NiFe, NiFeCo looks likely to be a viable alternative to NiFe for technological uses [78].

A systematic study of longitudinal and transverse magnetoresistance in $Cu_xZn_{1-x}Fe_2O_4$ system with x=0.0, 0.25, 0.50,0.75, 1.0 has been carried out to find out the optimal highest resistive state for practical applications [79]. The variation in magnetoresistance is of the first-order effect as in semiconductors. The effect of compositional variation on saturation magnetization, remanence and coercivity at room temperature were also reported. It has been observed that the highest resistive state appears at the field value for which the saturation magnetization exists for each concentration.

The microstructural and crystallographic characteristics of electrodeposited soft magnetic CoNiFe thin films were investigated by transmission electron microscopy by H.S.Nam and his co-workers [80]. Dark field images showed that the film with fcc-bcc dual crystals has a smaller grain size than the fcc or bcc single phase film. The fcc films were found to have a unique microstructure with twin-like stacking faults with relatively uniform grain size distribution, and such twins were also found in the dual phase films. It is suggested from the diffraction patterns that the fcc and bcc components of the films are substitutional solid solutions of Co, Ni and Fe. The lattice constants of fcc CoNiFe films were determined by atomic concentrations of the three elements.

The coercivity behaviour of the $Ni_{81}Fe_{19}$ film exchange-coupled with an antiferromagnetic CoO underlayer has been investigated systematically by C.J.Wang and L.Wu-Yan [81]. It has been found that the coercivity is greatly enhanced not only in the easy axis direction but also in the hard axis direction when the temperature is below the Neel temperature of CoO. Also, the thickness dependence of coercivity at low temperature follows the scaling relation as $1/t_{NiFe}^{\alpha}$ with α=2.5 at the hard axis, which is quite in contrast with the case of easy axis, i.e. α=1.5, predicted theoretically and verified experimentally previously. The increase of the temperature leads to the decrease of the coercivity at both the easy and hard axes .

L.Tie and S.H.Lie have obtained and investigated the magnetic behaviours of the ferromagnetic layer in the symmetric spin valves of Co/Cu/NiFe and NiFe/Cu/Co by measuring with a vibrating sample magnetometer and analyzing in terms of the multi-domain Ising model. It has been found that some magnetic layer can have quite different magnetic behaviours in different structures of spin valves, depending on the properties of the under-layer. In their investigation, they have found that the magnetic behaviour of a Co layer depends mainly on the magnetization of the under-layer, whereas this is not the case for the NiFe layer. It is interesting that the NiFe and Co layers with same thickness present different magnetic behaviours in different structures of spin valves [82].

The magnetostatic coupling in lithographically defined 25 n thick $Ni_{80}Fe_{20}$ wire arrays has been investigated using magnetoresistance (MR) measurements by A.O. Adeyeye, R.P. Cowburn and M.E. Welland [83]. A DC current of 1 mA was passed along the wire of each array and the resistance was recorded automatically using a four-terminal method as the magnetic field was swept. The magnetic field was applied in the film plane and at room temperature. They observed a novel MR response when the applied field is along the easy axis of the wire. For the field applied along the hard axis of the wire, the shape of the MR response is found to be strongly dependent on the inter-wire magnetostatic interactions.

Ni, Fe and NiFe alloy films were electrodeposited at a polycrystalline Au surface using a range of electrolytes and potentials by N. Myung [84]. In this study, the plating efficiency of NiFe alloy films was computed with the aid of ICP spectrometry. In general, plating efficiency increased to a steady value with deposition time. Plating efficiency of Fe was lower than that of Ni at –0.85 and –1.0 V but the efficiency approached to the similar plateau value to that of Ni at more negative potentials. The films with higher content of Fe showed different stripping behaviour from the ones with higher content of Ni. Finally, compositional data and real-time plating efficiency were presented for films electrodeposited using a range of electrolytes and potentials.

The properties of soft magnetic CoNiFe films electrodeposited in the presence of saccharin and sodium lauryl sulfate additives were studied in terms of their thickness and substrate dependence by I. Tabakovic and his co-workers [85]. The properties of soft magnetic CoNiFe films with B_s=1.64-1.85 T were studied at different thickness and substrate materials. The characteristic compositional gradient with higher Fe content in the deposit at the substrate interface during the electrodeposition of NiFe alloys was not found with CoNiFe alloy. The crystal structure of electrodeposited

CoNiFe films is mixed bcc+fcc phase with larger amounts of bcc and larger average grain sizes close to the 1.0 T NiFe substrate. The measured average stress and coercivity of CoNiFe films is both substrate and thickness dependent. The mechanism of coercivity of these magnetic films is governed by magnetoelastic anisotropy, grain size, and/or exchange coupling between two ferromagnetic layers.

The effect of different seed layers on the magnetoresistive (MR) properties of NiFe films has been investigated and significant improvements can be observed and explained by H. Gong and his co-workers [86]. By choosing seed layers that vary from conducting to insultating and from amorphous to crystalline the role of the NiFe crystalline texture and current shunting via the seed layer on the MR ratio is observed. In this study, thin $Ni_{81}Fe_{19}$ films with thicknesses ranging from 60-1000 A^0 were sputter-deposited on various seed layers of varying conductivity and crystallinity. The choice of the permalloy film as the magnetic layer is because that permalloy is a critical layer used in most MR and GMR applications. Moreover, its cubic fcc crystalline structure is typical for most of the soft magnetic materials employed in MR and spin-valve structure.

Magnetic multilayers $[Ni_{80}Fe_{20}/Cu]_{15}$ grown by dc-magnetron sputtering and annealed at 150^0C and 250^0C were investigated by low-angle and high–angle X-ray diffraction by M.Xu, C.Chai and at all [87]. It was found that the superlatice period decreases upon annealing, while both the interfacial roughness and (111) preferred orientation increase with increasing annealing time. The computer simulation of high-angle X-ray diffraction firstly revealed a very thick intermixing layer located between the $Ni_{80}Fe_{20}$ and Cu sublayers, and its thickness increases with increasing annealing time. The above results on microstructures of $[Ni_{80}Fe_{20}/Cu]_{15}$ multilayers were discussed.

Magnetoresistance of a permalloy monolayer and NiFe(t)/Cu(s)/NiFe(t) multilayers has been investigated in correlation with their microstructural properties by J.Neamtu, M.Volmer, and A.Coraci [88]. The thickness, t, of NiFe layers ranged from 4 to 12 nm, while that of the copper layer,s , was ranged from 3 to 18 nm. The multilayers exhibit magnetic properties different from those found in a single NiFe film, such as the gaint magnetoresistance effect (GMR). By decreasing the NiFe layer thickness and increasing the Cu layer thickness, the influence of interface intermixing effects on magnetic properties becomes more important. The GMR effect is influenced by the grain size of the NiFe layer. In this study, the magnetic properties of permalloy films and NiFe/Cu multilayers were measured with a vibrating sample magnetometer (VSM), at room temperature.

Samples of nanocrystalline Ni-20%Fe permalloy, obtained by electrodeposition, were studied using an X-ray diffraction technique and magnetic force microscopy. After deposition, the alloy exhibited strong fiber texture with the major component being (100) and a lesser contribution from (111). An increase in deposition current density led to a reduction in the strength of the (100) texture. Despite the small magnitude of the magnetic interaction, images of magnetic domains were obtained using magnetic force microscopy. The images were, however, unstable and changed significantly with the scanning time. Annealing of the permalloy above 573 K caused rapid grain growth and a transformation of the (100) fiber to (111) fiber. Numerical analysis of the texture data was conducted to assess the atomic structure of grain boundaries in the as-deposited and annealed states [89].

The room temperature magnetization, magnetoresistance and structural properties of soft magnetic $Fe_{26}Ni_{74}$ nanowires of 18 nm diameter and various lengths electrodeposited in the pores of anodic alumina were investigated by H.R.Khan and K.Petrikowski [90]. Nanowires show perpendicular magnetic anisotropy, anisotropic crystallographic and magnetoresistance behaviour with a coercivity of 967 Oe and a remanence value of 85%. It should be noted that an electrodeposited $Fe_{26}Ni_{74}$ layer (6μm) on a copper substrate shows in-plane anisotropy and a coercivity of less than 1 Oe. XRD spectra show strong <111> texture with only a weak trace of the NiFe peak, and observable (111) NiFe peak for as-deposited and annealed samples, respectively.

Y.Shimazu and his co-workers measured the magnetoresistance (MR) of ferromagnetic films of nonuniform thickness. The samples were designed so that the anisotropic magnetoresistance (AMR) effect gave a positive contribution to the MR in contrast to the case of thin wires. The result suggests a positive contribution of the domain walls to resistivity. For ferromagnetic wires of micron-range diameter with diameter fluctuations, they observed Barkhausen noise at room temperature which also indicates the domain wall effect [91].

N.V.Myung and K. Nobe studied on electrodeposition iron group thin film alloys and evaluated for properties including corrosion resistance, microstructure, electrical resistivity, magnetoresistance and other magnetic properties. Corrosion resistance depends on deposit composition and microstructure, which were controlled by solution composition and deposition variables. Maximum corrosion resistance was observed for 50Ni50Fe and 70Co30Ni binary alloys. Considerable improvement in the corrosion resistance of bulk NiFe alloys with increased Ni content was observed. The electrical resistivity and magnetoresistance of the electrodeposited films were determined by the standard four-point probe dc current technique in the presence and absence of an external magnetic field of 1500 Oe. Magnetic properties of electrodeposited films were measured with a vibrating sample magnetometer. Electrodeposited NiFe films from sulfate baths show superior soft magnetic properties including both lower coercivity and higher squareness than from chloride baths. Magnetic saturation (M_s) of electrodeposited NiFe films follows that of bulk alloys where magnetic saturation increases with increasing deposit Fe content [92].

3.3. Metalic Films

3.3.1. Introduction

The phonomenon of magnetism in materials plays an important part in our daily experience. It extends from the permanent magnets used to latch our refrigerator door to the magnetic memory elements of our most sophisticated computers. Magnetic materials are important industrial materials necessary for many engineering desings, particularly in the area of electrical engineering.

There are two general types of magnetism in materials. The first of these is a class we can call induced magnetism. In this class, the material is magnetized only when there is an applied magnetic field. Diamagnetism and paramagnetism are two forms of induced magnetism. The second general class of magnetic phenomena is refered to as spontaneous magnetism. As the name implies, spontaneous magnetism refers to the ability of a material to be magnetized and to retain its magnetic state even in the absence of an applied magnetic field [81]. Ferromagnetism and antiferromagnetism are the common examples of this form of magnetic phenomena. Almost all magnetic materials that have important engineering applications belong to this class. Spontaneously magnetized materials may be further classified with respect to the form of their use. In generally there are two main types; soft and hard magnetic materials. Materials that can be magnetized and demagnetized easily are called soft magnetic materials [82]. Materials such as silicon-iron and permalloy (iron-nickel alloy) are soft magnetic materials commonly used for transformers cores and for applications in which the material must be easily magnetized and demagnetized such as in magnetic read-write heads, magnetic memories, small electronic transformers, stator and rotor materials for motors and generators [83,93].

By contrast, hard magnetic materials can be magnetized only by the application of strong magnetic fields and once magnetized are difficult to demagnetized. Hard magnetic materials are used for applications requiring permanent magnets which do not demagnetize easily such as the permanent magnets in loudspeakers, telephone receivers, synchronous and brushless motors, and automotive starting motors [93,94].

3.3.2. Magnetic Properties of Materials

3.3.2.1. Basic Concepts and Definations

The magnetic properties of materials arise from the spin of electrons and the orbital motion of electrons around atomic nuclei. Since a moving charge set up a magnetic field around it, the moving and spinning electrons act as tiny magnets. In many atoms the opposite spins neutralize one another, but when there is an excess of electrons spinning in one direction, a magnetic field is produced. Except for ferromagnetic materials, which can form permanent magnets, all substances exhibit magnetic effects only when subjected to an external electromagnetic field.

The external field is characterized by the magnetic field strength H and the magnetic induction B. The magnitude of the magnetic induction is defined by the number of hypothetical induction lines per unit area normal to the their direction and is measured in gauss units. The magnetic induction is also referred to as the flux density, because the induction at a point equals the flux per unit area.

The magnetic field strength, called also the magnetic intensity or magnetizing force, can be represented, like the magnetic induction, by lines of magnetization. The magnetic field H is measured in ampere-turns per meter or inch, or in oersteds (1 oersted is 2,015 ampere-turns/in.) [95]. Magnetization or magnetic moment Per unit volume is the product of the magnetic moment of each atom and their number in a unit volume. The ratio of the magnetization to the applied magnetic field is called magnetic susceptibility;

$$\chi \equiv \frac{M}{H} \tag{3-1}$$

Magnetization M, magnetic field H, and induction B are related through the equation

$$B = H + 4\pi M \tag{3-2}$$

Permeability is a measure of the ability of material to be magnetized or the ease with which a magnetizing force H can induce a flux density B in a magnetic circuit. The permeability is numerically equal to B/H, but the relation between B and H is very complex. Hence the ratio B/H can not be determined analytically, but it is represented by an experimental curve.

$$\mu = \frac{B}{H} \tag{3-3}$$

All materials can be characterized as being either diamagnetic, paramagnetic, or ferromagnetic, depending on their behavior under the influence of a magnetic field, as seen in Figure 3.1. Furthermore, antiferromagnetic and ferrimagnetic materials are distinguished as subclasses of ferromagnetic materials. Diamagnetic substances are composed of atoms which do not have permanent magnetic moments but only field induced weak magnetic moments. Ionic solids and molecular solids are generally diamagnetic. Paramagnetic substances arise because the atoms or ions posses and odd number of electrons which give rise to a residual permanent magnetic moment. Atoms with even numbers of electrons may be paramagnetic if some of the inner electron shells are incomplete (Fig.3.1(a)) [96].

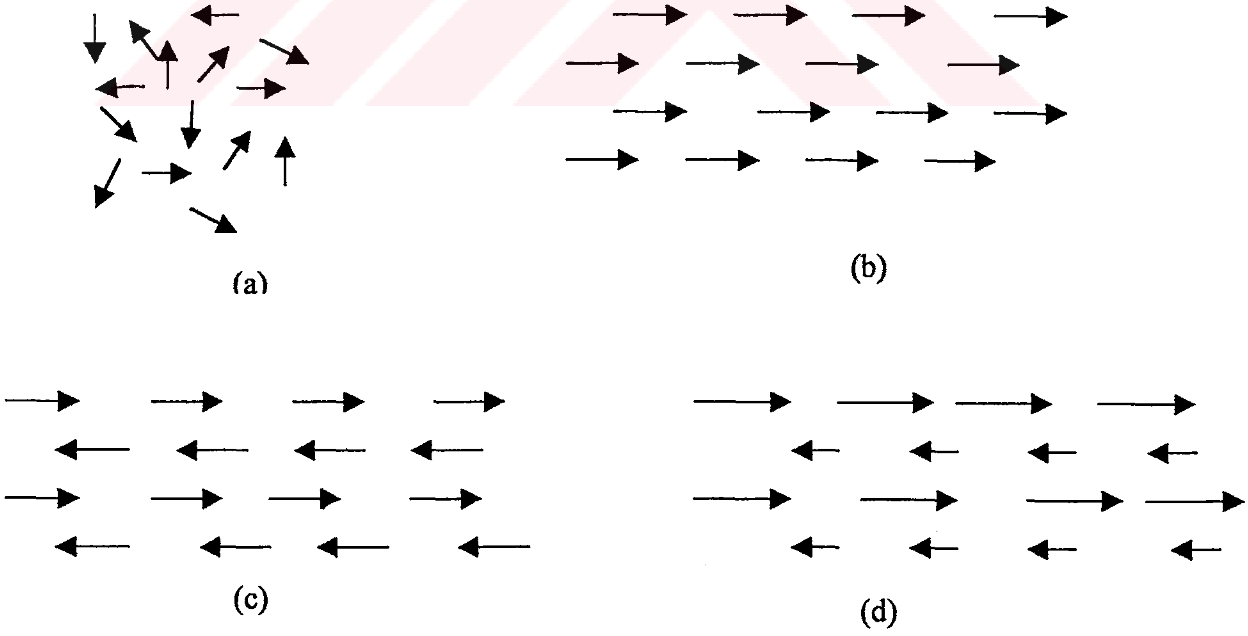

Figure 3.1 Four kinds of magnetism with various interatomic interaction: (a) paramagnetism, (b) ferromagnetism, (c) anfiferromagnetism, and (d) ferrimagnetism

Ferromagnetic substances exhibit a spontaneous magnetic moment which exist even in the absence of an applied magnetic field. Iron, nickel, and cobalt, as well as some of their oxides and carbides, exhibit pronounced ferromagnetic properties; gadolinium, a rare-earth element, also has ferromagnetic properties at a lower temperature. Ferromagnetism arises only when interactions between adjacent atoms or ions in a crystal are strong enough to hold magnetic moments of the neighboring atoms parallel to each other in spite of thermal agitation as seen in Figure 3.1(b). Ferromagnetism is found solely in elements possessing an incomplete energy level such as the 3d level in iron, cobalt, and nickel, and the 4f energy level in gadolinium. However, not all elements containing incomplete energy levels are ferromagnetic. Antiferromagnetism arises from an antiparallel locking of spins which results in a negative interaction between the nearest neighbors as seen in Figure 3.1(c). When the magnetic moments are not equal, the antiparallel arrangement results in ferrimagnetism as seen in Figure 3.1.(d).

The metals iron, cobalt, and nickel are the only three elemental metals which when magnetized at room temperature can produce a strong magnetic field around themselves, and are said to be ferromagnetic. The ferromagnetic properties of the transition elements Fe, Co, and Ni are due to the way the spins of the inner unpaired electrons are aligned in their crystal lattices. In Fe, Co and Ni the unpaired inner 3d electrons are responsible for the ferromagnetism which these elements exhibit. The iron atoms has four unpaired 3d electrons, the cobalt atom three, and the nickel atom two shown in Figure 3.2 [74,93].

Unpaired 3d electron	Atoms	Num.of the electrons	Electronic cofiguration				
4	Fe	26	↑↓	↑	↑	↑	↑
3	Co	27	↑↓	↑↓	↑	↑	↑
2	Ni	28	↑↓	↑↓	↑↓	↑	↑

Figure 3.2 Magnetic moments of Fe, Co and Ni atoms of 3d transition elements

In a solid sample of Fe, Co, or Ni at room temperature, the spins of the 3d electrons of adjacent atoms align in a parallel direction by a phenomenon called spontaneous magnetization as shown in Figure 3.3. This parallel alignment of atomic magnetic dipoles occurs only in microscopic regions called magnetic domains.

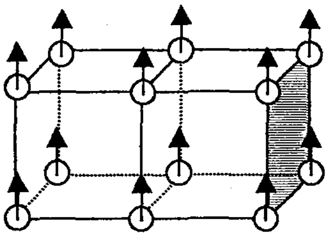

Figure 3.3 Ferromagnetic iron, which has the bcc structure

The origin of the force which aligns the moments in metals is still a major research problem but it is known to arise from the wave mechanical nature of electrons and it is related to the force which aligns the spins of electrons in a partly filled atomic shell [94].

3.3.3. Exchange Energy

Ferromagnetic materials have spontaneously magnetized regions which are called magnetic domains. The reason behind the spontaneous magnetization is exchange energy which is represented by the following equation

$$E = -J\vec{s}_1\vec{s}_2 \tag{3-4}$$

where J is the exchange integral, s_1 and s_2 are the atomic spins.

It is recalled that the exchange energy in a ferromagnetic is lowest when the magnetic dipoles are aligned in a parallel fashion (antiparallel for the case of antiferromagnetic materials). This means that if only the exchange energy is consedered, each and every atomic dipole within the solid would be expected to adopt the same orientation. The effects of the exchange energy can be likened to strong springs connecting all the dipoles and forcing them into parallel alignment.

3.3.4. Curie Temperature (T_c)

Magnetization is a temperature dependent quantity. The behaviour of magnetization as a function of temperature can be seen in Figure 3.4.

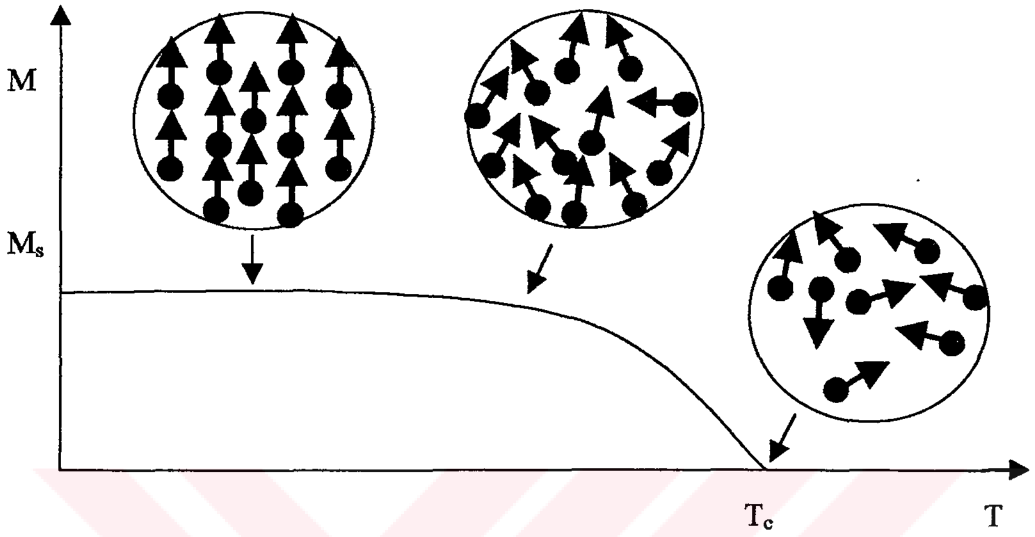

Figure3.4 Effect of temperature on the saturation magnetization M_s of a ferromagnetic material below the Curie temperature T_c

Thermal fluctuations of magnetic dipoles become so significant that the effects of the exchange energy are no longer evident and ferromagnetism disappears altogether. Above the Curie temperature (T_c), the material behaves paramagnetically since the dipoles are bougth into partial alignment only by the application of external fields [97].

When a sample of a ferromagnetic material is cooled from a temperature above its Curie temperature ferromagnetic domains reform and the material becomes ferromagnetic again. The Curie temperature of Fe, Co, and Ni are 770, 1123 and 358^0C, respectively.

The exchange energy that produces the dipole alignment is counteracted by the randomizing effects of thermal energy are more important at high temperature and eventually cause a significant reduction of the intensity of magnetization, as seen schematically and graphically in Figure 3.4.

3.3.5. Magnetostatic Energy

The magnetostatic energy of a magnetized sample is given as

$$E_{mag} = \frac{1}{8\pi}\int_{v} H_d^2 dV \tag{3-5}$$

where H_d is the demagnetizing field, dV is the volume element.

For a ferromagnetic material, a single domain structure has the highest potential energy. This potential energy is reduced by domain formation. The greater number of antiferromagnetically coupled domains results in the smaller magnetic potential energy.

Consider the sample shown in Figure 3.5 (a), (b) and (c). The pattern in Figure 3.5 (a) has the highest energy while the other patterns in Figure 3.5 (b) and (c) have less energy because of the domain numbers [98].

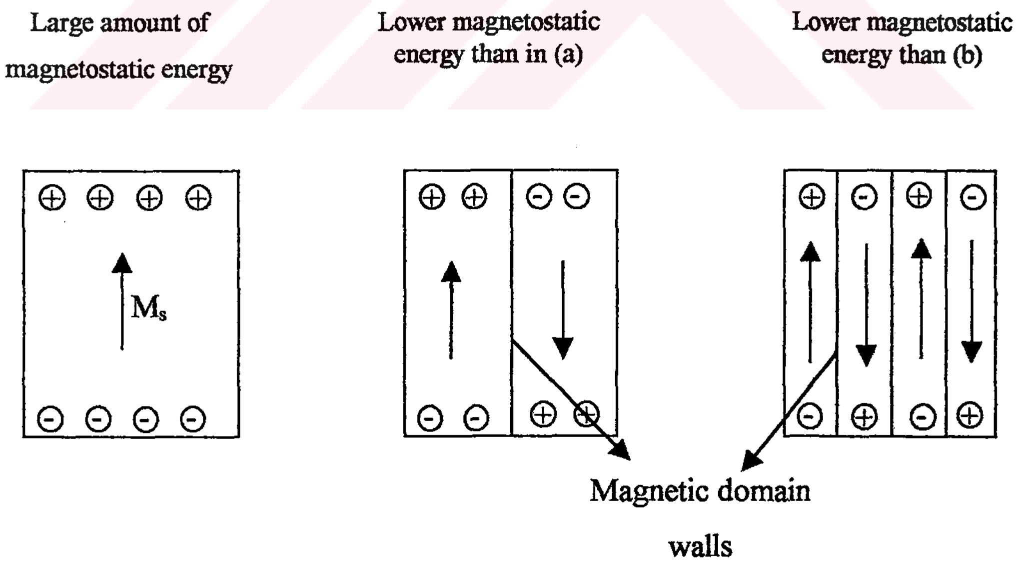

(a)
One Domain

(b)
Two Domains

(c)
Four Domains

Figure 3.5 Illustration of the external magnetic field associated with various domain patterns

3.4 Hysteresis Properties of Ferromagnetic Materials

3.4.1 Determination of Hysteresis Loops

The hysteresis loop for a ferromagnetic and ferrimagnetic material can be obtained by measuring the intensity of magnetization M or the induction field B as a function of the applied field H. It is conventional to permit the applied field to cycle between positive and negative values and to record the entire cycle. Consider the circuit elements shown in Figure 2.6 and initially unmagnetized sample [93,98].

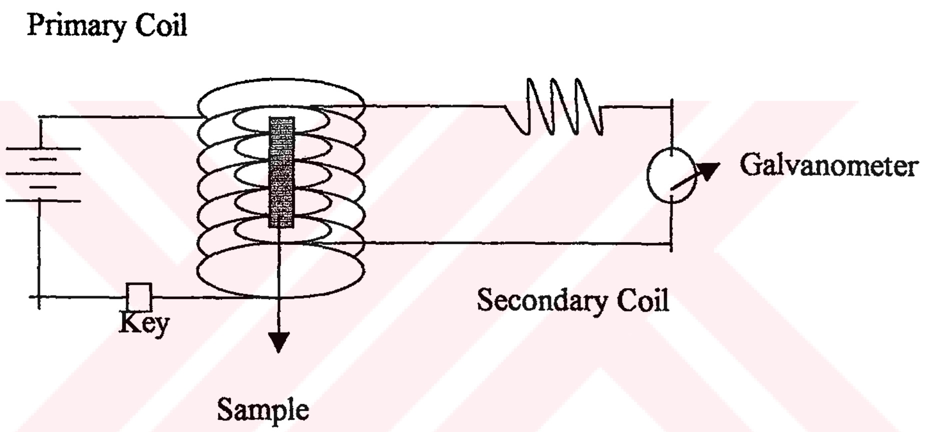

Figure 3.6 Electrical circuit ased for determininig the B-H relationships for ferromagnetic materials

When a direct current is allowed to flow in the primary coil, a uniform magnetic field is produced within the coil, and the sample responds by developing a magnetic moment. The magnetic flux lines associated with the magnetization of the sample induce a charge or current in the secondary coil that can be easily measured with galvanometer. Each time either the field is abruptly changed or the sample is vibrated with a certain frequency, the magnetization or magnetic flux in the sample changes and a fixed, measurable charge is induced into the secondary. A complete record of magnetization of the sample as a function of the applied magnetic field can be obtained by keeping a running account of the increments in the magnetization or induction each time the field is changed. Using this technique, it is possible to determine the entire magnetic hysteresis loop by varying the applied magnetic field from positive to negative values. The general features of the hysteresis loop are shown in Figure 3.7.

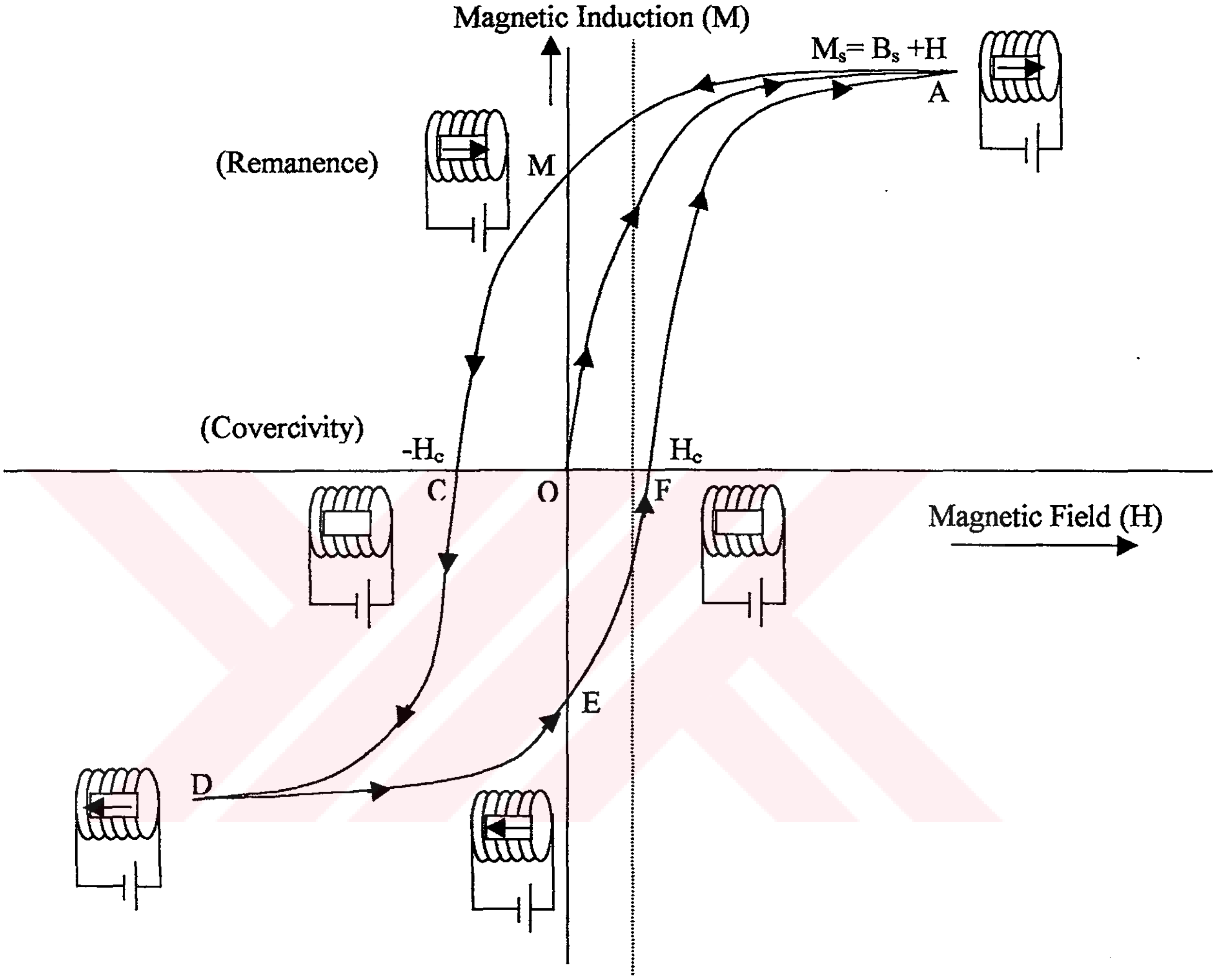

Figure 3.7 Hysteresis loop for a ferromagnetic material

The hysteresis loop shown in Figure 3.7 corresponds to the magnetization of a ferromagnetic sample that is initially unmagnetized. As the magnetic field is applied to the sample, the magnetization usually follows a smooth but curved path such as OA.Usually the magnetization builds up by an S-shaped curve. When the applied field is sufficiently strong, the sample begins to saturate; that is the intensity of magnetization in the sample approaches the saturation magnetization M_s.

Now let us consider what happens when the magnetic field intensity begins to decrease. The hysteresis loop indicates that the magnetization does not follow the initial magnetization curve AO. Rather, it follows the hysteresis loop along AB. When the magnetic field is reduced to zero, the sample remains partially magnetized. At this point the residual magnetization in the sample is called the remanent magnetization M_r; B_r is the corresponding remanent induction field. Now, if the magnetic field is reversed, the sample will be forced to demagnetize along BC. As indicated by the hysteresis loop, a critical field called the coercive field H_c, is required to reduce the magnetization or induction B to zero [97]. If the magnetic field is increased negatively beyond the coercive field, the sample begins to develop a negative magnetization along CD. Eventually, when the reverse field is sufficiently strong, the sample begins to saturate in the reverse direction.

Now, if the reverse field is decreased, the magnetization again lag behind the changes in the applied magnetic field and the magnetization follows the path DE. The magnetization is $-M_r$ when the reverse field reduces to zero. When the magnetic field is reversed for the second time (becoming positive again), the magnetization follows EF. Again, a critical field H_c is needed to eliminate the remanent magnetization. If the magnetic field is continually increased, the sample eventually saturates again in the positive direction along FA. The sample has now been returned to the same state that was produced by the initial magnetization. Hereafter, each time the magnetic field oscillates between positive and negative values, the magnetization follows the hysteresis curve as shown in Figure 3.7 [98].

This discussion of the hysteresis curve indicates that the magnetization is history dependent. When the hysteresis loops are rectangular in shape, as in the case of some ferrites, there are two limiting magnetic states (i.e., $+M_s$ or $-M_s$) in which the material can exist. By simply applying a magnetic field of the proper sign, the material can be switched from one state to the other. In this way, these materials can be used as memory elements for computers [74,95,98].

3.5. Magnetic Anisotropy

3.5.1 Physical Origion of Crystal Anisotropy

Crystal anisotrpy is due mainly to spin-orbit coupling. By coupling is meant a kind of interaction. Thus we could speak of the exchange interaction between two neighboring spins as a spin-spin coupling. This coupling is very strong and keeps neighboring spins parallel, or antiparallel, to one another. But the associated exchange energy is isotropic; it depends only the angle between adjacent spins and not all on the direction of the spin axis relative to the crystal lattice. The spin-spin coupling therefore cannot contribute to the crystal anisotrpy.

The orbit-lattice coupling is also strong. This means, in effect, that the orientations of the orbits are fixed very strongly to the lattice, because even large fields cannot change them. There is also a coupling between the spin and the orbital motion of each electron. When an external field tries to reorient the spin of an electron, the orbit of that electron also tends to be reoriented. But the orbit is strongly coupled to the lattice and therefore resists the attempt to rotate the spin axis. The energy required to rotate the spin system of a domain away from the easy direction, which we call the anisotropy energy, is just the energy required to overcome the spin-orbit coupling. This coupling is relatively weak, because fields of a few hundred oersteds are usually strong enough to rotate the spins.

The strength of the anisotropy in any particular crystal is measured by the magnitude of the anisotropy constants K_1, K_2, etc. Nor is there any simple relationship between the easy, or hard, direction of magnetization and the way atoms are arranged in the crystal structure. Thus in iron, which is body-centered cubic, the direction of greatest atomic density, i.e., the direction in which the atoms are most closely packed, is <111>, and this is the hard axis. But in nickel (face-centered cubic) the direction of greatest atomic density is <110>, which is an axis of medium hard magnetization. And when iron is added to nickel to form a series of face-centered cubic solid solutions, the easy axis changes from <111> to <100> at about 25 percent iron, although there has been no change in crystal structure [97-99].

The total energy of the film in an applied magnetic field with components H_x and H_y in the easy and hard directions is

$$E_T = -M_s H_x \cos\theta - M_s H_y \sin\theta + K_u \sin^2\theta \qquad (3\text{-}6)$$

where M_s is the saturation magnetization, θ is the angle between the magnetization vector and easy axis. K_u is the anisotropy constant with units of energy/volume.

In the equilibrium state the magnetization angle is determined by the conditions that

$$\frac{\partial E_T}{\partial \theta} = 0 \quad \text{or} \quad \frac{\partial E_T}{\partial \theta} \rangle 0 \qquad (3\text{-}7)$$

Using the solutions of Eq.(3-7), one can predict the shape of hysteresis loop. When magnetic field is applied along the easy direction a square hysteresis loop is obtained as seen in Figure 3.8.

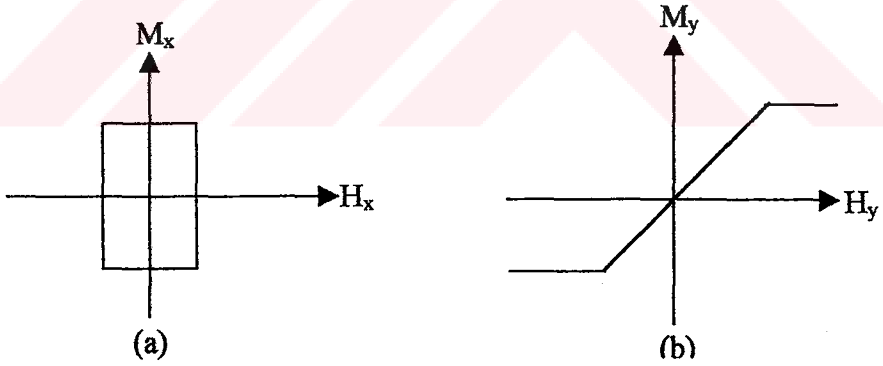

Figure 3.8 Hysteresis loops

When a magnetic field is oriented along the hard direction a hysteresis loop like Figure 3.8 (b) is obtained. Using the hysteresis loops and

$$H_x = \frac{2K_u}{M_s} \quad \text{or} \quad H_y = \frac{2K_u}{M_s} \qquad (3\text{-}8)$$

which are obtained as solutions of Eq.(3-6) and one can obtain the anisotropy constant K_u from these expressions.

3.6. Electrical Resistivity in Metals

Metals have high conductivities because of the large numbers of free electrons that have been excited into the empty states of conduction band above the Fermi energy. Since crystalline defects serve as scattering centers for conduction electrons in metals, increasing their number raises the resistivity (or decreasing lowers the conductivity). The concentration of these imperfections depends on temperature, composition and the degree of cold work of a metal specimen. In fact, it has been observed experimentally that the total resistivity of a metal is the sum of the contributions from thermal vibrations, impurities, and magnetizations. This may be represented in mathematical form as follows;

$$\rho(H,T) = \rho_{(imp)} + \rho_{(phonon)}(T) + \rho_{(mag)}(T)\left[1 - F\left(M/M_s\right)^2\right] \tag{3-9}$$

Sumation of the first and second term of the Eq. (3-9) is defined as,

$$\rho' = \frac{m v_F}{\eta |e|^2 \overline{L}} \tag{3-10}$$

where L is the mean free path between collisions, since this is the most important factor determining the electrical resistivity of a metal and defined as $L = L_{TH} + L_i$. Suppose that mean free path due to the thermal vibrations is L_{TH} and that due to the impurities is L_i. It is clear that when an electron drifts a distance L in a metal, it will have suffered L/L_{TH} collisions due to the lattice vibrations and L/L_i collisions due to impurities. Since the total number of scattering events may be expressed as $L/L_{TH} + L/L_i$, it follows that the mean free path L due to both thermal vibrations and impurity atoms may be expressed by

$$\frac{1}{L}=\frac{1}{L_{TH}}+\frac{1}{L_i} \tag{3-11}$$

The electrical resistivity caused by scattering from lattice vibrations and impurity atoms

$$\rho^{*}=\rho_{(imp)}+\rho_{(phonon)} \tag{3-12}$$

represents a law of additive resistivities and known as Mathiessen's rule [96,99,100].

The electrical resistivity of a metal varies with the metal's temperature in a characteristic manner. This variation is usually discussed in terms of the behaviour of the resistivity ρ versus T. Figure 3.9 shows the observed curve for metals. At $T \cong 0^0$K, ρ has a small constant value; above that, ρ increases with T slowly at first, but afterward ρ increases linearly with T. The linear behaviour continues essentially until the melting point is reached. This pattern is followed by most metals and usually room temperature falls into the linear range.

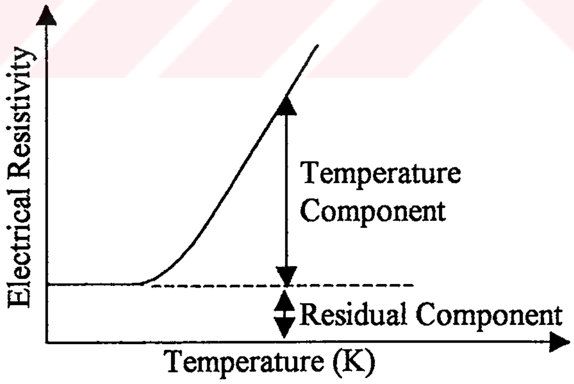

Figure 3.9 Schematic variation of electrical resistivity of a metal with absolute temperature.

In the third term on the left side of Eq.(3.9), F is a function of the argument $(M/Ms)^2$, The function F(x) is monotonic, bounded between 0 and 1, with the limiting values of $F(x)\rightarrow 0$ at $M\rightarrow 0$; and $F(x)\rightarrow 1$ at $M\rightarrow M_s$. The simplest form of F is $F=(M/M_s)^2$ which describes the data well for small values of $(M/M_s)^2$ [101]. The quantity $\rho_{(mag)}(T)$ due to the scattering of conduction electrons from the ferromagnetic entities, has to be addressed theoretically. The quantity $\rho_{(mag)}(T)$ depends on the size and number of the ferromagnetic entities within the mean-free path and the magnetic orientations of the entities are contained in the factor of $[1-(M/M_s)^2]$, [93].

3.7. Magnetoresistance

The magnetoresistance effect is a change in the electrical resistance R of a substance when it is subjected to a magnetic field. The value of $\Delta R/R$ is extermely small for most substances, even at high fields, but is relatively large (a few percent) for strongly magnetic substances. The resistance of nickel increases about 2 percent, and that of iron about 0.3 percent, when it passes from demagnetized to the saturated state under magnetişc field.

A magnetoresistance measurement is usually done on a rod or wire specimen with the measuring current i and the applied field H both parallel (longitudinal magnetoresistance) to the rod axis or, current i and the applied field H both perpendicular (transverse magnetoresistance) to the rod axis. Then, in most ferromagnetics, the observed effect is an increase in R of any domain as the angle θ between the current i and M_s vector of that domain decreases. The physical origion of the magnetoresistance effect lies in spin-orbit coupling: as M_s rotates, the electron cloud about each nucleus deforms slightly [74,75].

Magnetoresistance arising from a nanoscale magnetic structure was first discovered by Lark-Horovitz and Johnson in ferromagnetic and antiferromaqgnetic materials [102]. In metals, the magnetoresistance is a second-order effect, which arises from the deviation of the conduction electrons from free electron behavior and from the existence of very small range in electron velocities [103]. The magnetoresistance measurements allowed us to determine the GMR effect and the magnetic field sensitivity of GMR [104]. The GMR effect results from two factors: (a) spin dependence of the electronic band structure of a defect-free system, and (b) spin dependence of scattering potential [74].

It is generally refered as giant magnetoresistance (GMR) due to the large and isotropic resistance change as compared to the anisotropic magnetoresistance (AMR) of bulk ferromagnetic materials. The large change in resistance under magnetic field gives great potential for technological applications [102,104].

3.8 Experimental Apparatus and Electrodeposition Technique

3.8.1 Electrodeposition Method

3.8.1.1 Introduction

In general, the main concerns in the practical application of this technique can be summarized as follows;

(i)- Chemical and electrochemical stability are required for the solvent and cathode electrode which is used as substrate. Depending on the final product, aqueous or nonaqueous solutions are used as an electrolyte and the deposition quality is strongly affected by the purity of solution.

(ii)- The characteristics of substrates such as stability, surface conditions and morphology are the determining factors for initial and subsequent deposition. The substrate may vary from being a liquid metal to a single crystal.

(iii)- The electrical resistivity of deposited layers should be low enough to allow the current density to remain in the optimum range, and any existing surface oxide must be removed by reaction with the solvent.

(iv)- Although decomposition can be achieved under constant current, constant potential or by other means involving pulsed current or voltage, the current density level must remain within the pre-defined values, depending on the materials involved.

(v)- Doping during the elecrodeposition and post-deposition treatments is often required to improve the characteristics of films.

3.8.1.2 Experimental set-up of Electrodeposition system

The electrodeposition system is simple, consisting of an anode and a cathode which are immersed in a suitable electrolyte. Metal or semi-conductor material can be deposited on the cathode. A schematic block diagram of an experimental apparatus used for electrodeposition is shown in Figure 3.10.

According to the Faraday's rule, the amount of deposit is proportional to the total amount of charge which passes during the depositing. This rule is employed to determine film thickness as in the following expression;

$$\frac{G}{A} = jtE\alpha(g/cm^2) \tag{3-13}$$

Where G/A is the weight of deposite per unit area, J is current density, t is time and α is the current efficiency which is the ratio of the experimental to theoretical weight deposited and E is electric field. It can generally be expected to be between unity and 0.5. This equation can be written in a slightly different form to give the rate of the deposition. If a thickness L is deposited in time t, then the rate of deposition L/t is given by

$$\frac{L}{t} = \frac{jE\alpha}{\rho}(cm/\sec) \tag{3-14}$$

where ρ is the film density.

The efficiency of the electrodeposition process can also be defined as the ratio of the current used for the reduction of the ions for the intended deposit to the total current passed through the cell. From thermodynamics it follows that only copper and more noble metals can be expected to deposit with 100% efficiency from a water-based electrolyte. For all other elements, at least a part of the current will be consumed in the formation of hydrogen gas.

Usually one wants to reduce this effect as much as possible, to increase the deposition efficiency and hence the deposition rate. The gas bubbles formed on the sample surface also hinder further deposition. Most practical electroplating systems operate at an efficiency of 90% or higher although in some cases it can be as low as 20%. The deposition rate in electroplating can be determined from the Faraday's law as expressed in Eq.(3-13).

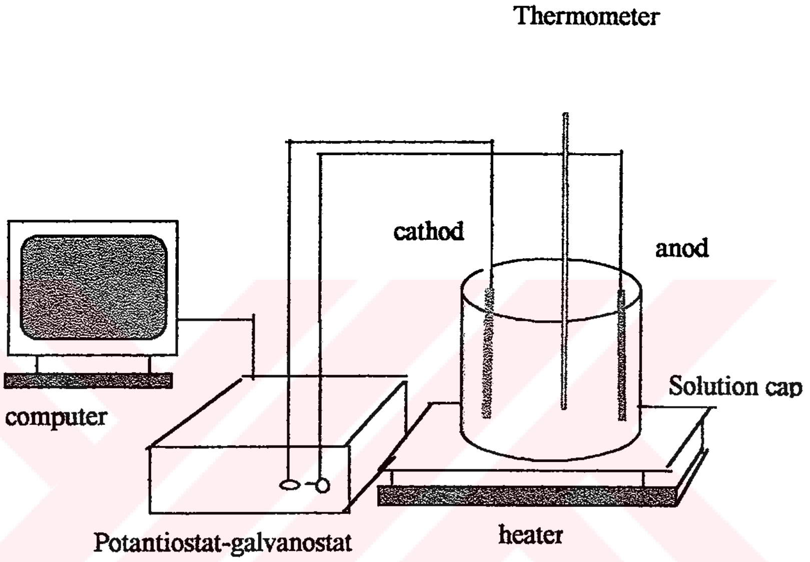

Figure 3.10 Schematic diagram of the electrodeposition system

Our system is controlled by a computer during the electrodeposition process to provide a constant potential or a constant current for a certain period of time. A magnetic stirrer heater is used to stir and control the temperature of chemical solution .

3.8.2 Deposition of Conducting $Ni_xFe_{(1-x)}$ Alloy Films onto a Copper Substrate by Electrodeposition Technique

3.8.2.1 Preparation of Copper Substrate for Electrodeposition

Before the deposition of $Ni_xFe_{(1-x)}$ film layer onto a copper substrate some cleaning processes were applied as follows:

1- Copper plates were cut into 1x2 cm in dimension.

2- The copper plates were mechanically polished with a zero number emery paper.

3- The mechanically polished surface of the copper plates were washed a few times with distilled water.

4- Then, the copper plates were electrochemically polished in a phosforic acid solution until a mirror like appearance was obtained.

5- Finally, the surface of the copper plates were rinsed in distilled water and dried with a dry paper.

At the end of all these processes, the copper substrate is ready for the application of electrodeposition of $Ni_xFe_{(1-x)}$ film.

3.8.2.2 Deposition of Conducting $Ni_xFe_{(1-x)}$ Alloy Films onto a Copper Substrate

To produce $Ni_xFe_{(1-x)}$ alloy film samples onto a copper substrate, a cleaned copper surface was prepared as explained above. A 50 ml solution of Ni and Fe sulfate salts was used. The Ni : Fe ratio in the electrolyte was initially 25:1 and then the ratio was changed gradually towards 1:1 to produce a set of nine NiFe alloy films with different compositions. The bath composition was consisted $NiSO_4.6H_2O$ (3.35-131.5 g/l), $FeSO_4.7H_2O$ (5.56 g/l) and H_3BO_3 (24.72 g/l). The pH value of the solution was adjusted to 3 by the addition of 1 M H_2SO_4 solution. The bath solution was freshly prepared each time before deposition. Two electrodes were used as an anode (platin electrode) and as a cathode (copper electrode, 2 cm^2 in size) and immersed into the chemical solution as seen in Figure 3.10. During the deposition process, the temperature of the solution was maintained at room temperature and no stirring was applied. The depositions were carried out by using a computer controlled potantiostat-galvanostat device. NiFe alloy film samples were cathodically deposited onto the copper substrate. During the deposition process a current density of 16 mA/cm^2 was applied. The desired current was immediatly applied upon the insertion of the electrode into the chemical solution and the deposition was maintained for 15 min. The range of pH is important because the current density passing through the solvent, closely affects film quality, and prohibition of the hydrogen gas etc. During the deposition process positevely charged Ni^{+2} and Fe^{+2} ions are accelerated under the influence of the applied potential towards the cathodic electrode (copper working electrode).

$$Ni^{++} + 2e \rightarrow Ni \ , \quad Fe^{++} + 2e \rightarrow Fe \qquad (2.15)$$

When the ions reach to the cathodic electrode, they bond at the surface of by taking electrons from the cathodic electrode, so that a metallic film of NiFe alloy is formed on the copper substrate. And also during this process, an amount of hydrogen gas was yielded therefore at least a part of the applied current was consumed in this formation.

After the succesful deposition process, the NiFe films were stripped off from the surface of the copper plates using a cromic sulfuric acid solution which solves the copper substrate while the NiFe alloy films remains unaffected. To strip off the NiFe films from the Cu substrate and to protect it from dissolving process it was covered with the nail polisher while the Cu substrate side was exposed to the cromic sulfuric acid solution. A set of carbon rods were used as cathode in this process as seen in Figure 3.11.

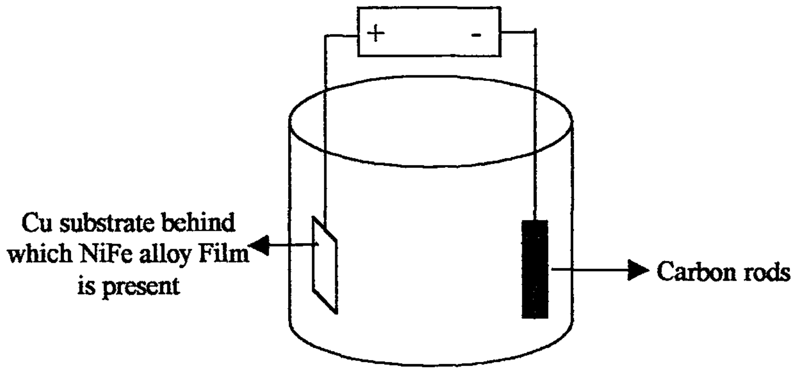

Figure 3.11 Schematic diagram of substrate stripping system

MEASUREMENTS AND RESULTS

3.9 Measurement Techniques and Results

3.9.1 Determination of Compositions and Thickness of Ni_xFe_{1-x} Alloy Films

To determine Ni and Fe contents in the NiFe alloy films, Atomic Absorption Spectrophotometer was used. For this process, a 10 ml reference solution was prepared for each element of Ni and Fe by using pure Ni and Fe and then each NiFe films was solved one by one in a 10 ml chemical solution of 2.5 ml %35 nitric acid and 7.5 ml distilled water. These reference and NiFe samples were examined by the Atomic Absorption method to determine the Ni and Fe concentrations. According to the Atomic Absorption results, the compositions of the NiFe film samples were given in Table 3.1.

To determine the thickness of the film samples, the density, mass and volume relation was used. This relation is defined as

$$d_{(NiFe)} = \frac{m}{V} \tag{3-16}$$

where d is the density of the NiFe alloy films, m is the mass of solid material and V is the volume of the solid material. V=A*t ; where t is the thickness of film and A is the area of film sample and the densities of NiFe alloy film samples were calculated by using the following equation

$$d_{Ni_xFe_{(1-x)}} = d_{Ni}C_{Ni}(\%) + d_{Fe}C_{Fe}(\%) \tag{3-17}$$

where d_{Ni} and d_{Fe} are densities of pure Ni and Fe, respectively, $d_{Ni} = 8.92$ gr/cm^3 and $d_{Fe}= 7.87$ gr/cm^3, and C is the concentrations of Ni and Fe in the samples determined by using Atomic Absorption Spectrometer results. The calculated thickness of the alloy film samples are given in Table 3.1

Table 3.1 The alloy film thickness and the concentration of the Ni and Fe in the NiFe film samples

Sample	Thickness(μm)	%Ni	%Fe
$Ni_{0.22}Fe_{0.78}$	3.75	22	78
$Ni_{0.27}Fe_{0.73}$	3.23	27	73
$Ni_{0.39}Fe_{0.61}$	2.45	39	61
$Ni_{0.46}Fe_{0.54}$	2.32	46	54
$Ni_{0.48}Fe_{0.52}$	3.12	48	52
$Ni_{0.51}Fe_{0.49}$	2.32	51	49
$Ni_{0.52}Fe_{0.48}$	2.29	52	48
$Ni_{0.62}Fe_{0.38}$	3.2	62	38
$Ni_{0.64}Fe_{0.36}$	2.73	64	36

3.9.2 The Crystal Structure of the Film Samples

In this study, the crystal structure of NiFe conducting film, grown by using electrodeposition technique were determined using a Philips X-Ray Powder diffractometer with monochromated high intensity CuKα radiation (λ=1.5405 A^0). Examples of the diffraction spectra of some NiFe alloy samples are given in Figure 3.12. As it can be seen from the figure that the peak at 2θ= 44 - 44.5 represents NiFe alloy while the other peak may belong to either Ni_3Fe or NiO. Because the latter peak appears in every spectrum of NiFe samples used in this study, it is more probable that it may represent Ni_3Fe in our sample. A diffraction peak of Ni_3Fe in electrodeposited Au/NiFe/Cu system [105] and in sputtered NiFeCo-Ag system [106] was also reported. It is also observed that both peaks shift to lower angles with increasing amount of Ni content in sample. The NiFe peak has a broad line width which may indicate that it may be contributed by a distribution of different Ni and Fe regions. Assuming, therefore, the NiFe diffraction peak is contributed by the distribution of atoms of Ni and Fe from both Ni rich and Fe rich regions in sample, the (111) and (110) planes may contribute to form the broad diffraction peak. The lattice constant of our samples may therefore be calculated using the average of (111) and (110) planes.

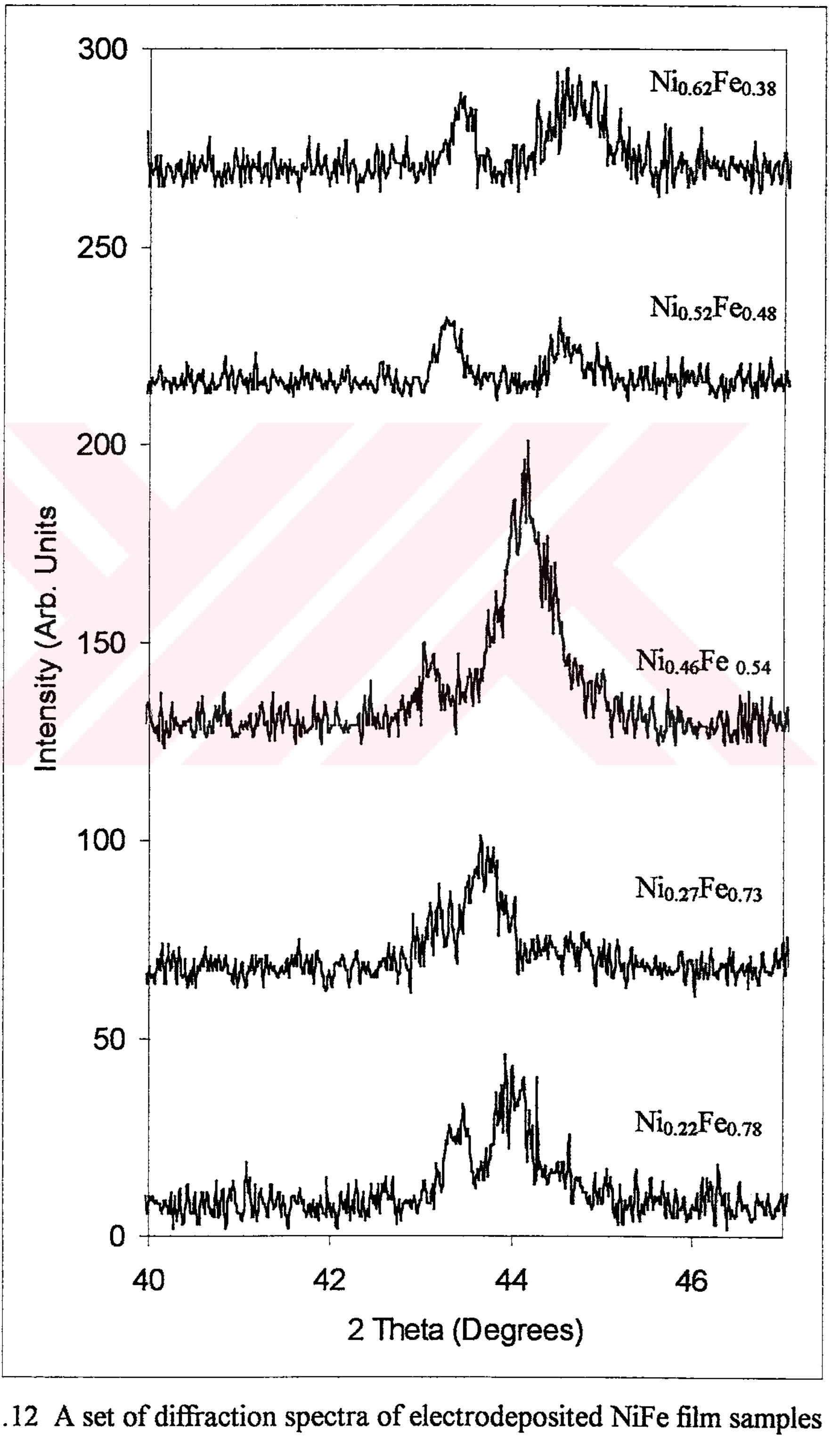

Figure 3.12 A set of diffraction spectra of electrodeposited NiFe film samples

The percentage concentrations of Ni and Fe were used to calculate the average of (111) and (110) planes and the lattice constant (***a***) was calculated using $a^2=\lambda^2(h^2+k^2+l^2)/4\sin^2\theta$ where the θ values from the diffraction spectra were used. λ is the wavelength of copper K_α x-ray. Assuming the numbers of (111) and (110) diffraction planes are proportional to the percentage amount of Ni and Fe in samples, respectively, the contributions to diffraction peak from the average values of diffraction planes (111) and (110) were calculated multiplying $(h^2+k^2+l^2)=3$ by the Ni percentage and $(h^2+k^2+l^2)=2$ by the Fe percentage and summing them up. The variation of the lattice constant ***a*** (calculated following the procedure above) with the Ni percentage in the samples is shown in Figure 3.13. The lattice constant increases with increasing Ni percentage as the diffraction angle for NiFe peaks shifts higher values with increasing Ni percentage in the samples. This may be understood by considering that the increase in the Ni percentage in samples does not soley contribute to form FCC structures but also contribute to form FCC rich and BCC rich regions with Ni and Fe atoms in our samples.

Table 3.2 Variation of the lattice constant of $Ni_xFe_{(1-x)}$ films with Ni percentage

2θ	**Ni(%)**	**Fe(%)**	**a(A^0)weighted**
44	22	78	3,0633
43,64	27	73	3,1226
44,4	39	61	3,1492
44,16	46	54	3,2161
44,45	48	52	3,2033
44,6	51	49	3,2155
44,63	52	48	3,2154
44,7	62	38	3,2814

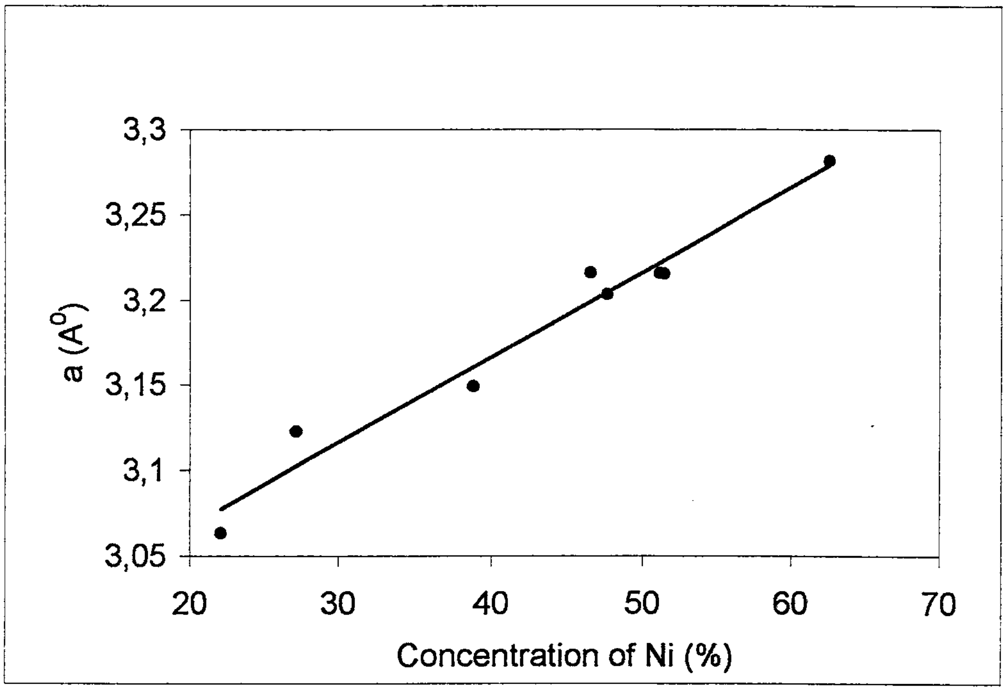

Figure 3.13 Variation of lattice constant of $Ni_xFe_{(1-x)}$ films with Ni percentage

3.9.3 Scanning Electron Microscope (SEM) Measurements

The surface images of two NiFe alloy films which have different concentrations ($Ni_{0.22}Fe_{0.78}$ and $Ni_{0.64}Fe_{0.36}$) were taken by Jeol-6400 model SEM. As seen from Figure 3.14 and Figure 3.15 both images show granular structures. The surfaces of both films are very smooth, although the surface of $Ni_{0.64}Fe_{0.36}$ film looks smoother than the $Ni_{0.22}Fe_{0.78}$ film. This may be expected because more Ni content causes better alloying effect in alloy samples. The density of the grains in $Ni_{0.22}Fe_{0.78}$ is therefore greater than $Ni_{0.64}Fe_{0.36}$.

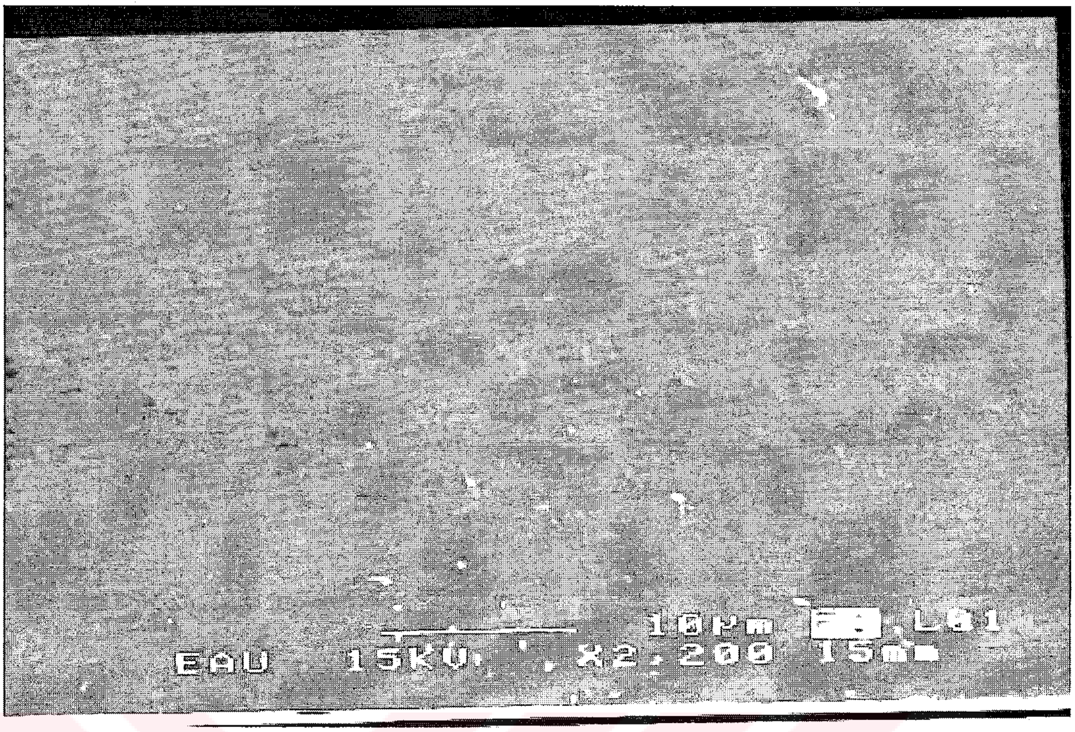

Figure 3.14 SEM-image of electrodeposited $Ni_{0.22}Fe_{0.78}$ alloy film

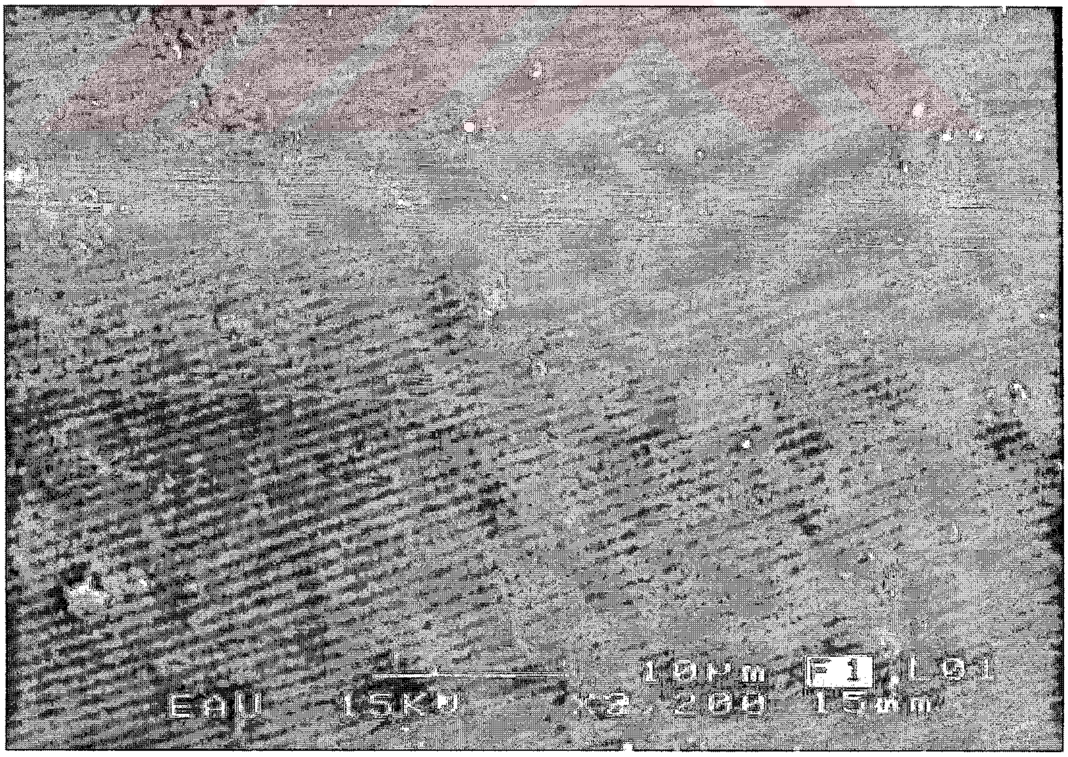

Figure 3.15 SEM-image of electrodeposited $Ni_{0.64}Fe_{0.36}$ alloy film

3.9.4 Investigation of the Magnetic Properties of NiFe magnetic films

Magnetoresistance measurements

To investigate the magnetoresistive effects in NiFe ferromagnetic film samples, the resistance values were measured at room temperature. For this purpose; the DC resistivity of NiFe ferromagnetic films, with and without the application of magnetic field, was measured using a home made electromagnet of range 0- 2000mT as shown in Figure 3.17.

The Van der Pauw method for the measurement of the resistance of NiFe films was applied. A four-point contact was prepared on film samples. All of the contacts points were placed in a square (4x4 mm). For better electrical contacts silver paste was used. The samples were inserted in specially desinged sample holder for transverse and longitudinal measurements. A constant DC current of 10 mA was passed along the film surface. The potential difference between on the film surface with and without the application of magnetic field was measured on a digital nanovoltmeter (Prema 5017 model).

The magnetoresistance measurements of NiFe ferromagnetic film samples were done for three types of configurations as seen in Figure 3.16: (a) with a magnetic field applied parallel to the current direction (I) in the film plane (θ=0) (longitudinal geometry, Fig.3.16(a)) , (b) the magnetic field perpendicular to the current direction in the film plane (transverse geometry, Fig.3.16(b)), (c) with the magnetic field applied perpendicular to the film plane with the current either as in the longitudinal or perpendicular geometries, (Fig.3.16(c)). This geometry (c) is named as either longitudinal-perpendicular geometry or transverse-perpendicular geometry depending on the current direction. The graphs for longitudinal magnetoresistance measurements are shown in Figure 3.18 for nine samples which were gained from the measured data.

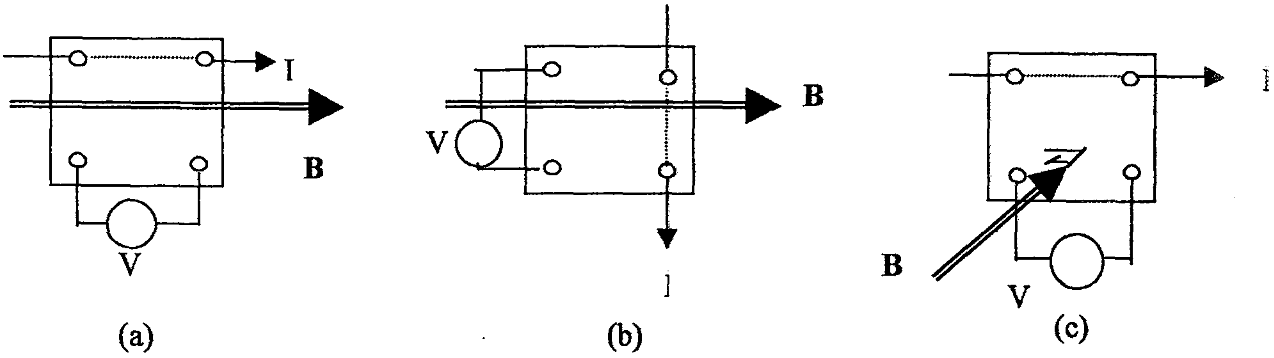

Figure 3.16 A laboratory set-up for magnetoresistance measurements

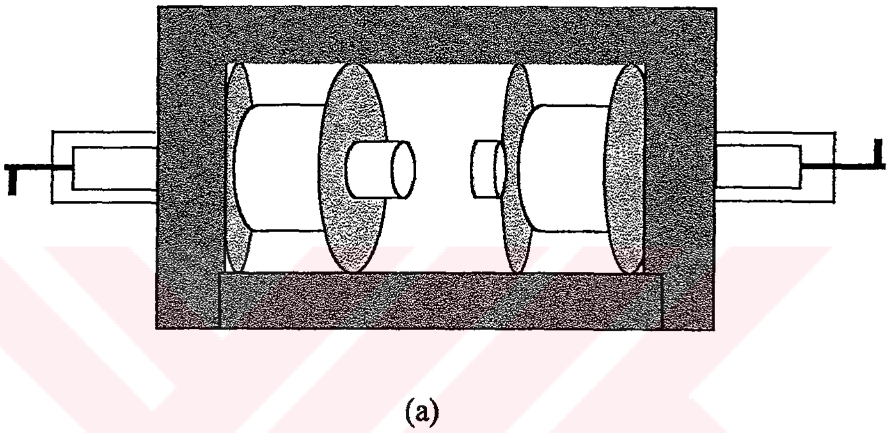

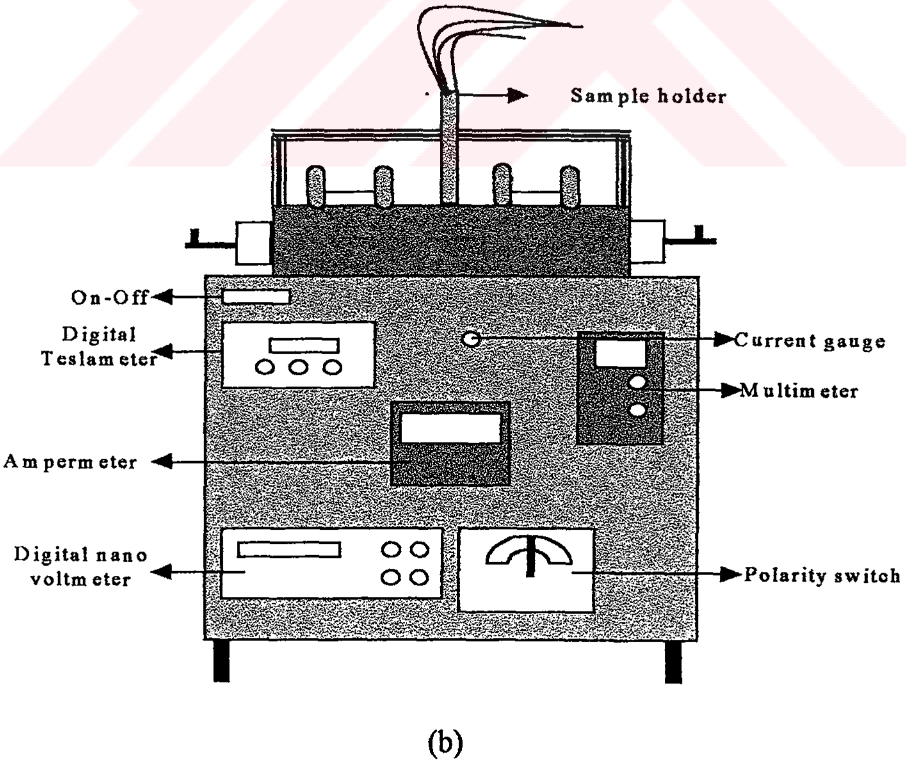

Figure 3.17 Illustration of the home made electromagnet (a) top and (b) front view

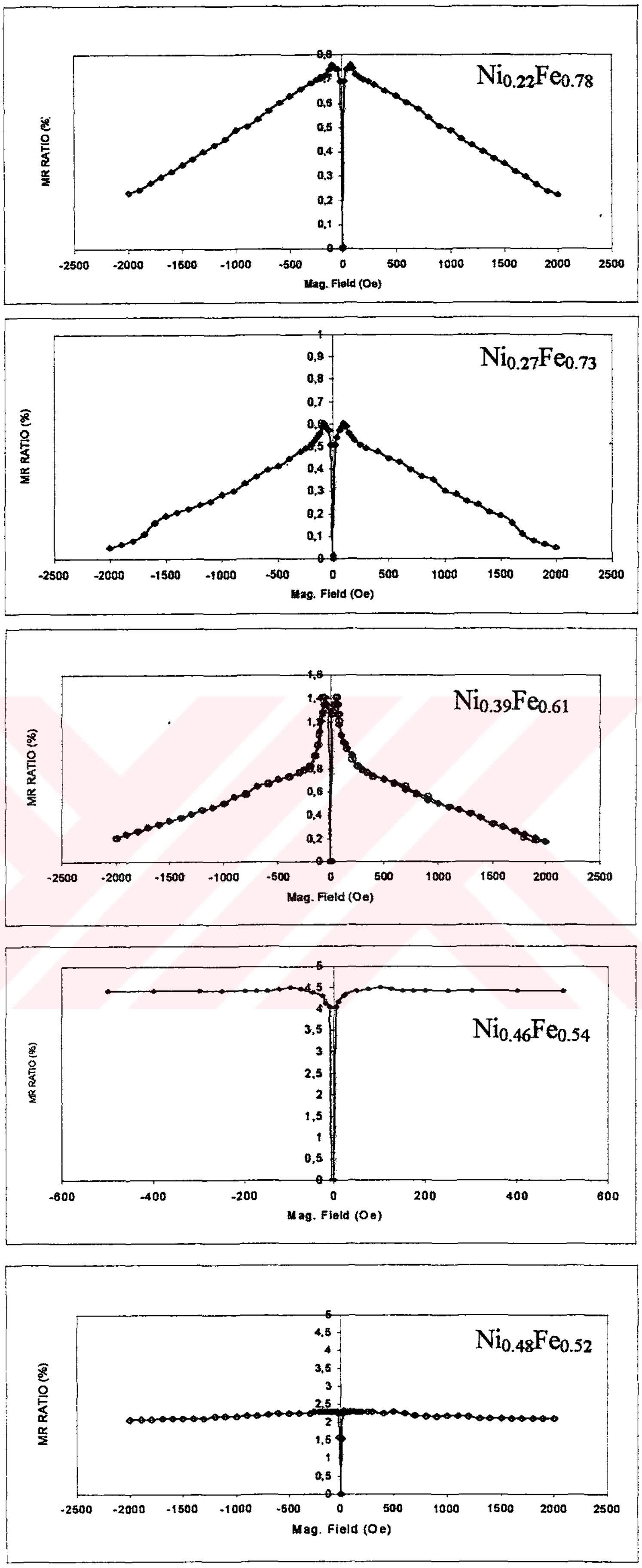

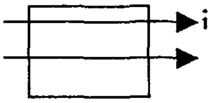

Figure 3.18 Continues on the next page

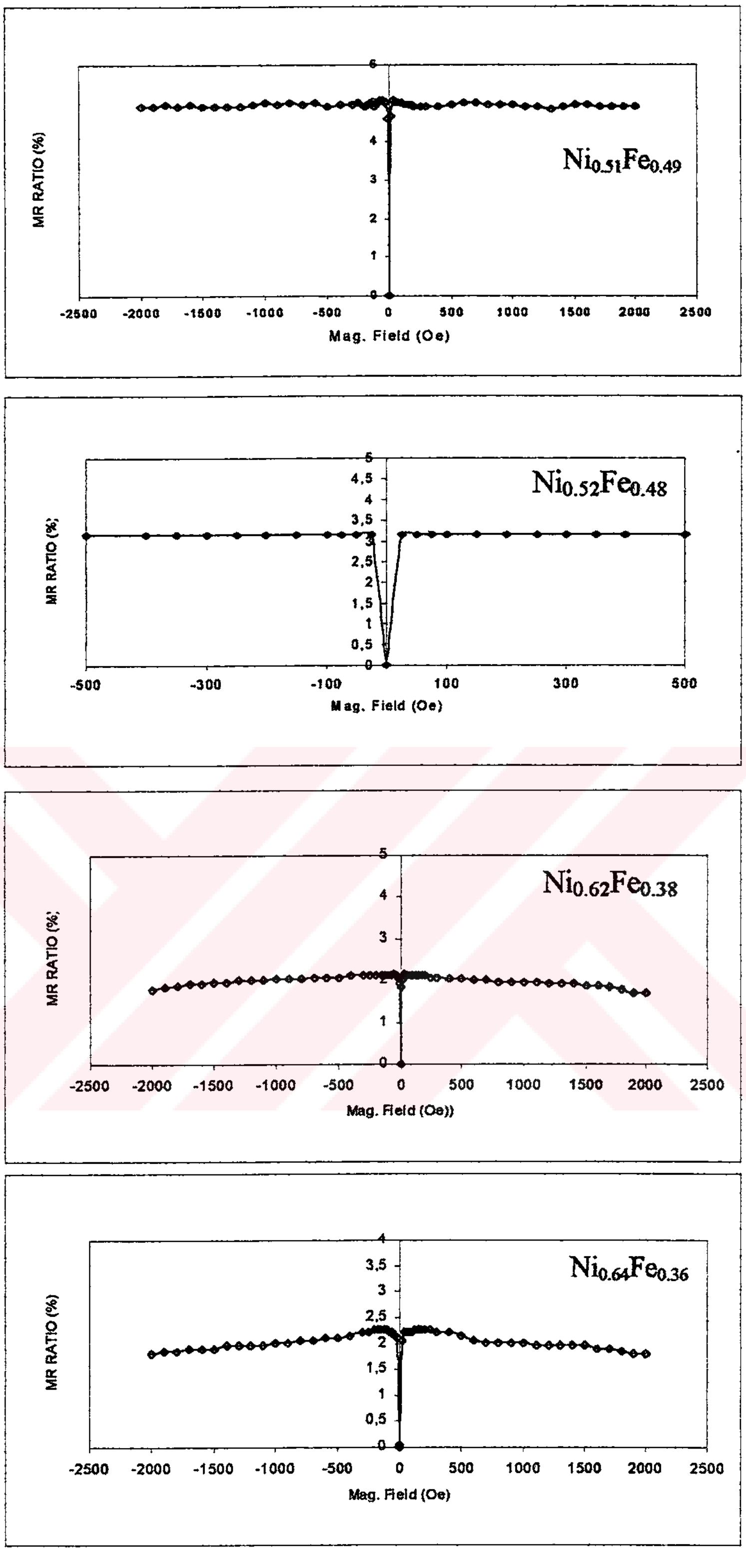

Figure 3.18 Longitudinal magnetoresistance curves of NiFe samples of various composition where current and magnetic field directions are parallel to each other in the plane.

The magnetoresistance (MR) effect was studied for all the samples in the longitudinal geometry. Figure 3.18 shows the longitudinal magnetoresistance curves of the NiFe samples of various composition.

In all the samples the magnetoresistance value jumps to a positive value for a very small magnetic field increase (>20 Oe). The maximum positive magnetoresistance value is observed as 4.5% in the samples of $x=0.46$ and $x=0.51$ while the lowest value is 0.6% - 0.8% in samples of $x=0.22$ and $x=0.27$. For the Ni concentration $x\leq0.39$, the positive magnetoresistance value is under 1.5%, while for the Ni concentration $x\geq0.46$, the positive magnetoresistance value is greater than 2%.

And also the positive magnetoresistance value decrease with increasing magnetic field as seen in the samples with $x=0.22$, 0.27 and 0.39. This indicates that in these samples there is also a negative component of magnetoresistance effect which can be detected above a certain magnetic strength (> 20 Oe). No saturation was obtained even in the magnetic field of 22 kOe in the three samples with $x=0.22$, 0.27 and 0.39, but in the samples with $x\geq0.46$ the saturation was obtained for a very small magnetic field increase (> 20 Oe). The samples with $x\geq0.39$ have higher magnetoresistance values between 1.5% and 4.5% than those with $x<0.39$ between 0.6% and 0.8%.

These results show that the samples with $x\geq0.39$ have a pure positive magnetoresistance properties while the others show a mixture of positive and negative magnetoresistance effect. No pure negative magnetoresistance component was detected in these samples in the longitudinal geometry.

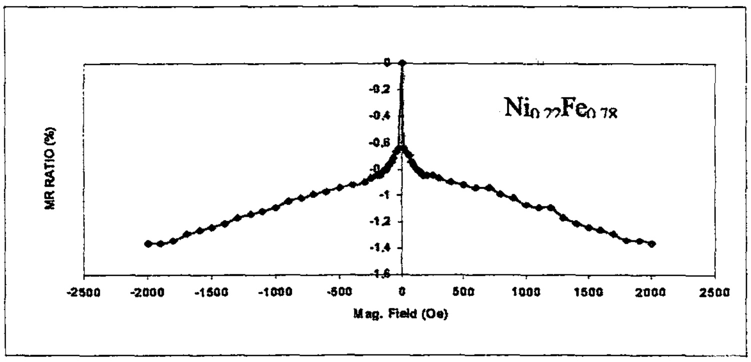

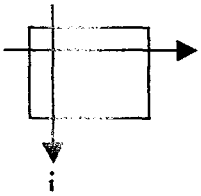

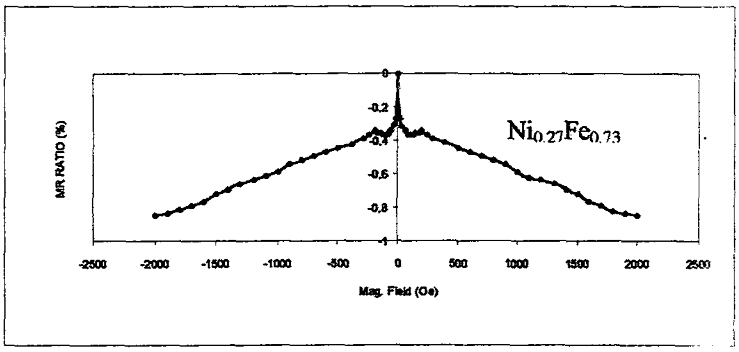

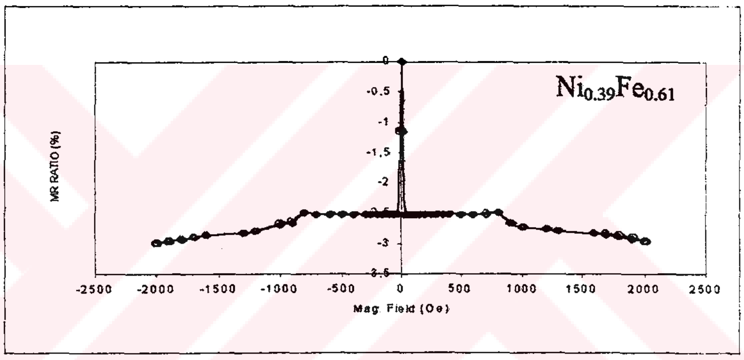

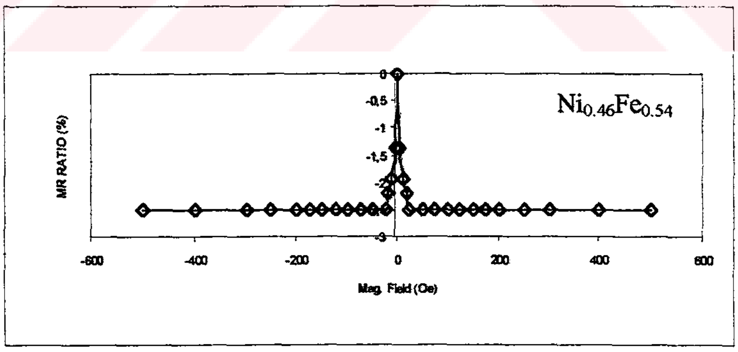

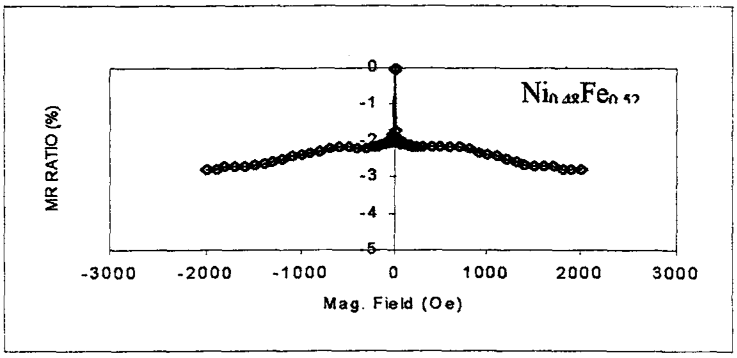

Figure 3.19 Continues on the next page

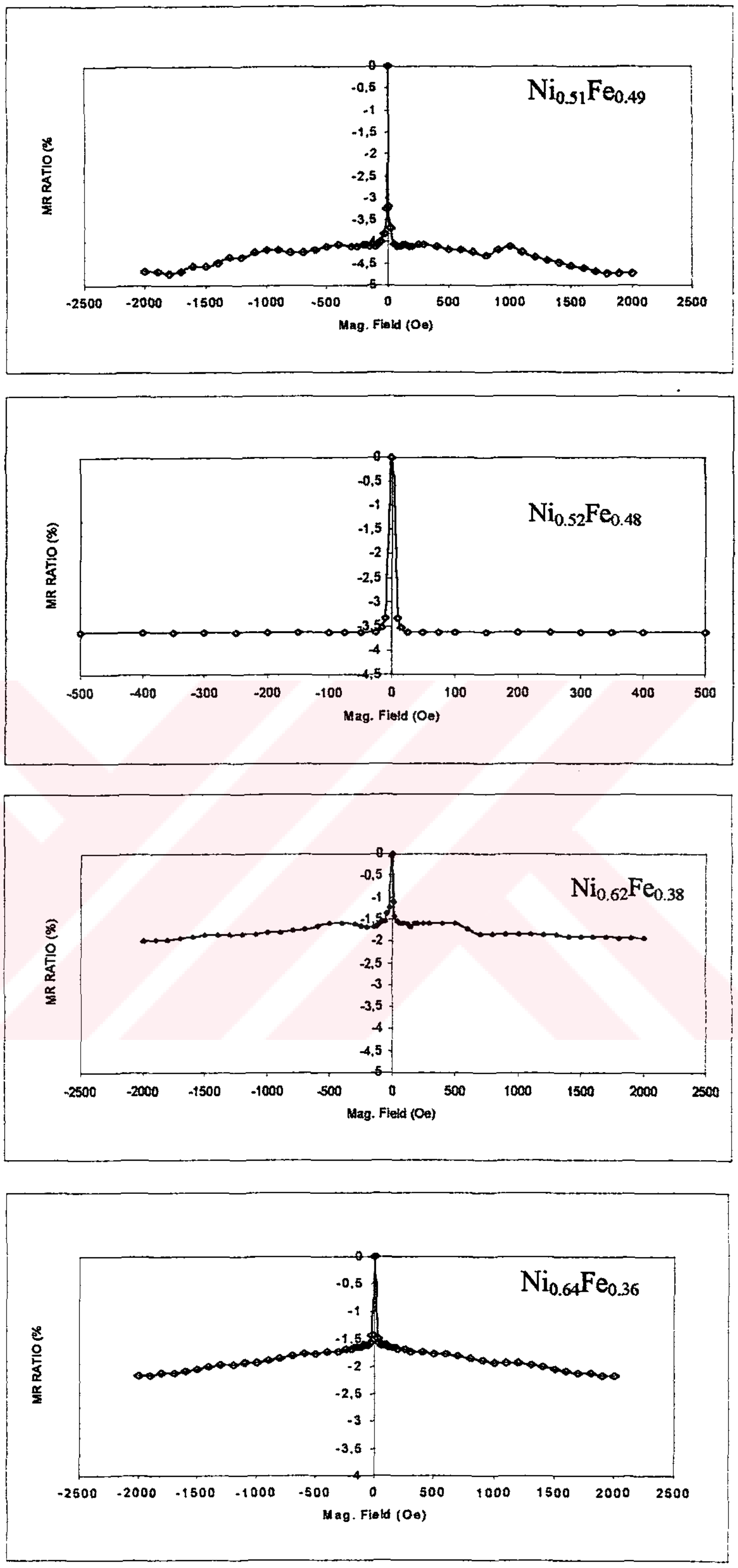

Figure 3.19 Transverse magnetoresistance curves of NiFe samples where current and magnetic field directions are perpendicular to each other in the plane

In the transverse configuration both current and magnetic field were applied parallel to the film plane although the direction of magnetic field was kept the same as in the longitudinal geometry while the direction of current was oriented perpendicular to magnetic field.

The transverse magnetoresistance curves of the NiFe samples can be seen in Figure 3.19. In all the samples a negative magnetoresistance effect is detected while only in the samples with $x \leq 0.39$ the positive component of magnetoresistance effect is seen to be overlapped on the negative one above ~20 Oe. In the other samples, the negative component is dominant and it saturates just above >20 Oe.

It is found that in the measurement of the transverse geometry the magnitude of magnetoresistance ratio (both positive and negative) is also composition dependent so that it is greater, which is purely negative between 1.5% and 4.5% in the samples with the Ni percentage concentration $x > 0.39$ than those between 0.8% and 1.4% in the samples with $x \leq 0.39$ which also indicates a positive component above 20 Oe.

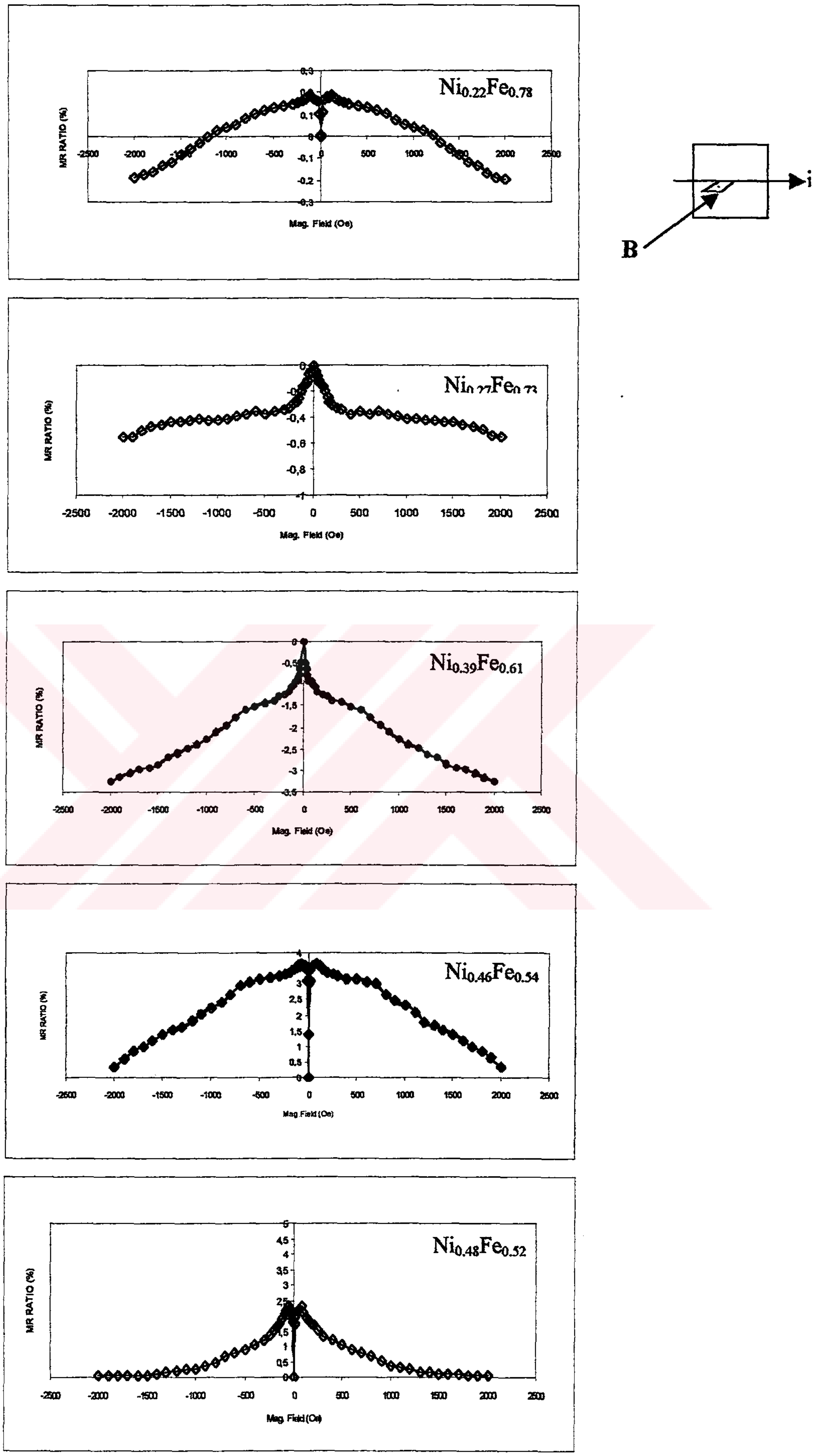

Figure 3.20 Continues on the next page

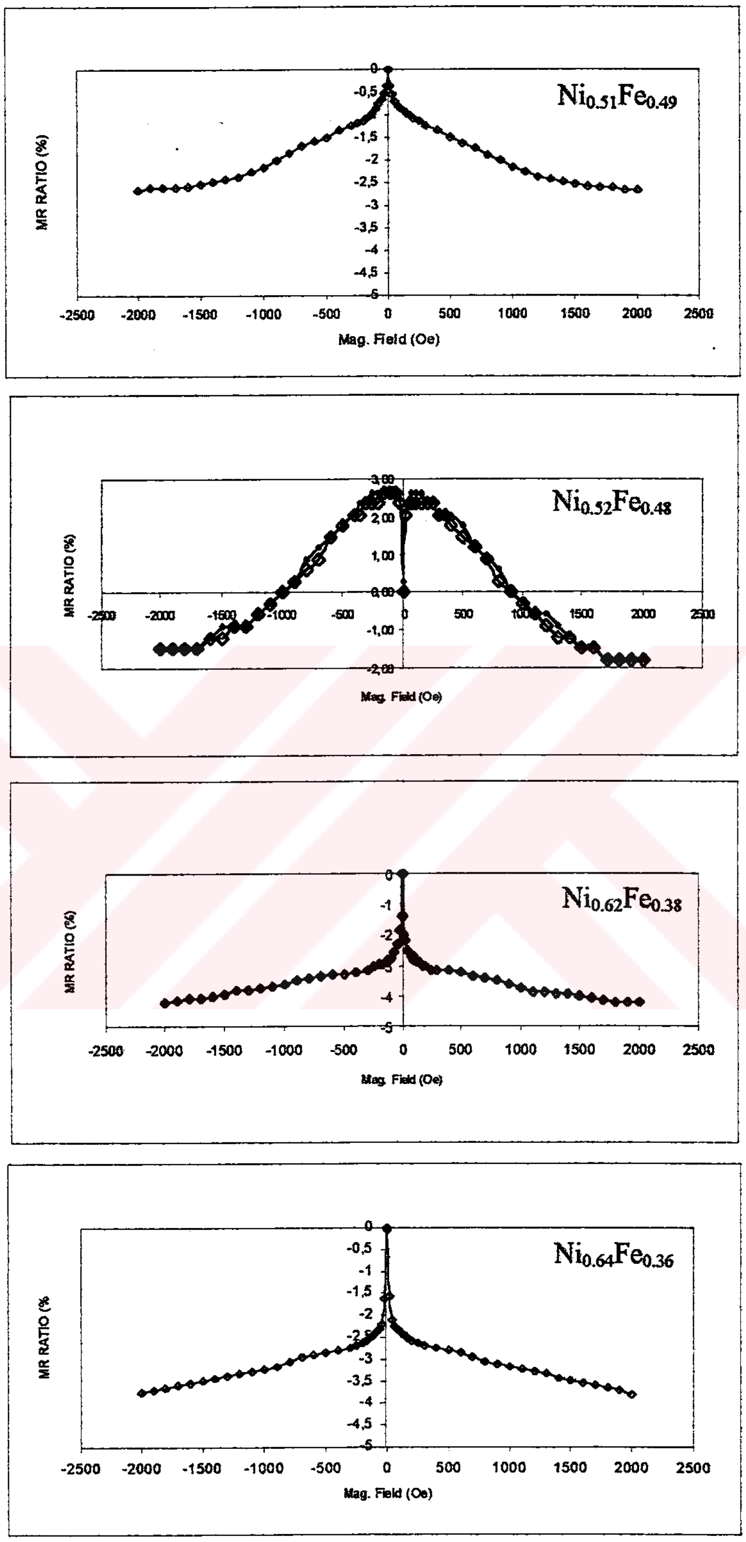

Figure 3.20 The magnetoresistance curves taken in longitudinal-perpendicular geometry where current is kept the same as in the longitudinal geometry while magnetic field is applied perpendicular to film plane

The third cofiguration is either longitudinal or longitudinal-perpendicular geometry. The directions of currents in both the longitudinal and transverse-perpendicular geometries were kept the same as how they were in their geometries while the direction of the magnetic fields varied from parallel direction to the perpendicular direction to the film plane.

In this configuration as seen in Figure 3.20 a significant demagnetization effect occurs while it is of negligible importance in the longitudinal and transverse geometries. The magnetic field inside the film is different from the applied external field so that a demagnetization correction must be done to find the actual magnetic field within films. This is done using the expression of B(local)= B(applied)-μ_0M where B(local), B(applied) and M are local field within the film,externally applied field and the magnetization in the direction of applied field respectively [107].

However for the sake of clarity, the magnetoresistance curves were introduced as not a function of local field but as a function of applied field. The magnetoresistance measurements were also done in these geometries for all the nine samples. The magnetoresistance curves taken for both current directions with the magnetic field perpendicular to the film plane (at 90^0) are shown in Figure 3.18 and 3.19 .

As it can be seen from Figure 3.20 that the positive and negative components of magnetoresistance effect in the samples with x=0.22, 0.46, 0.48 and 0.52 are again observed to be in competition in this geometry (longitudinal-perpendicular geometry) The samples with x= 0.27, 0.39, 0.51, 0.61 and 0.64 show the dominancy of negative magnetoresistance ratio with a varying maximum magnitudes between ~0.5% and ~4.5% with a tailing section above the magnetic field of 300 Oe, repectively. This tailing section may be an indication of the presence of the positive component in the dominancy of the negative one.

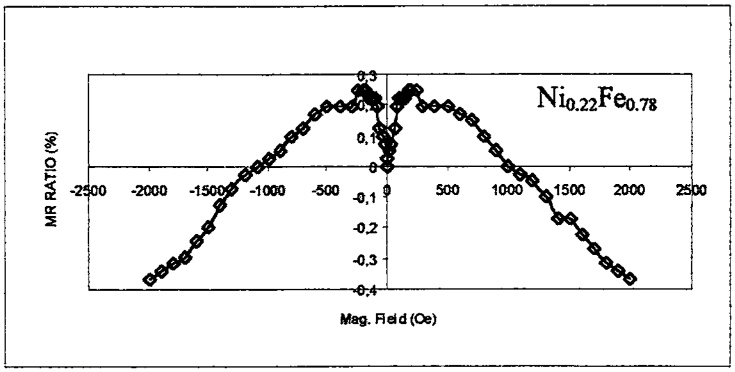

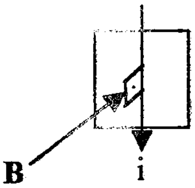

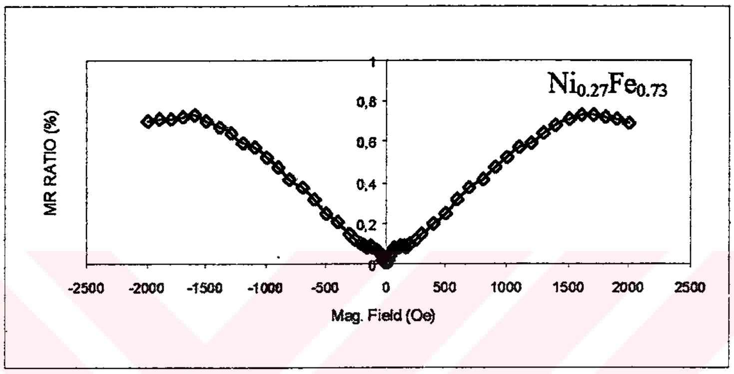

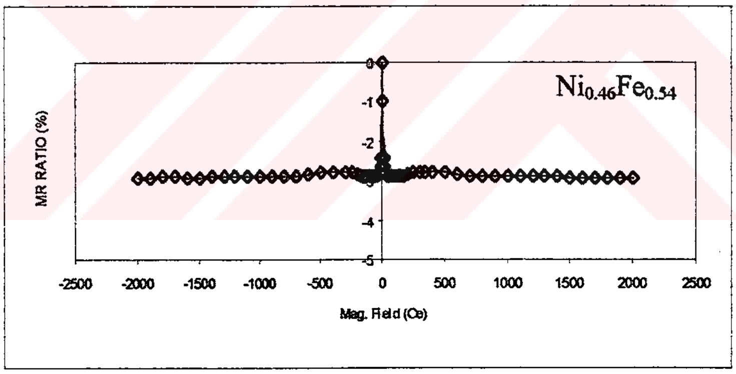

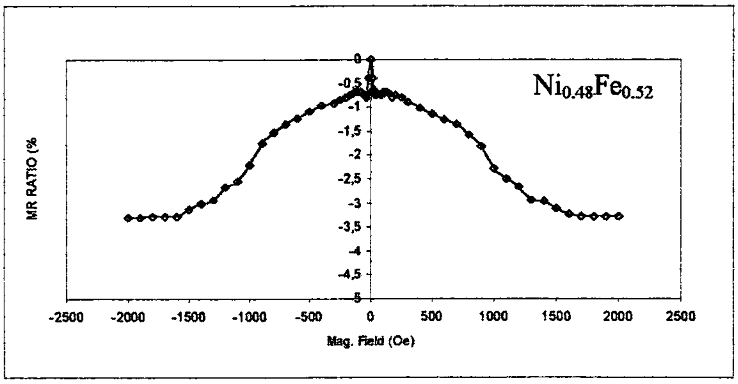

Figure 3.21 continues on the next page

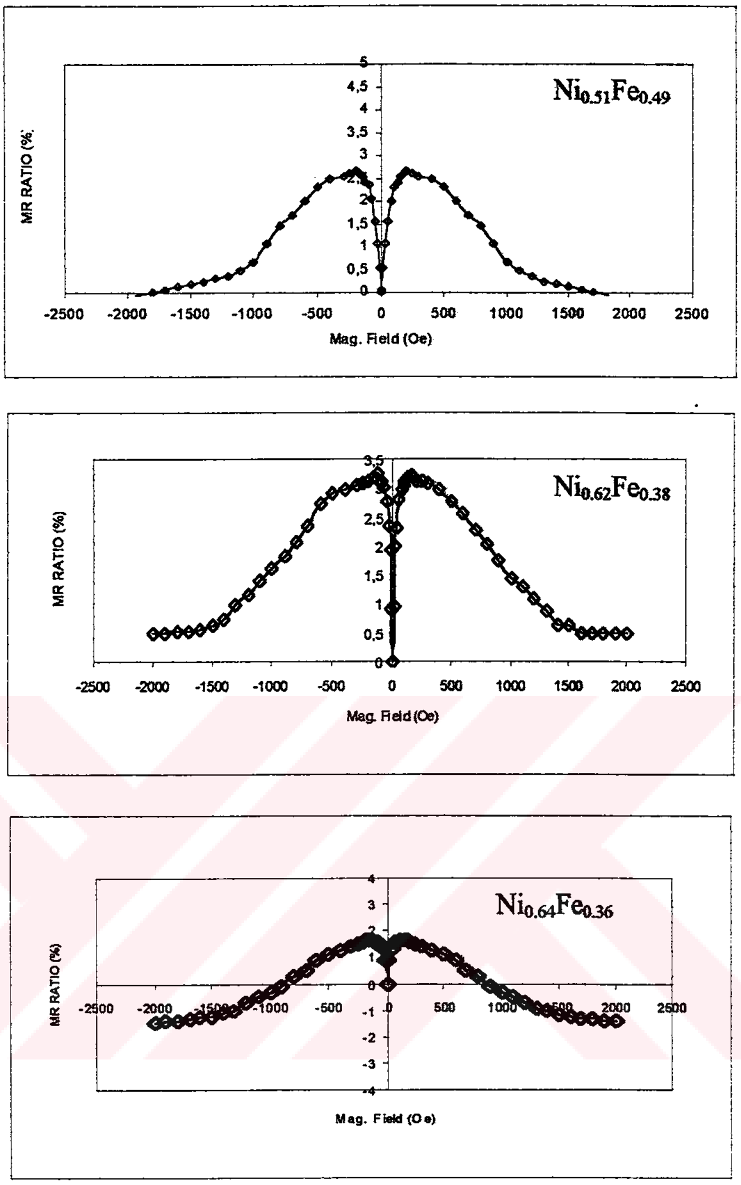

Figure 3.21 The magnetoresistance curves taken in transverse-perpendicular geometry where current is kept the same as in the transverse geometry while magnetic field is applied perpendicular to film plane

In the transverse-perpendicular geometry, a significant demagnetization also occurs in the samples but the magnetoresistance change is also expressed as a function of the applied field for the sake of clarity in this geometry.

The curves of the magnetoresistance ratio for this geometry shown in Figure 3.21 that the positive and negative components of magnetoresistance effect are present in the samples with x=0.22, 0.51, 0.62 and 0.64.

The magnetoresistance value jumps to a positive value for a very small magnetic field increase (>100 Oe) in the samples with x=0.22, 0.27, 0.51, 0.62 and 0.64 and also the positive magnetoresistance decrease with increasing magnetic field. There is a pure positive magnetoresistance effect in the sample with x=0.27 while the negative magnetoresistance dominancy was detected in the samples with x=0.46 and 0.48.

The maximum negative magnetoresistance value is observed as 3% in the sample with x= 0.46, the negative magnetoresistance becomes saturated above >20 Oe in this sample. On the other hand, sample with x=0.48 also shows a negative magnetoresistance ratio with a maximum magnitude of 3.5% with a tailing section above the magnetic field of 100 Oe.

The other samples as it is mentioned above shows a mixture of positive and negative magnetoresistance effect. The maximum value of the positive magnetoresistance ratio peak is smaller than 1% in the samples with x=0.22 and 0.27 and greater than 2% in samples with x=0.51, 0.62 and 0.64.

3.9.5 Magnetoresistance Measurements with Angular Variation

The magnetoresistance measurements of NiFe alloy films were also done as a function of angular variation from 0^0 to 90^0 at room temperature for the two geometries: (i) longitudinal-perpendicular, (ii) transverse-perpendicular geometries. The angular variation of magnetoresistance curves were given in the following Figure 3.22.

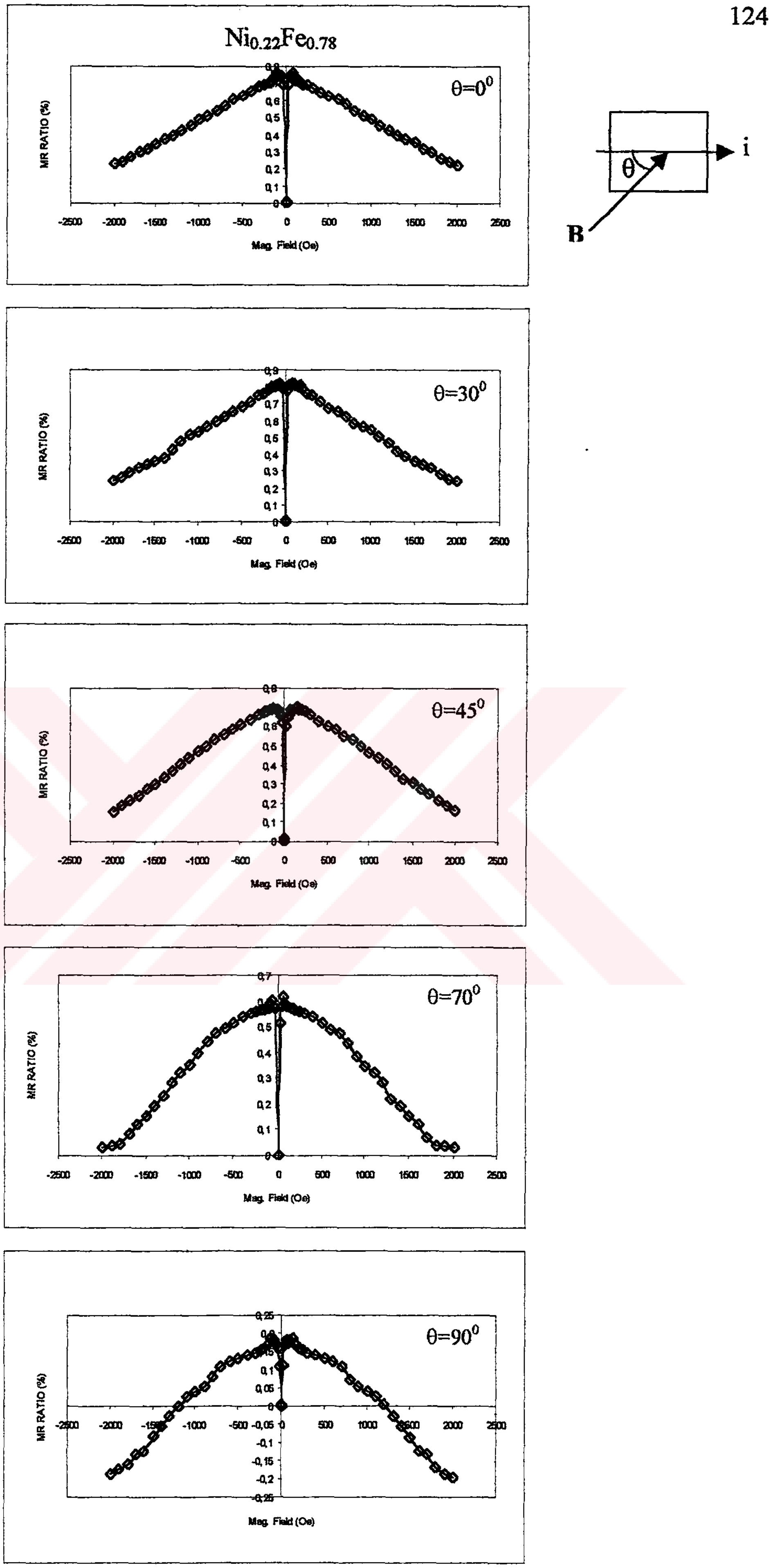

Figure 3.22 continues on the next page

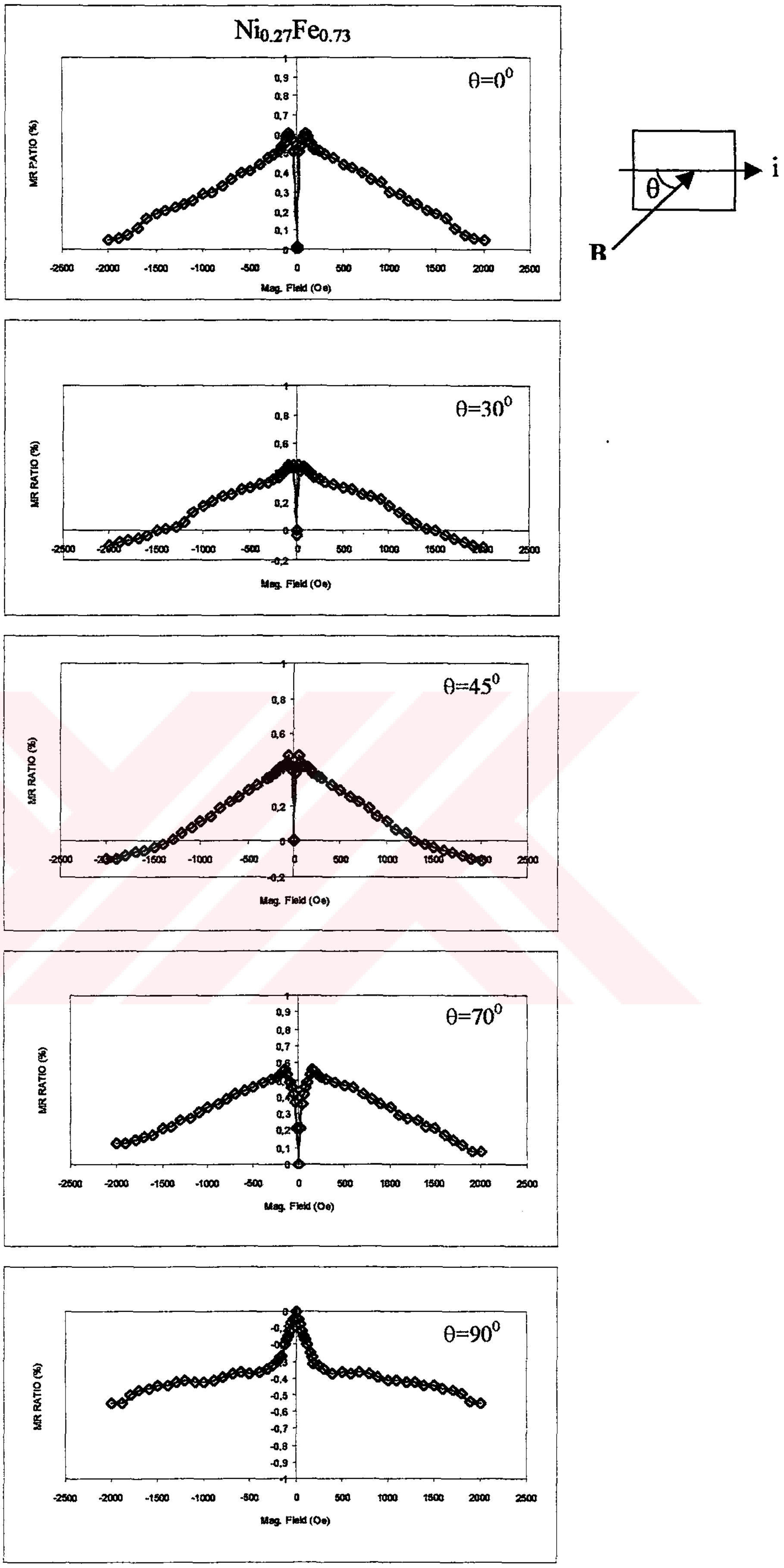

Figure 3.22 Continues on the next page

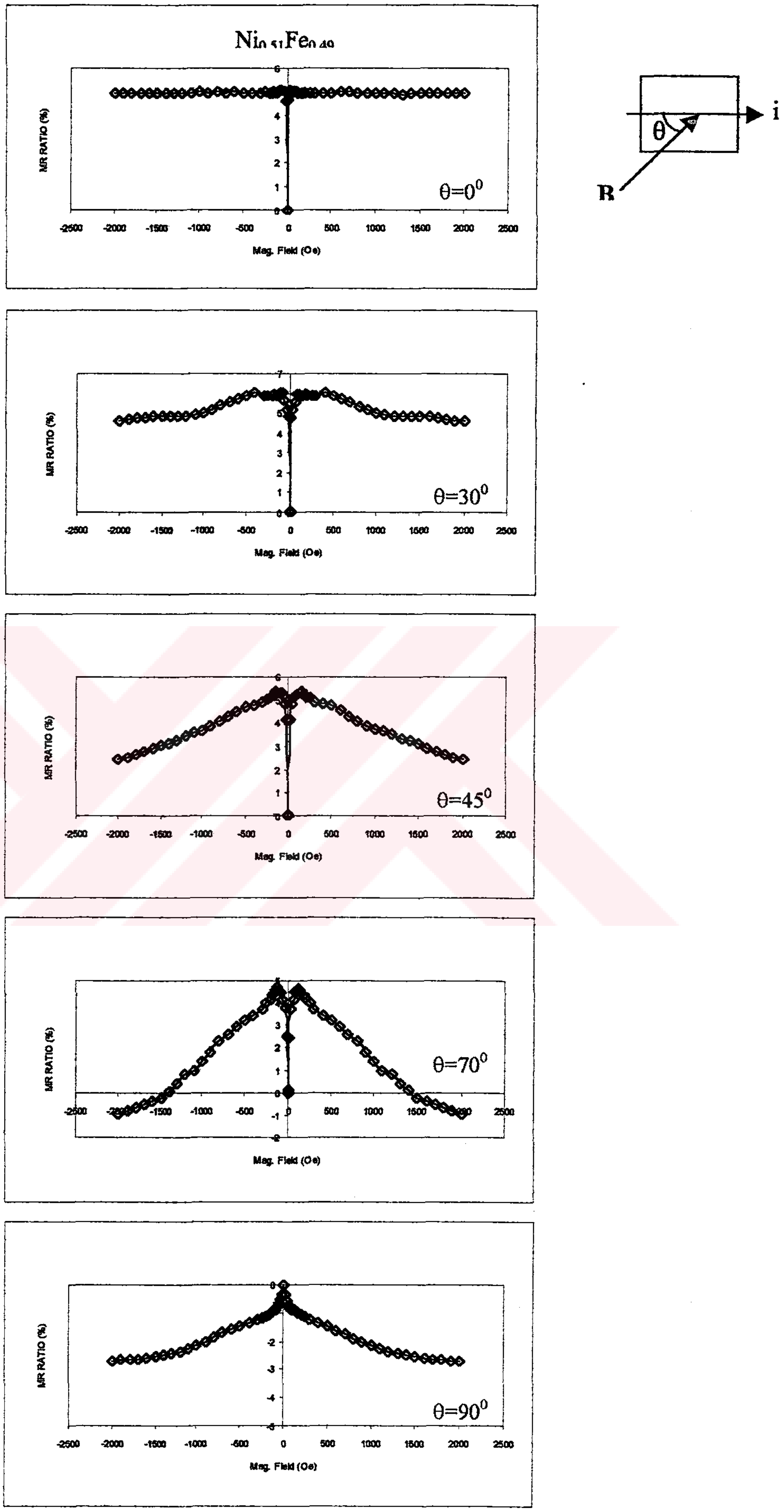

Figure 3.22 Continues on the next page

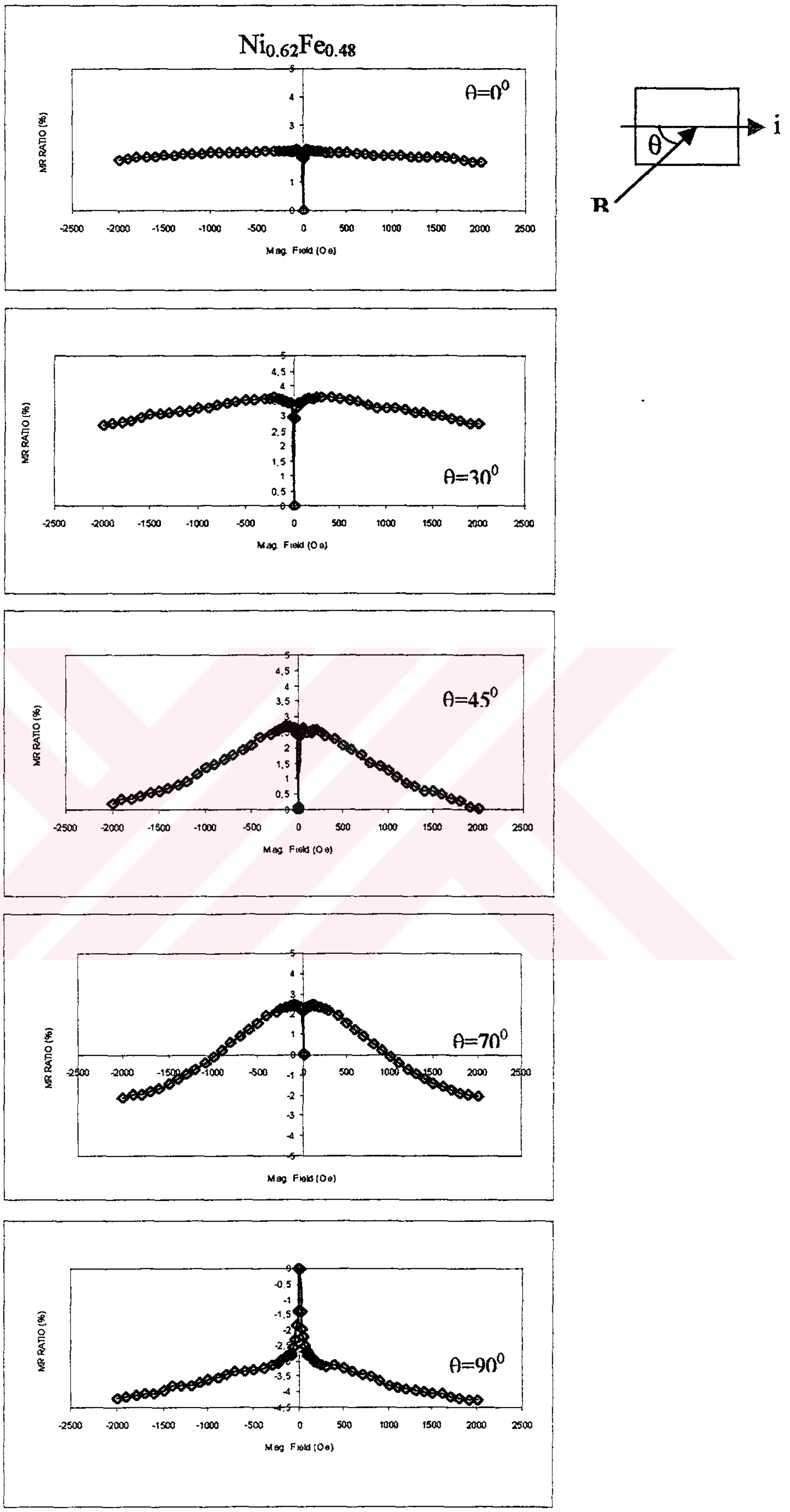

Figure 3.22 The angular variation of MR curves in NiFe samples from 0^0 to 90^0 for the longitudinal-perpendicular geometry at room temperature

The angular variation of the magnetoresistance curves from 0^0 to 90^0 for the longitudinal-perpendicular geometry is shown in Figure 3.22. Four samples of the electrodeposited NiFe alloy films were chosen to study angular variation of magnetoresistance effect. In these samples the magnetoresistance value jumps to a positive value for a very small magnetic field increase (>20 Oe).

The change from the pure positive magnetoresistance effect to the negative magnetoresistance effect with the gradual change in the direction of applied magnetic field from parallel to perpendicular to the film plane is clearly seen from the graphes in Figure 2.22.

As the angle between the applied field and the film plane increases, the magnetoresistance ratio decreases and it reaches to a negative magnetoresistance value at $\theta=90^0$ in the sample with x= 0.22, (Fig.2.22). In the sample with x=0.46, (Fig.2.22), as the angle between applied field and the film plane increases the saturation in magnetoresistance value is lost and a decreasing effect in magnetoresistance ratio emerges.

At $\theta=45^0$ the mixture of positive and negative magnetoresistance effect is slightly changing but at $\theta=70^0$ and $\theta=90^0$ this mixture magnetoresistance effect is dominant.

The other two samples with x=0.51 and 0.62, (Fig.2.22), clearly show magnetoresistance effect under the angular applied magnetic field. As the angle between the applied field and the film plane increases the saturation in magnetoresistance value is lost and a decreasing effect in magnetoresistance ratio emerges. At $\theta=45^0$ the mixture of positive and negative magnetoresistance effect is dominant.

Above 45^0 the positive magnetoresistance gradually loses its strength and mostly replaces with the negative magnetoresistance component at $\theta=90^0$. It is therefore seen from these two curves that the change from positive to negative magnetoresistance ratio appears to be not abrupt but a continuous one.

3.9.6 Temperature Dependence of Magnetoresistance Effect

In this part, the magnetoresistance measurements of the NiFe film samples were carried out for two configurations: (a) with a constant magnetic field applied parallel to the current direction and thin surface (longitudinal geometry), (b) with a constant magnetic field applied perpendicular to the current direction and film surface (longitudinal-perpendicular geometry) under the different temperatures 20 K≤ T ≤ 320 K. A schematic diagram of the temperature dependent magnetoresistance measurement system is shown in Figure 3.23.

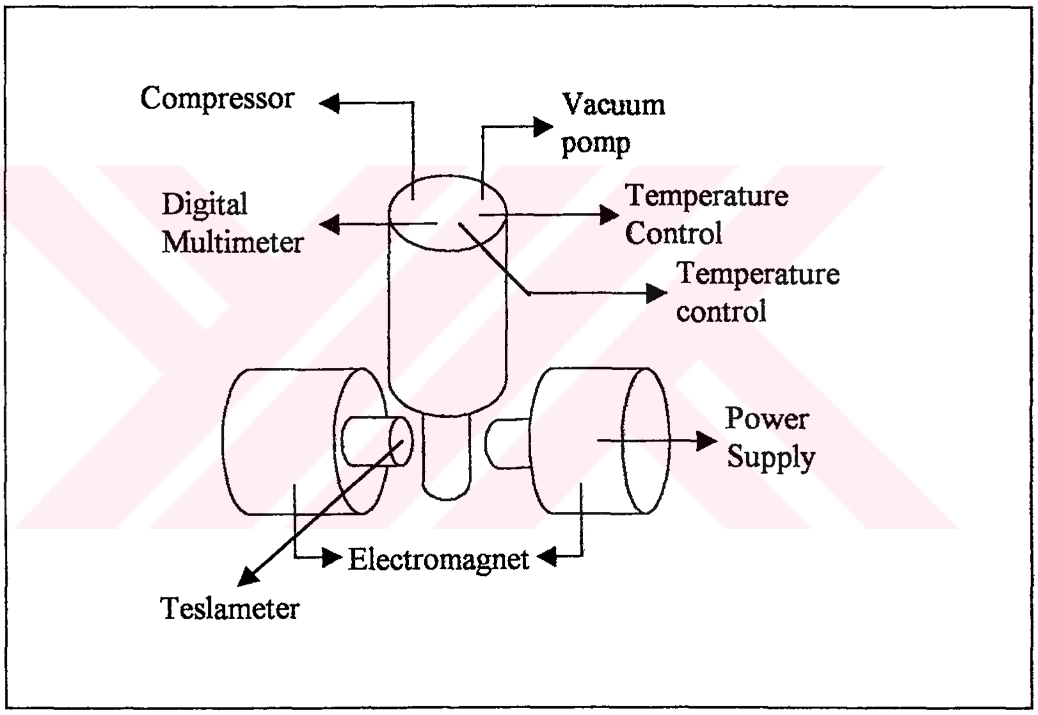

Figure 3.23 Temperature dependence magnetoresistance measurement system

This system consists of two main parts one is electromagnet (Varian mark and V-2900 Model) and the other is a closed helium cryostat (Leybold Serueus mark). For this process, thin film samples were prepared 4x4 mm in size and placed on the sample holder of the cryostat. The connections between the film and electrical leads were provided by the silver paste solution in the Van der Pauw configuration. Sample holder was properly inserted into the cryostat. Later, cryostat was vacummed with a vacumm pump and the temperature of the cryostat was decreased to 20K with a fluid of helium. A constant DC current of 10 mA was passed along the film surface. The potential difference between two points on the film surface was measured under the influence of a constant magnetic field of 0,8 Tesla at each temperature. The results of the temperature dependent magnetoresistance measurements are shown in Figure 3.24 and 3.25 for two different configuration, longitudinal and longitudinal-perpendicular geometries, repectively.

3.9.6.1 Temperature Dependence of Magnetoresistance Effect in Longitudinal Configuration

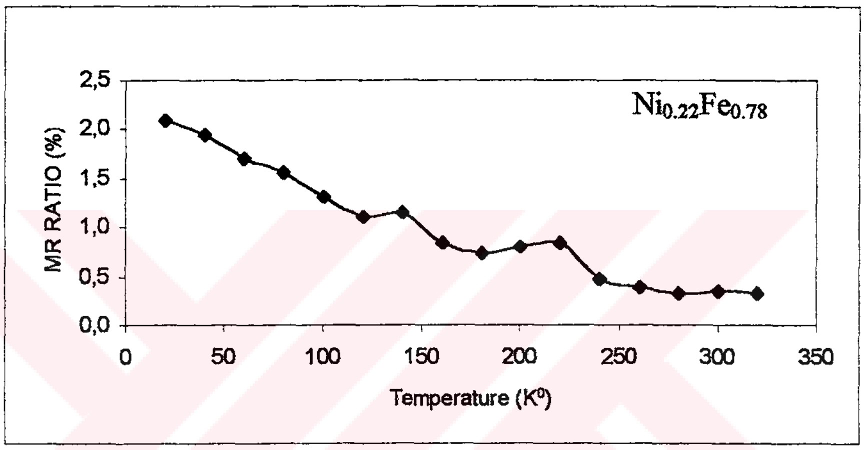

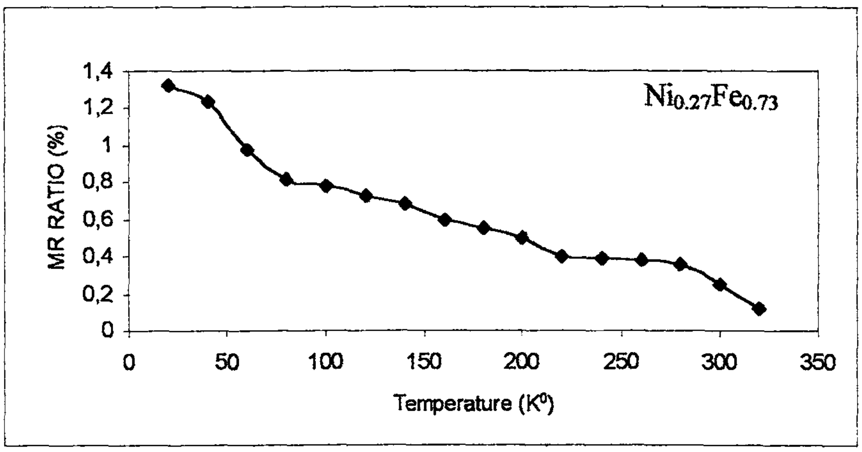

Figure 3.24 continues on the next page

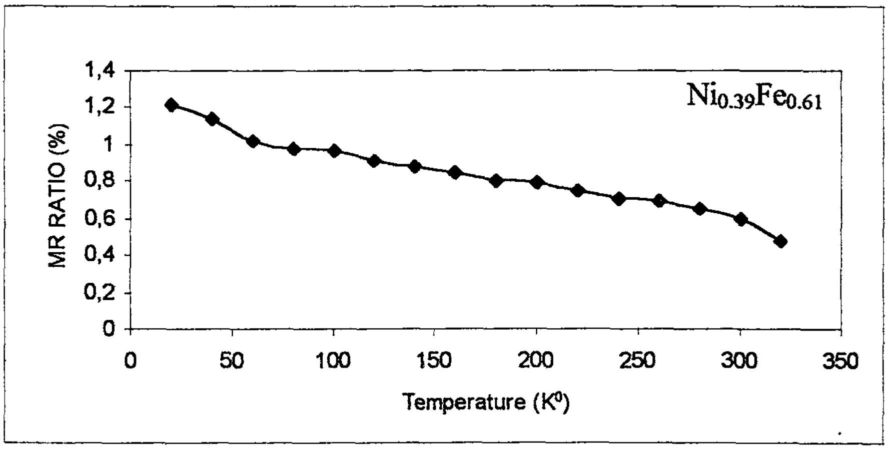

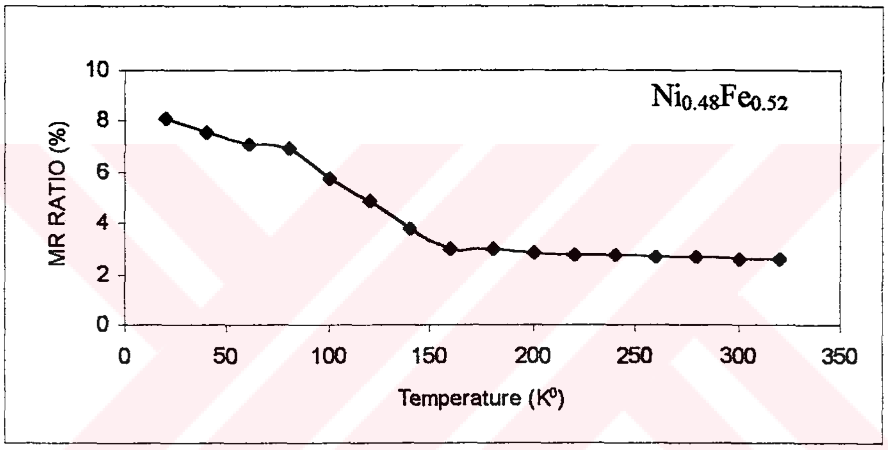

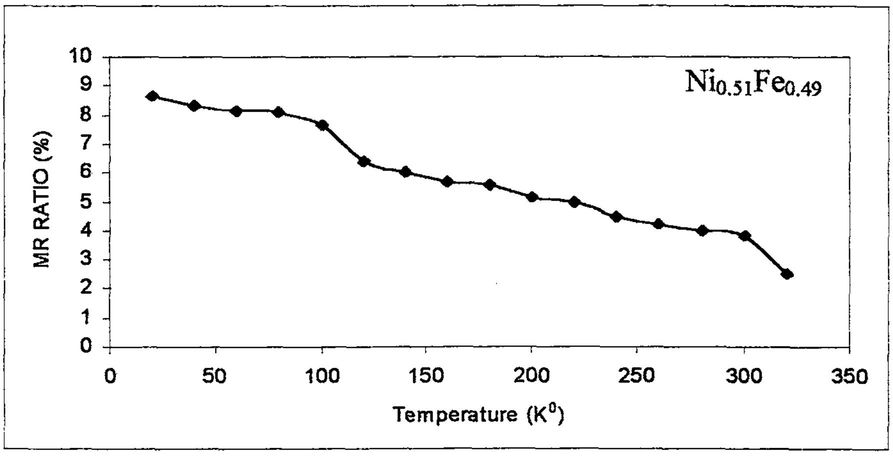

Figure 3.24 continuous on the next pages

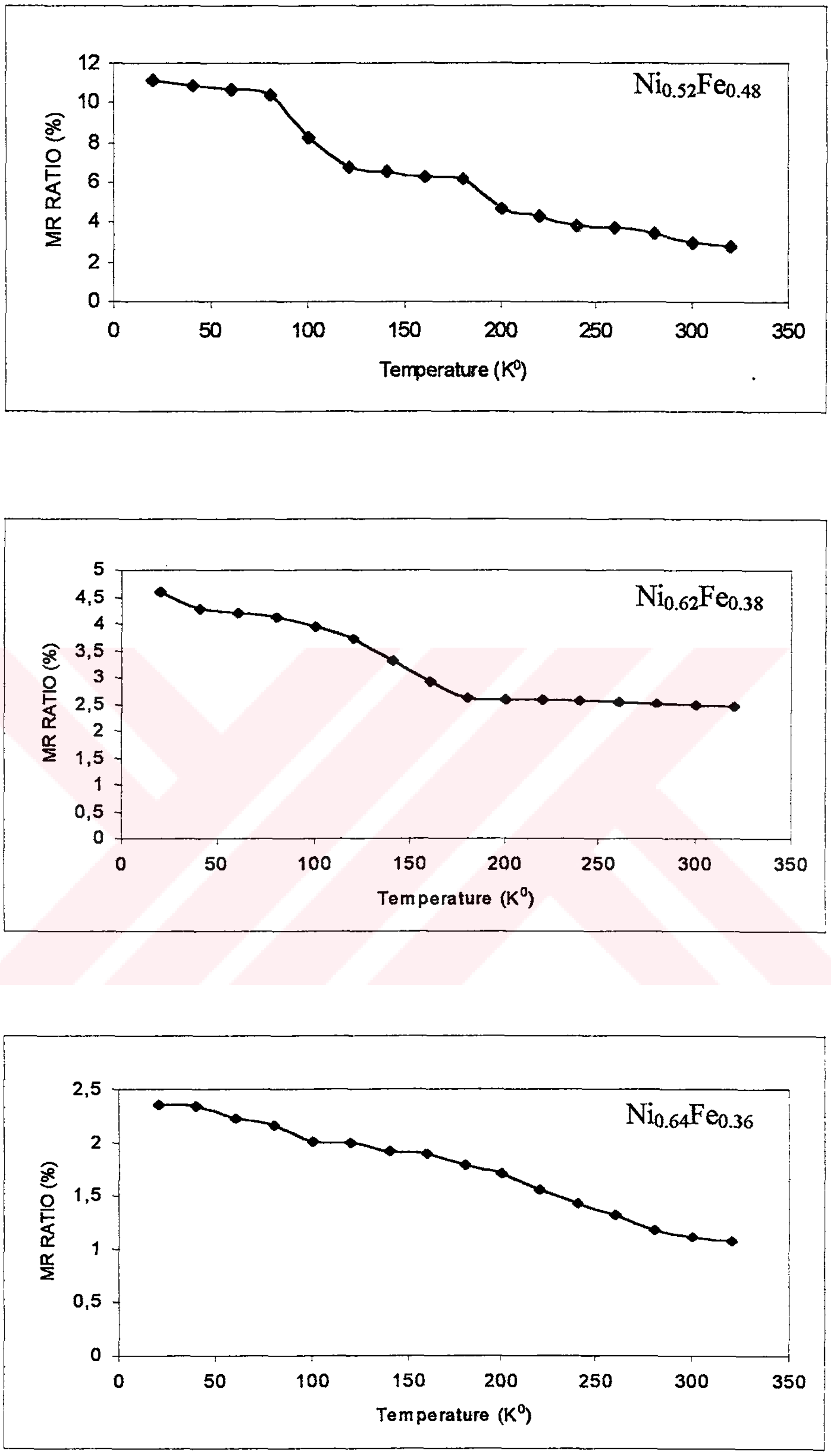

Figure 3.24 The temperature dependence MR measurement of $Ni_xFe_{(1-x)}$ films for parallel geometry

All of the samples in Figure 3.24 show an increase in the magnetoresistance ratio as temperature decreases. For at 320K, the magnetoresistance (MR) value of the samples with x=0.22, 0.27 and 0.39 is below 1% but for the other samples with x=0.48, 0.51, 0.52, 0.62 and 0.64 it is between the values of %1.5≤ MR ≤%2.5 at 320K. The MR values at 320K change order at 20K, because the variation of the MR ratio with the decrease in temperature is different for each sample. At 20K, for all of the samples MR ratio is higher than 1%. The increase in the MR ratio with decreasing temperature may represent the reduction in spin-magnon scattering at lower temperatures i.e. represent the relative reduction in the number of magnons. The values and proportions of the MR ratios at 320K and 20K are given in Table 3.3 for the longitudinal configuration measurements.

Table 3.3 The values of MR ratios at 320K and 20K while the last column gives the change in MR ratio for each sample between 320K and 20K for parallel configuration

Sample	MR ratio (320K)	MR ratio (20K)	{1-[(MR(320K))/(MR(20K))]}
$Ni_{0.22}Fe_{0.78}$	0.0033	0.021	0.84
$Ni_{0.27}Fe_{0.73}$	0.0012	0.0132	0.90
$Ni_{0.39}Fe_{0.61}$	0.00597	0.0121	0.51
$Ni_{0.48}Fe_{0.52}$	0.0261	0.0808	0.68
$Ni_{0.51}Fe_{0.49}$	0.0248	0.0866	0.71
$Ni_{0.52}Fe_{0.48}$	0.0278	0.1117	0.75
$Ni_{0.62}Fe_{0.38}$	0.0245	0.0459	0.47
$Ni_{0.64}Fe_{0.36}$	0.0108	0.0236	0.54

In Table 3.3, the fourth column shows the change in the MR ratio between 320K and 20K and may be considered to be the percentage decrease in the number of magnons in this temperature range. The largest decrease in the number of magnons is seen in the $Ni_{0.27}Fe_{0.73}$, which also has the second largest decrease in the resistivity, with decreasing temperature, while the lowest magnon decrease occurs in the $Ni_{0.62}Fe_{0.38}$ sample. The values in the fourth column may also represent the percentage magnon part of the change in the resistivity values, which decrease due to the phonon+magnon reduction with decreasing temperature from 320K to 20K.

3.9.6.2. Temperature Dependence of Magnetoresistance Effect in Longitudinal -Perpendicular Configuration

Figure 3.25 shows the temperature dependent magnetoresistance (MR) measurements which were performed from 320K to 20K under the influence of a constant magnetic field of 0.8T in the longitudinal-perpendicular geometry. From these figures, at 320K, the MR values of the samples of x=0.22 and 0.27 are below 1% and other samples of x=0.52, 0.62 and 0.64 have higher values than 1%, between 1.6% and 3.36%. The samples of x=0.39, 0.48 and 0.51 have a negative magnetoresistance value at 320K which changes order at 20K. The negative MR values of these samples at 320 K are greater than 1%. The increase in the MR ratio with decreasing temperature, similar to the result of the longitudinal geometry, may represent the reduction in spin-magnon scattering at lower temperature i.e. represent the relative reduction in the number of magnons. And also it is observed that the measurement geometry affects the magnitude of magnetoresistance value.

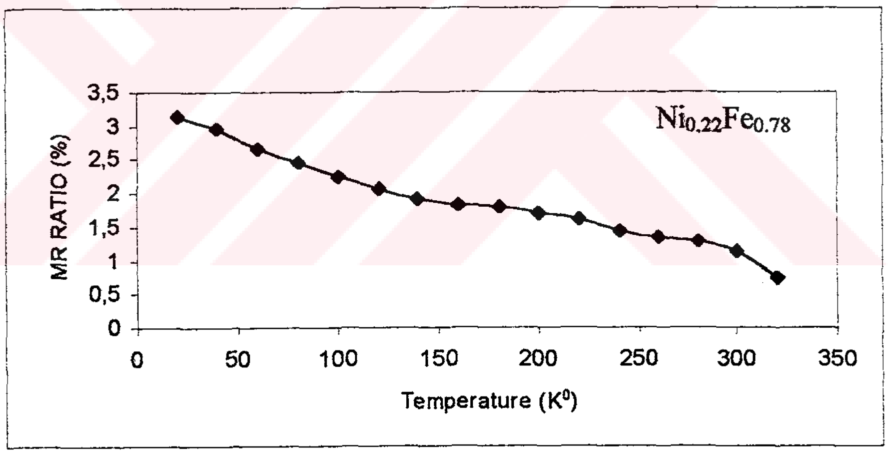

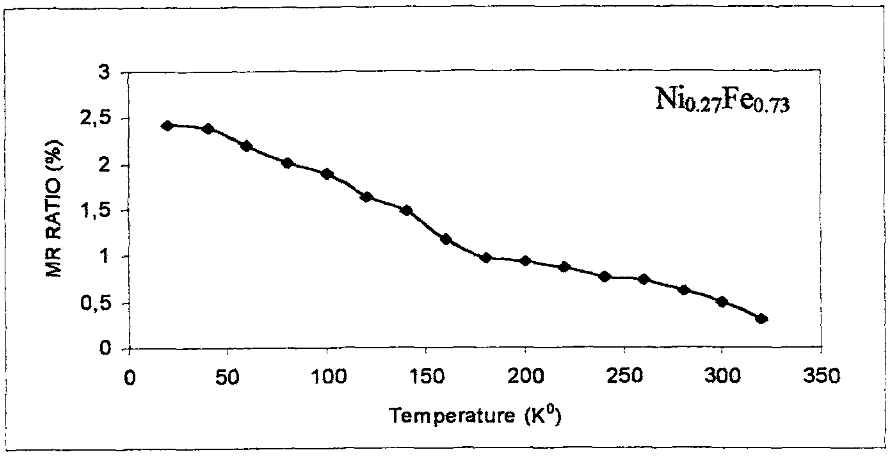

Figure 3.25 continues on the next pages

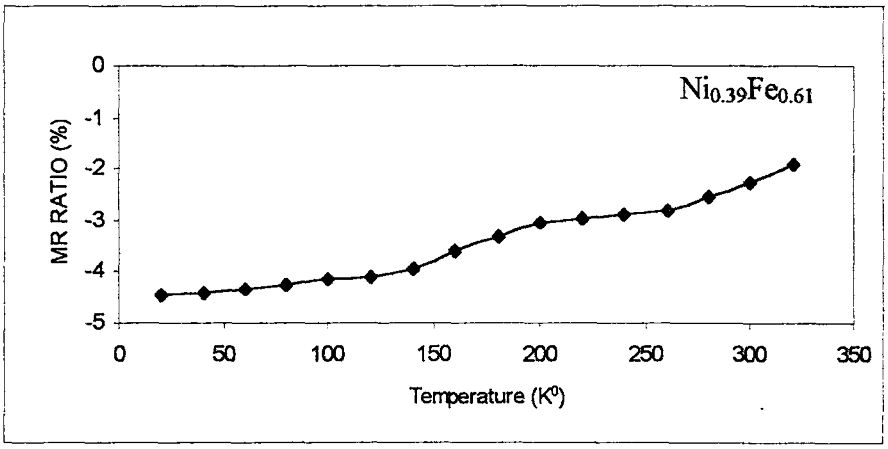

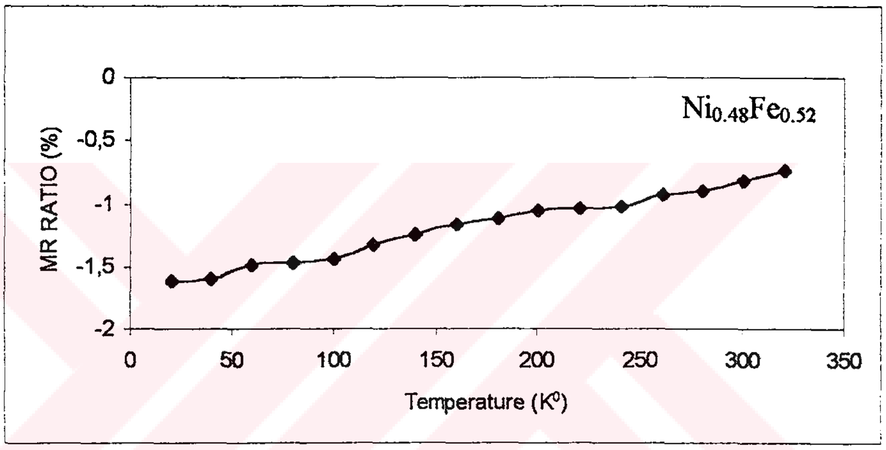

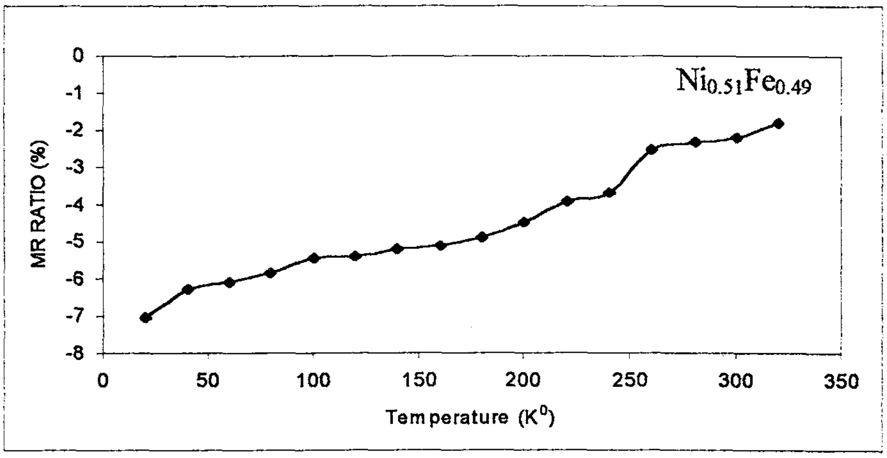

Figure 3.25 continues on the next pages

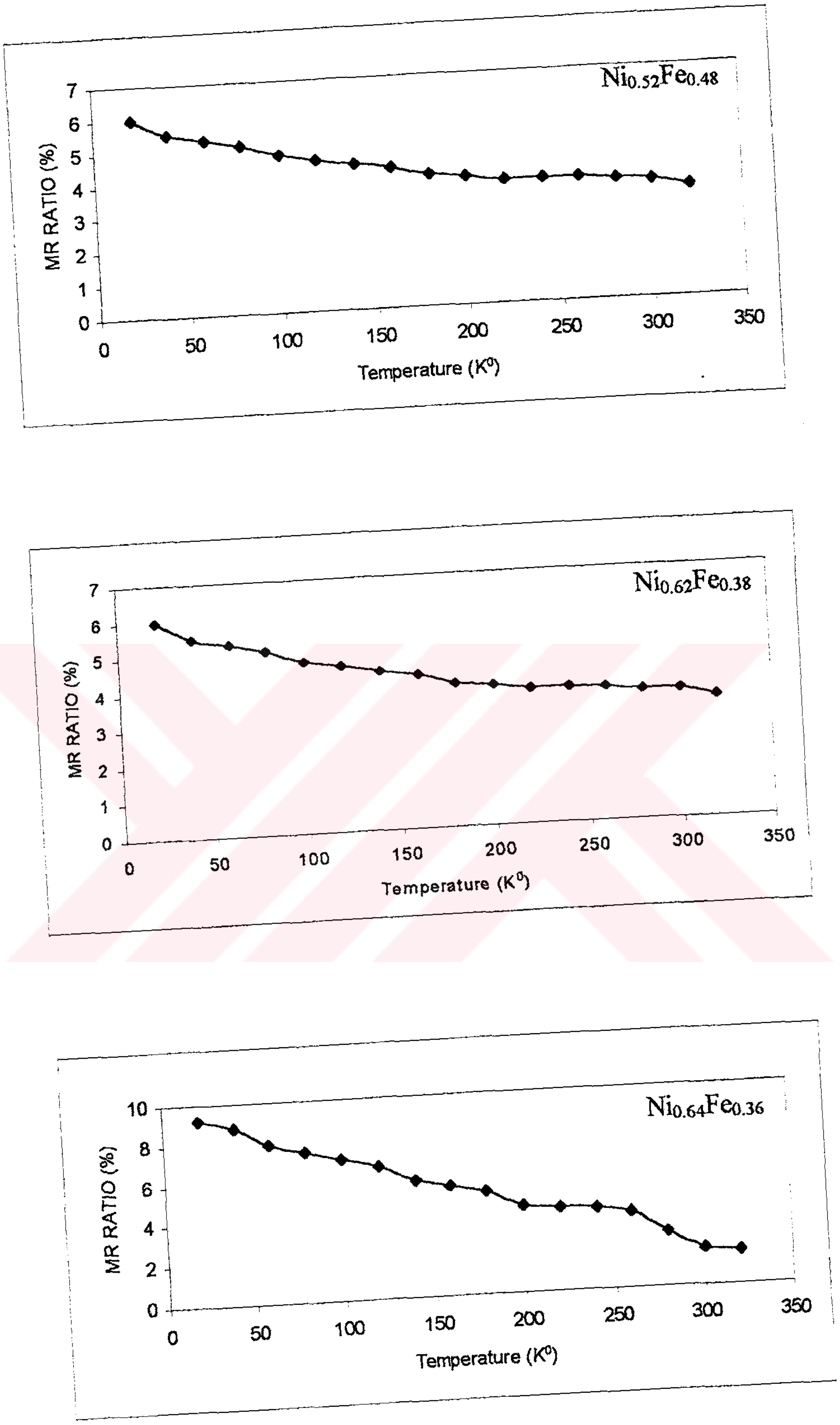

Figure 3.25 Temperature dependence MR measurement of $Ni_xFe_{(1-x)}$ films for perpendicular geometry

The values and proportions of the MR ratios at 320K and 20K for longitudinal-perpendicular configuration measurements are given in Table 3.4

Table 3.4 The values of MR ratios at 320K and 20K while the last column gives the change in MR ratio for each sample between 320K and 20K for longitudinal-perpendicular configuration

Sample	MR ratio (320K)	MR ratio (20K)	{1-[(MR(320K))/(MR(20K))]}
$Ni_{0.22}Fe_{0.78}$	0.0075	0.0313	0.76
$Ni_{0.27}Fe_{0.73}$	0.003	0.0242	0.88
$Ni_{0.39}Fe_{0.61}$	-0.0189	-0.0444	0.57
$Ni_{0.48}Fe_{0.52}$	-0.0073	-0.0162	0.55
$Ni_{0.51}Fe_{0.49}$	-0.0181	-0.0705	0.74
$Ni_{0.52}Fe_{0.48}$	0.0336	0.06	0.44
$Ni_{0.62}Fe_{0.38}$	0.0168	0.0512	0.67
$Ni_{0.64}Fe_{0.36}$	0.0921	0.0167	0.45

In this Table 3.4, the fourth column shows the change in the MR ratio between 320K and 20K and may be considered to be the percentage decrease in the number of magnons in this temperature range.

The largest decrease in the number of magnons is seen in the $Ni_{0.27}Fe_{0.73}$ sample which also has the second largest decrease in the resistivity with decreasing temperature, while the lowest magnon decrease occurs in the $Ni_{0.52}Fe_{0.48}$ sample. The values in the fourth column may also represent the percentage magnon part of the change in the resistivity values, which decrease due to the phonon+magnon reduction with decreasing temperature from 320K to 20K.

3.9.7 Magnetization Measurements Using Vibrating Sample Magnetometer

The vibrating sample magnetometer (VSM) was developed in 1956 by S.Foner and by Van Osterhart. According to Faradays laws of magnetic induction, an ac voltage is induced in the electrical circuit which is proportional to the rate of change of magnetic flux linking the circuit, and therefore to the size of the moment within the sample due to the applied magnetic field.

As the sample is vibrated in the vertical direction near the detection coil, an ac signal is generated at a frequency determined by the sample oscillation. A schematic of the VSM set-up is shown in the Figure 3.26.

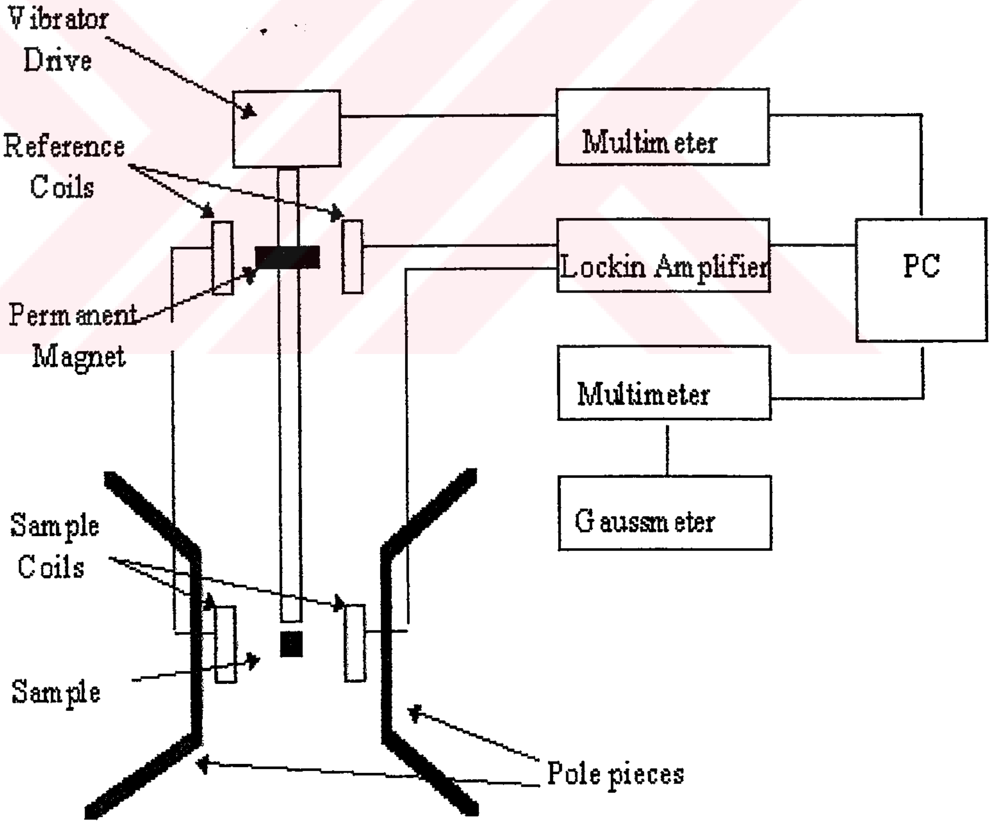

Figure 3.26 A schematic of the VSM set-up

If a material is placed within a uniform magnetic field, a magnetic moment m will be induced in the sample. In a VSM, a sample is positioned within suitably placed sample coils, and is made to undergo sinusoidal motion, i.e., mechanically vibrated. The resulting magnetic flux changes induce a voltage in the sample coils that is proportional to the magnetic moment of the sample. The applied field may be produced by an electromagnet.

A common application of vibrating sample magnetometry (VSM) is the characterization of magnetic materials. Using a VSM it is possible to measure the saturation flux density B_s, the coercivity H_c, the total magnetic field moment as a function of applied magnetic field, from which saturation magnetization, magnetic anisotropy, and exchange of magnetic layers can be determined.

The magnetic properties of the NiFe magnetic film samples were investigated with a vibrating sample magnetometer (VSM 3900 Model) at room temperature. In this measurements the magnetic field was applied both parallel and perpendicular to the sample surface. The dimensions of the films used in the VSM measurements were 4mm x 4mm.

The systematic room temperature measurements of the hysteresis loop of NiFe films allowed us to determine; the antiferromagnetic fraction $F_{AF}= 1-(M_R/M_S)$ in the NiFe alloys where M_R and M_S denote the remanent and saturation magnetization, respectively. The VSM hysteresis loop measurements of NiFe film samples are shown in Figure 3.27 and 3.28 for parallel and perpendicular configurations, respectively.

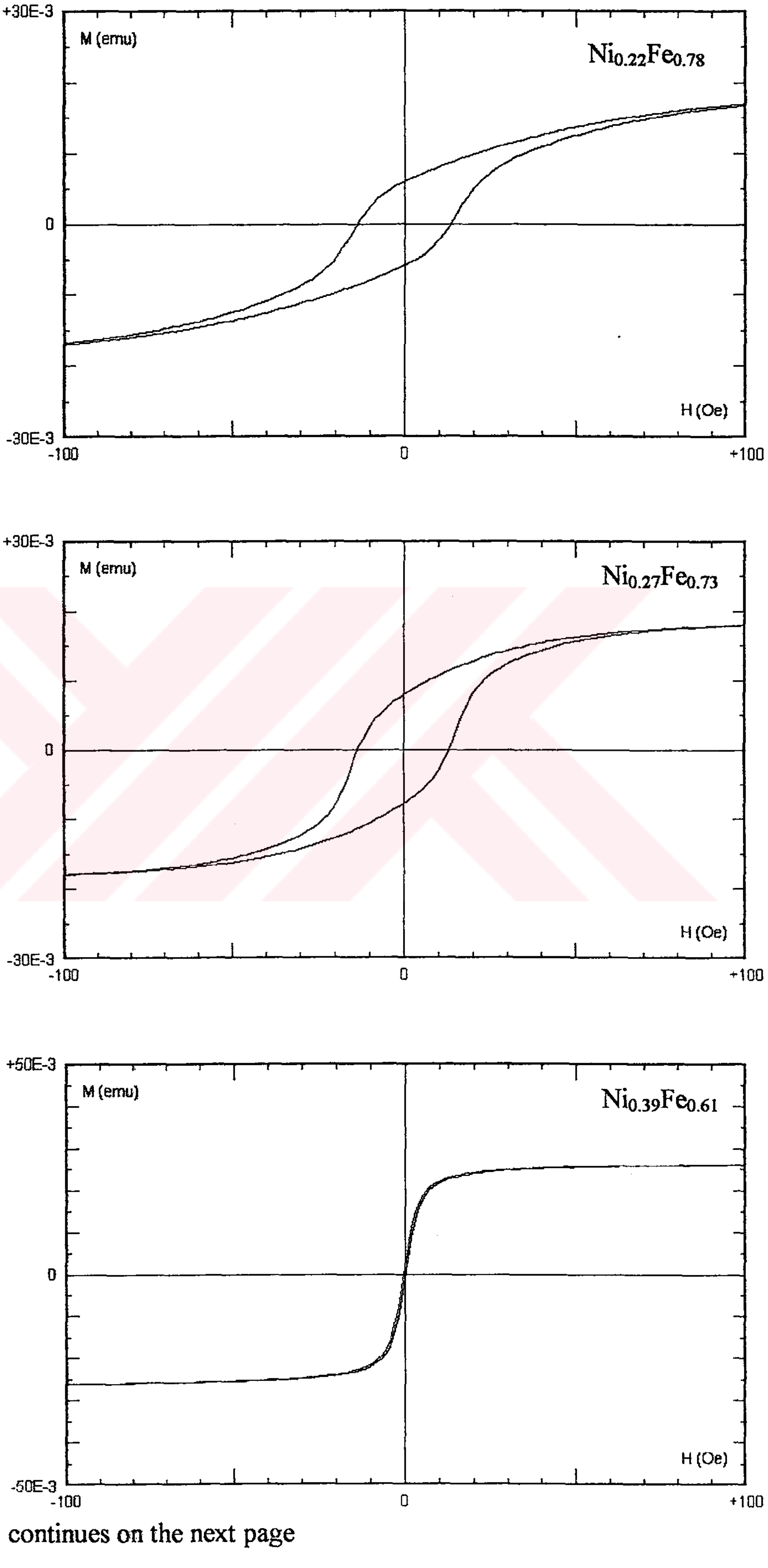

Figure 3.27 continues on the next page

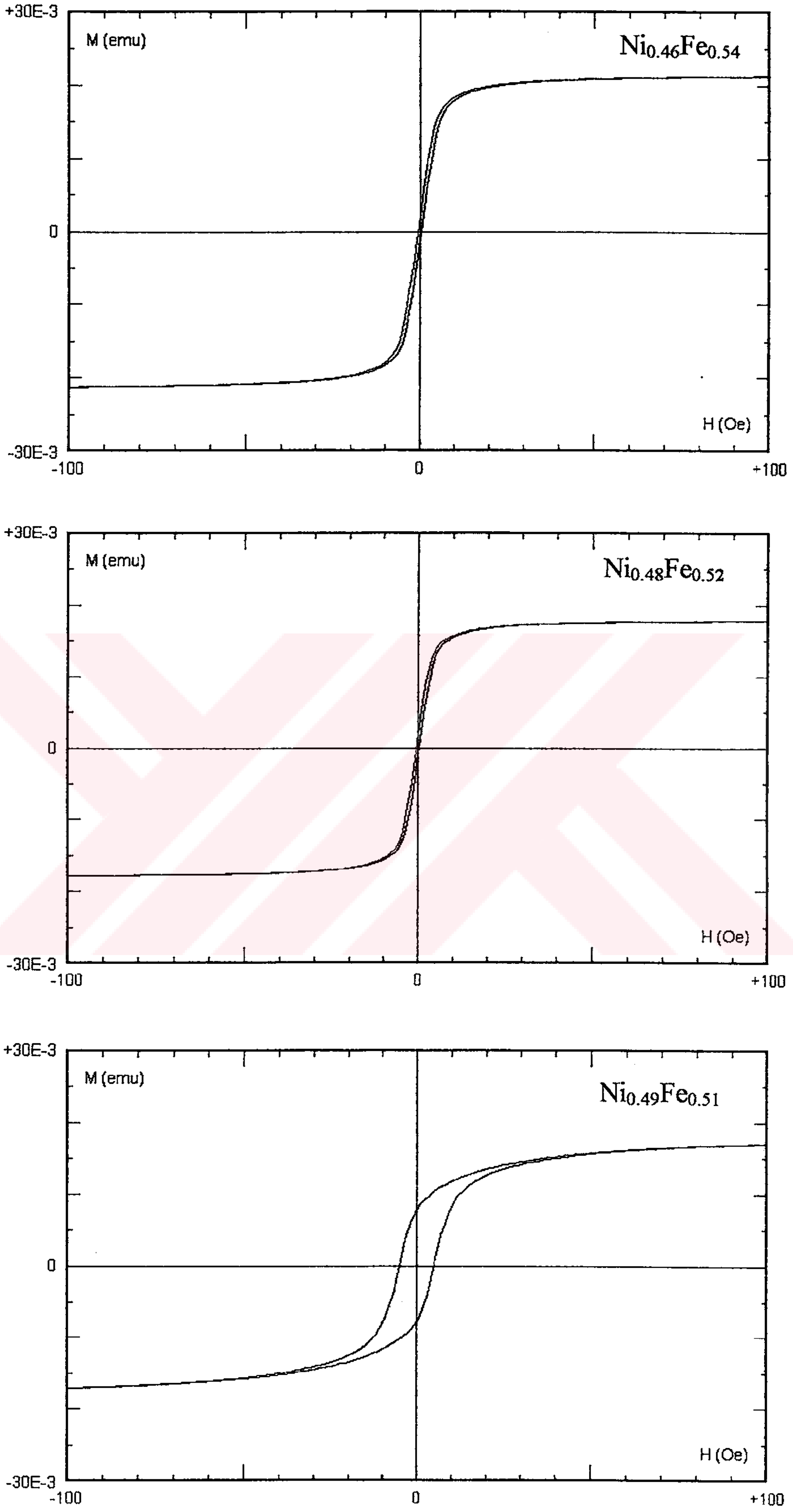

Figure 3.27 continues on the next page

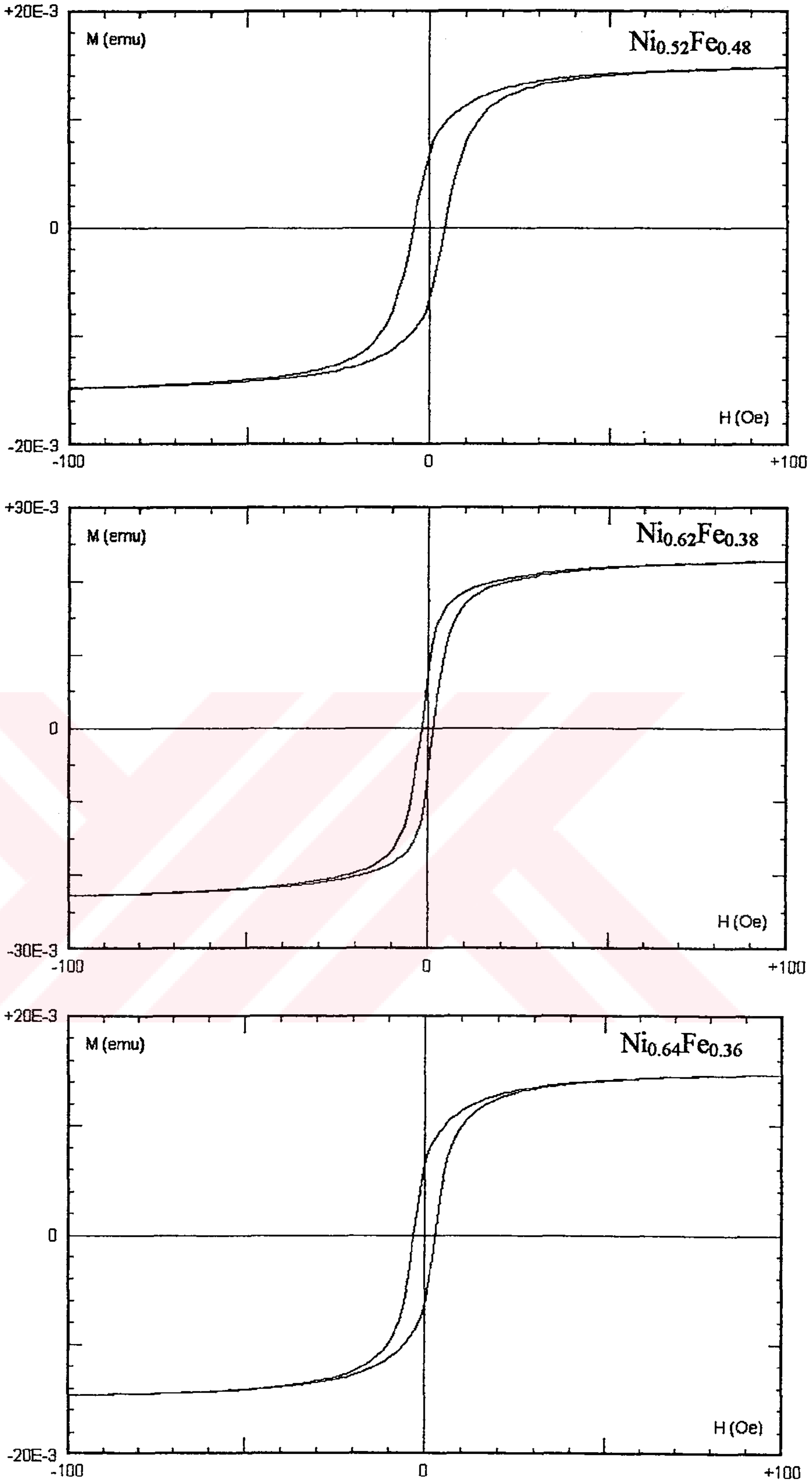

Figure 3.27 The magnetization loops of $Ni_xFe_{(1-x)}$ samples were measured using a vibrating sample magnetometer with magnetic field applied parallel to the film plane at room temperature

As it can be seen from Figure 3.27 that the $Ni_{0.22}Fe_{0.78}$ and $Ni_{0.27}Fe_{0.73}$ alloy films have larger and unsaturated loops than the other seven samples (with x= 0.39, 0.46, 0.48, 0.49, 0.52, 0.62, 0.64), which have relatively smaller loops and saturated easily at low fields.

As it is remembered from section (3.9.4) that the $Ni_{0.22}Fe_{0.78}$ and $Ni_{0.27}Fe_{0.73}$ samples show a significant mixture of positive and negative magnetoresistance effect whereas the other samples have pure positive or negative ones (see Figs.3.18 and 3.19) when the magnetic field is applied parallel to the film plane.

The large and unsaturated hysteresis loops at low fields indicate a larger distribution of Ni and Fe components in the $Ni_{0.22}Fe_{0.78}$ and $Ni_{0.27}Fe_{0.73}$ samples and may be the cause of the significant mixture of the positive and negative MR effect in this geometry although the large and unsaturated loops may be expected to give rise to higher MR effect which is not the case in the samples with high Ni content.

For all of the $Ni_xFe_{(1-x)}$ alloy film samples, the coercive field (H_c) and the ratio of the remanence (M_r) to magnetization (M_s) values obtained by VSM are given in Table 3.5.

Table 3.5 Coerciev field H_c, saturation magnetization M_s and M_r/M_s at 22 kOe values obtained by vibrating sample magnetometer (VSM) measurements, where M_r is remenance.

Sample	H_c (Oe)	M_r (memu)	M_s (memu)	M_r/M_s
$Ni_{0.22}Fe_{0.78}$	13.47	5.900	16.99	0.3472
$Ni_{0.27}Fe_{0.73}$	13.19	7.827	17.96	0.4358
$Ni_{0.39}Fe_{0.61}$	0.266	1.316	26.13	0.0503
$Ni_{0.46}Fe_{0.54}$	0.477	1.651	21.31	0.0775
$Ni_{0.48}Fe_{0.52}$	0.418	1.416	17.80	0.0796
$Ni_{0.49}Fe_{0.51}$	4.922	7.804	17.06	0.4574
$Ni_{0.52}Fe_{0.48}$	4.209	6.759	14.83	0.4558
$Ni_{0.62}Fe_{0.38}$	1.576	6.862	22.80	0.301
$Ni_{0.64}Fe_{0.36}$	2.871	6.407	14.68	0.4366

The maximum saturated magnetization value M_s(emu/cm^3) at 22 kOe was detected in the $Ni_{0.46}Fe_{0.54}$ sample (Table 3.5). The coercive field H_c and the ratio of the remanence (M_r) to the saturation magnetisation M_s (at 22 kOe) at room temperature are also given in Table 3.5.

The coercieve fields have relatively low values, which is in agreement with other studies [e.g. 8,12], indicating soft magnetic properties and they are almost in the same range as the magnetic field at which the maximum positive MR effect is observed.

The M_r/M_s value varies between 7.6% for $Ni_{0.46}Fe_{0.54}$ and 45.7% for $Ni_{0.49}Fe_{0.51}$ indicating the degree of the ferromagnetic alignment of NiFe particles in our samples and it puts an upper limit of ~5–46% on the ferromagnetically coupled and ~54% on the non-ferreomagnetically coupled fractions in the samples for the parallel geometry measurement.

The highest positive MR value in the longitudinal geometry corresponds to the sample which has the lowest M_r/M_s ratio while in the transverse geometry the highest value of negative MR belongs to the $Ni_{0.51}Fe_{0.49}$ sample.

As seen in Figure 3.27 the samples with $x \geq 0.39$ are saturated more easily when compared to the other samples with $x \leq 0.27$ which have more inclined magnetization curves. This may indicate a more disordered arrangement of Ni atoms and therefore less degree of ferromagnetic order in x=0.22 and 0.27 alloy films. The biggest coercive field H_c is detected in the $Ni_{0.22}Fe_{0.78}$ alloy film.

The coercive field H_c (at room temperature) show a decreasing behaviour with increasing Ni content in the film. The biggest value of M_r/M_s (at room temperature) is observed 45.7% with x=0.49 and the lowest value of M_r/M_s (at room temperature) is observed 5% with x=0.39.

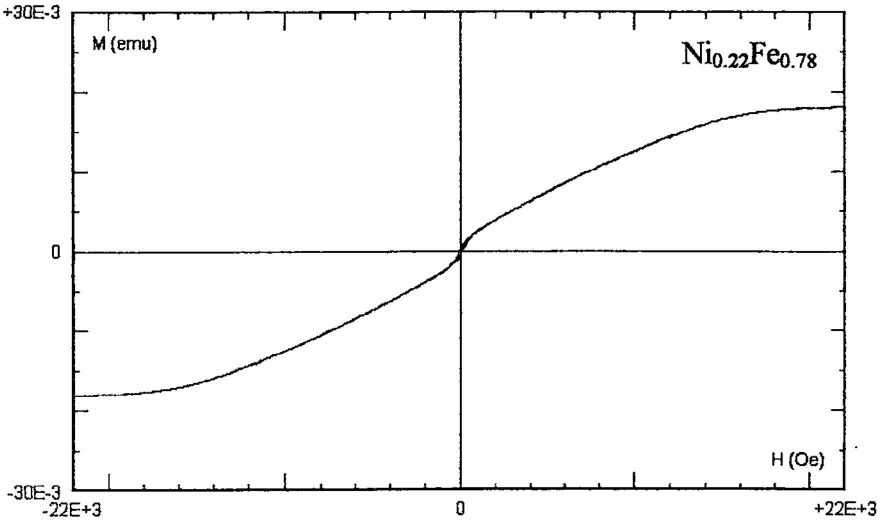

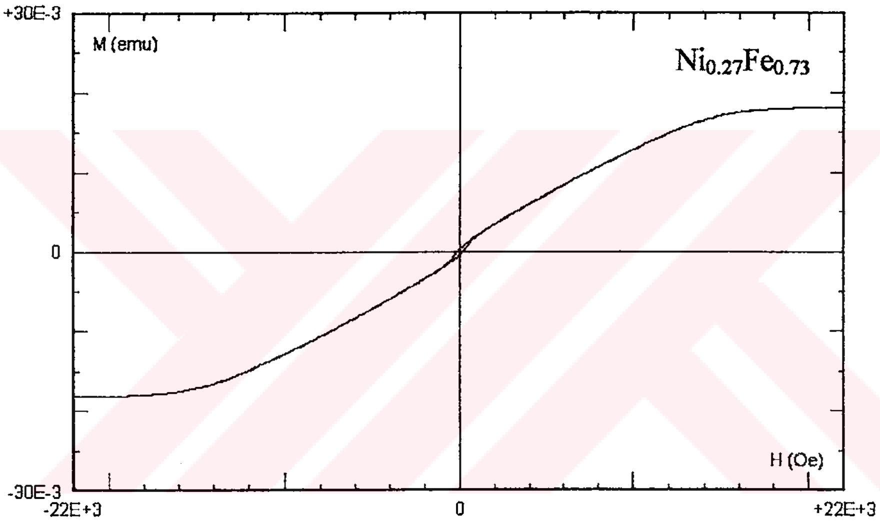

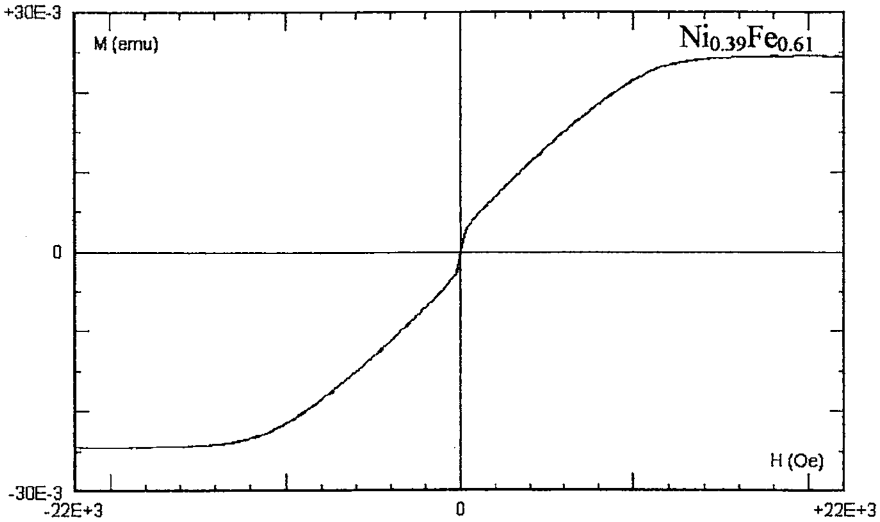

Figure 3.28 continues on the next page

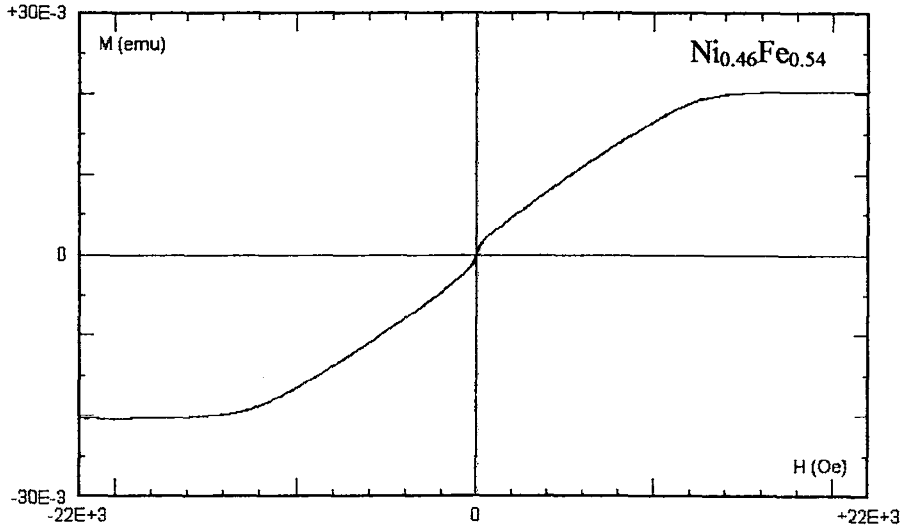

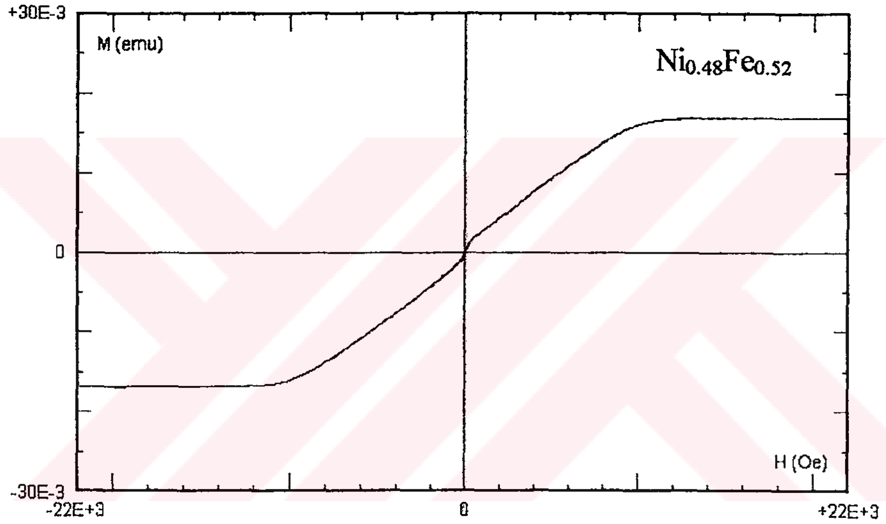

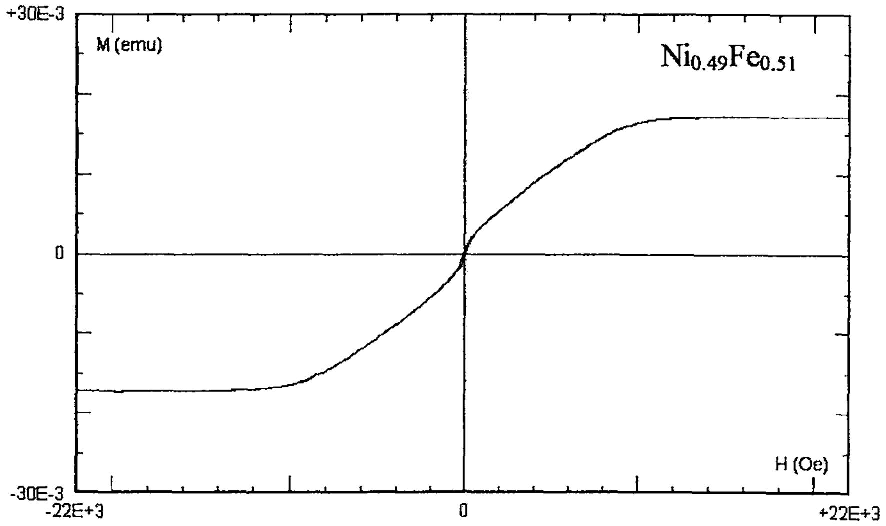

Figure 3.28 continues on the next page

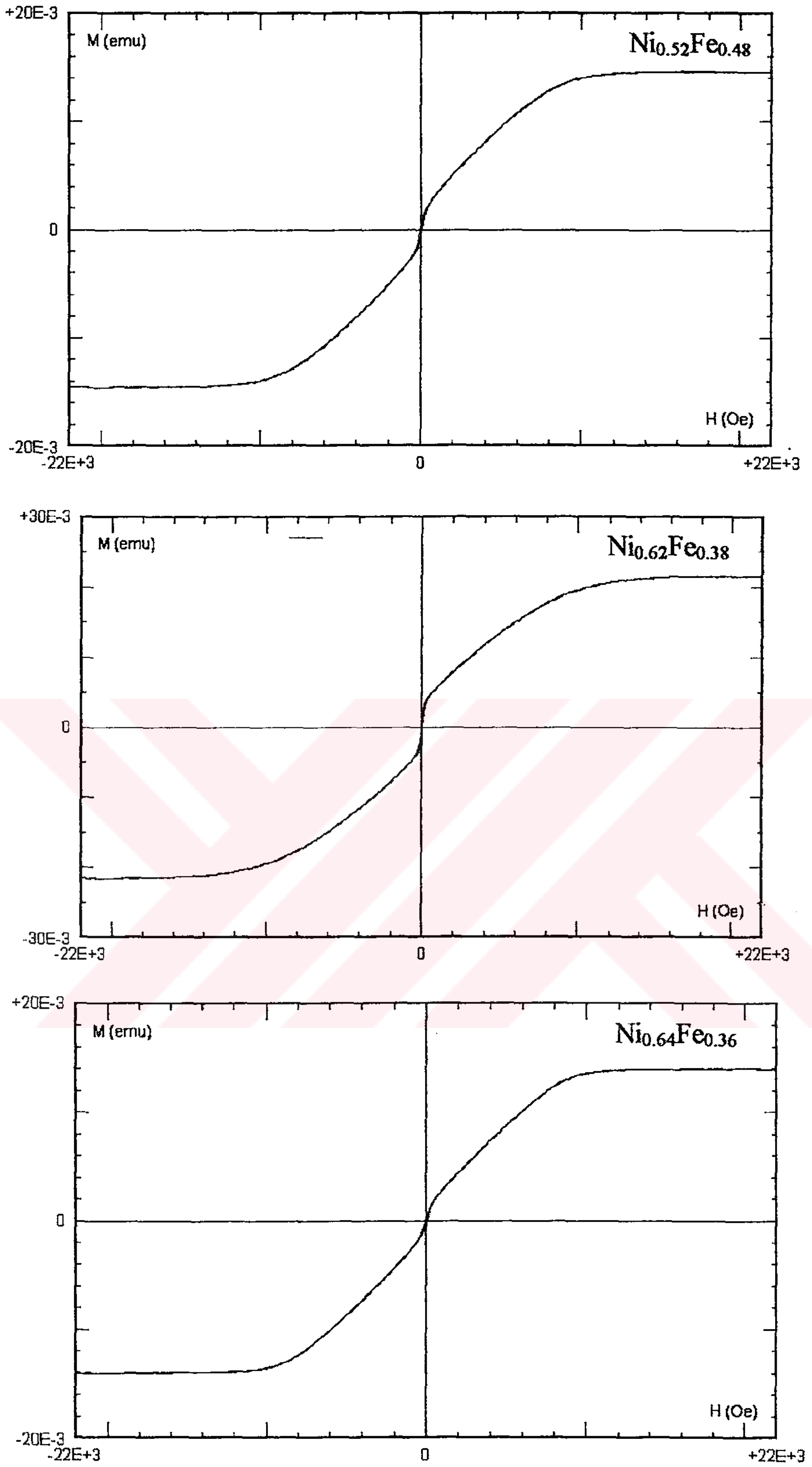

Figure 3.28 The magnetization loops of $Ni_xFe_{(1-x)}$ samples were measured using a vibrating sample magnetometer with magnetic field applied perpendicular to the film plane at room temperature

Figure 3.28 shows the hysteresis loops recorded with the field applied perpendicularly to the film surface of $Ni_xFe_{(1-x)}$ alloy samples.

Each loop clearly shows a low coercivity but higher than that of the parallel configuration. The low coercivity is attributed to a small grain size in the film samples.

And also the magnetization curves of various $Ni_xFe_{(1-x)}$ alloy films show a fairly higher and unsatured loops. It can be deduced from the comparison of the hysteresis loops taken in parallel (Fig.3.27) and perpendicular (Fig.3.28) configuration that the easy direction of the magnetization is in the film plane while the hard direction lies perpendicular to the film plane, which are in agreement with the theoretical interpretations in Chapter III (3.5.1).

For all of the $Ni_xFe_{(1-x)}$ alloy film samples the coercive field (H_c) and the ratio of the remanence (M_r) to magnetization (M_s) values obtained for perpendicular configuration by VSM measurements are given in Table 3.6.

Table 3.6 Coerciev field H_c, saturation magnetization M_s and M_r/M_s at 22 kOe values obtained by vibrating sample magnetometer (VSM) measurements, where M_r is remenance.

Sample	H_c (Oe)	M_r (μemu)	M_s (memu)	M_r/M_s
$Ni_{0.22}Fe_{0.78}$	69.48	323.5	18.10	0.0179
$Ni_{0.27}Fe_{0.73}$	146	354.1	18.16	0.0190
$Ni_{0.39}Fe_{0.61}$	4.457	51.47	24.50	0.0021
$Ni_{0.46}Fe_{0.54}$	20.75	125.5	20.32	0.0062
$Ni_{0.48}Fe_{0.52}$	19.04	97.02	16.90	0.0057
$Ni_{0.49}Fe_{0.51}$	47.78	335.2	17.21	0.0195
$Ni_{0.52}Fe_{0.48}$	37.42	311.7	14.58	0.0214
$Ni_{0.62}Fe_{0.38}$	5.388	99.79	21.56	0.0046
$Ni_{0.64}Fe_{0.36}$	37.60	221.5	13.97	0.0159

As seen from this table, The biggest coercive field is detected in the $Ni_{0.27}Fe_{0.73}$ alloy film and the lowest coercive field is detected in the $Ni_{0.62}Fe_{0.38}$ with 22kOe. The biggest Mr/Ms value is observed %2.14 in $Ni_{0.52}Fe_{0.48}$ and the lowest Mr/Ms value is observed to be %0.46 in $Ni_{0.62}Fe_{0.38}$ alloy thin film at room temperature and puts an upper limit of 0.46%-2.14% on the fraction of the samples that could be ferromagnetically coupled along the perpendicular direction to the film plane while over ≈ 98% non-ferromagnetic coupling could exist along the same direction in our samples.

3.10 Conclusions

In this work, Ni_xFe_{1-x} alloy films were fabricated with different compositions by using electrodeposition method and their crystal structure and magnetical properties were investigated. The NiFe alloy films were deposited at a current density of 16 mA/cm^2, a deposition time of 15 min, a pH value of 3. The temperature of the solution was kept at room temperature during the deposition process and no stirring was done.

The compositions and thickness of the samples were determined by Atomic Absorption Spectrophotometer results with the density mass and volume relation. NiFe diffraction lines were detected by using x-ray diffractometer at a diffraction angle where the FCC Ni and BCC Fe diffraction lines are expected. The lattice constant of NiFe alloy film was calculated using x-ray spectra of the films. It was found that the lattice constant of NiFe alloy film increases with increasing Ni content. The surface morfology of the NiFe alloy film was investigated by Scanning Electron microscopy photos. It is observed that the surface of the films has granular structure and smooth surface.

The magnetoresitive properties of NiFe alloy films were investigated for different geometries. The NiFe alloy film samples with $x \geq 0.39$ show a pure positive magnetoresistance effect while others show a mixture of positive and negative magnetoresistance effect and no pure negative magnetoresistance component was detected in the longitudinal geometry. In the transverse geometry, the samples show a negative magnetoresistance effect while as the samples with $x \leq 0.39$ also showed the positive component of the magnetoresistance effect. The other samples showed dominant negative component effect and were saturated just above ≥ 20 Oe.

Magnetoresistance effect was also investigated for magnetic field applied at the different angles. The angular variation in magnetoresistance measurements were carried out from 0^0 to 90^0 for longitudinal-perpendicular geometry. These results showed that, as the angle between the applied field and the film plane increases, the magnetoresistance ratio decreases. The magnetoresistance measurements also show that the magnitude of the magnetoresistance ratio (both positive and negative) are strongly dependent both composition and geometry, (Fig.3.11).

The temperature dependence of magnetoresistance effect was investigated for two configurations, longitudinal and transverse geometries, with a constant magnetic field of 0.8T under the different temperature $20 \leq T \leq 320$ K. In both geometry, all the samples show an increase in the magnetoresistance ratio as temperature decreases. The increase in the magnetoresistance ratio with decreasing temperature may represent the reduction in spin-magnon scattering at lower temperatures i.e, represent the reduction in the number of magnons.

The magnetization properties of the NiFe alloy films were investigated with vibrating sample magnetometer (VSM) measurements at room temperature. The VSM measurements were carried out for two geometry, perpendicular and parallel. In both geometries, all the samples showed a ferromagnetic properties. The coercive fields have relatively low values, which are in agreement with other studies, indicating soft magnetic properties and they are almost in the same range as the magnetic field at which the maximum positive magnetoresistance effect is observed. And also it is shown that the coercive field H_c (at room temperature) show a decreasing behaviour with increasing Ni content in the film and the low coercivity value is attributed to a small grain size in the film samples. It can be deduced from the comparison of the hysteresis loops taken in parallel and perpendicular configuration that the easy direction of the magnetization is in the film plane while the hard direction lies perpendicular to the plane, which are in agreement with the theoretical interpretations.

In short, the electrodeposited Ni_xFe_{1-x} alloy films obtained in this work exhibited soft magnetic properties and magnetoresistance characteristics. They show a low coercive field (H_c) and relatively high magnetic saturation. Therefore, they could be employed in magnetic reading and writing heads, magnetic microsystems, magnetic sensors, transformers cores, magnetic memory technologies.

In this thesis, the electrodeposited NiFe alloy films were determined. As a next study, it may be the determination of the magnetic and magnetoresistance properties of the electrodeposited NiFe alloy films prepared under different electrodeposition conditions such as with different pH, temperature and current densities. Magnetoresistance properties of alloy films depend closely their grain sizes. The grain size of alloy films may be altered by heat treatment. The NiFe films used in this study may therefore be reexamined for their magnetic and magnetoresistance properties after applying heat treatment on them.

CHAPTER IV

General Conclusion

In this work, semiconducting CdS, CdSe and ZnSe thin films were fabricated at different substrate temperature by using spraying plyrolysis and electrodeposition method and their growth conditions, crystal structure, optical and electrical properties were investigated in detail using different techniques.

It was found that the high quality sprayed semiconducting CdS (1:1), CdSe (1:1) and ZnSe (1:1) thin films could be obtained on a glass substrate at the substrate temperatures of 380^0C, 420^0C and 430^0C and the corresponding flow rates of 0.5 ml, 0.5ml and 0.3.ml per min, respectively, when the distance between nozzle and substrate in all the processes was adjusted to be 20 cm.

In the electrodeposition process, It was observed that the high quality CdS thin films could be obtained at the applied potentials of 0.65-0.75 V, for a deposition time of 30-60 min, at a pH value of 1-2, at the solution temperatures of 70-75^0C and for the stirring rate at 400-600 rpm. For high quality CdSe thin films could be obtained at the applied potential of 0.55-0.60 V, for a deposition time of 30-60 min, at a pH value of 2.1-2.6, for the solution temperature of 60-65^0C and the stirring rate at 400-600 rpm. A high quality ZnSe thin film could be obtained at the applied potentials of 0.60-0.70 V, for a deposition time of 80-120 min, a pH value of 2.0-2.5, the solution temperature of 65-70^0C and the stirring rate at 400-600 rpm.

The band gaps of CdS, CdSe and ZnSe thin film samples were found as 2.44 eV, 1.76 eV and 2.68 eV, respectively. The crystal structures of the CdS, CdSe and ZnSe semiconducting thin films were investigated by x-ray powder diffractometer and their main diffraction peaks are found to be in agreement with other studies [21, 28, 64, 65].

The electrical properties of sprayed CdS, CdSe and ZnSe thin films were investigted by using Van der Pauw method. It is found that, the high quality semiconducting CdS, CdSe and ZnSe thin films were developed at 380^{0}C with a resistivity value of 3.93×10^5 ohm-cm and a Hall mobility value of 28 cm^2/Vsec, at 420^{0}C with a resistivity value of 5.8×10^5 ohm-cm and a Hall mobility value of 44 cm^2/Vsec and at 430^{0}C with a resistivity value of 57.9×10^5 ohm-cm and a Hall mobility value of 0.51 cm^2/Vsec, respectively.

The electrodeposition and spraying pyrolysis method are found to be very suitable methods for high quality and low cost semiconducting thin film growth. These methods do not require complex systems and sophisticated equipments. Electrodeposited CdS, CdSe and ZnSe thin films were developed on conducting substrate (nickel plate) but it was not possible to measure the electrical properties of these films due to the short circuit of these films to the nickel substrate.

The sprayed and electrodeposited CdS, CdSe and ZnSe thin films obtained in this work exhibited a near-ideal direct band gap, and high photosensitivity in the visible range of the solar spectrum. Therefore, these materials can be advantageously used in the applications of low cost solar cells and photo-electronic materials, detectors, light emitting devices.

Ni_xFe_{1-x} alloy films were fabricated with different compositions by using electrodeposition method and their crystal structure and magnetical properties were investigated. The NiFe alloy films were deposited at a current density of 16 mA/cm^2 for a deposition time of 15 min and a pH value of 3. The temperature of the solution was kept at room temperature during the deposition process and no stirring was done.

The compositions and thickness of the NiFe samples were determined by using an Atomic Absorption Spectrophotometer. The NiFe diffraction lines were detected by using an x-ray diffractometer at the diffraction angles where the FCC Ni and BCC Fe diffraction lines are expected. The lattice constant of NiFe alloy film was calculated using x-ray spectra of the films. It was found that the lattice constant of NiFe alloy film increases with increasing Ni content. The surface morfology of the NiFe alloy film was investigated by the Scanning Electron microscopy photos. It is observed that the surface of the films has granular structure and smooth surface.

The magnetoresitive properties of NiFe alloy films were investigated for different geometries. The NiFe alloy film samples show a pure positive, a mixture of positive and negative magnetoresistance effect and a pure negative magnetoresistance component depending on the measurement geometries. In the transverse geometry, the samples show a pure negative or a mixture of negative and positive components of the magnetoresistance effect depending on the film composition while any pure negative component was not detected in the longitudinal geometry.

Magnetoresistance effect was also investigated for the magnetic fields applied at different angles. The angular variation in magnetoresistance measurements were also studied from 0^0 to 90^0 for longitudinal-perpendicular geometry. These results showed that, as the angle between the applied field and the film plane increases, the negative component of magnetoresistance ratio starts to be seen with the positive component.

The temperature dependence of magnetoresistance effect was investigated for two configurations, longitudinal and transverse geometries, with a constant magnetic field of 0.8T under the different temperature $20 \leq T \leq 320$ K. In both geometry, all the samples show an increase in the magnetoresistance ratio as the temperature of sample decreases.

The magnetization properties of the NiFe alloy films were investigated with a vibrating sample magnetometer (VSM) at room temperature. The VSM measurements were carried out for two geometries, perpendicular and parallel. In the both geometries, all the samples showed ferromagnetic properties.

The coercive fields have relatively low values, which are in agreement with other studies, indicating soft magnetic properties. It can be deduced from the comparison of the hysteresis loops taken in parallel and perpendicular configuration that the easy direction of the magnetization is in the film plane while the hard direction lies perpendicular to the plane, which are in agreement with the theoretical interpretations.

Because the electrodeposited Ni_xFe_{1-x} alloy films obtained in this work exhibited soft magnetic properties and magnetoresistance characteristics due to their a low coercive field (H_c) and relatively high magnetic saturation, they may therefore employed in magnetic reading and writing heads, magnetic microsystems, magnetic sensors, transformers cores and magnetic memory technologies.

6.REFERENCES

[1] L.Timg, Chu, S. Shifrley. Chu and Shırley S. Chu..(1995). *Sol. Stat. Electr.* **38**. 533-549

[2] R.N.Bhattacharya and K.Rajeshwar. (1985). *J.Appl.Physc.***58.** 9-13

[3] Trevor A. Chynoweth and Ricard H.Bube. (1980). *J.Appl.Phys.* **51**(3).1844

[4] D.W.Lane, K.D.Rogers, J.D.Painter, D.A.Wood and M.E.Özsan. (2000). *Thin Films.***1**(8). 361-362

[5] D. Gal, G. Hodes.(2000). *J.Electrochem.Soc.***147**(5), 1825-1828

[6] M.E.Özsan, D.R.Jhonson, S.Oktik and M.H.Patterson. (1994). *12.European PVSEC.* Amsterdam

[7] M.Ilieva, D.Dimova, B.Ranguelov and I.Markov. *J.Phys:Condens Matter.* **11**.10025-10031

[8] T.Mahalingam and C.Sanjeeviraja. (1992). *Phys.State.Sol.(a).* **K89**.129

[9] T.Gruszecki, B.Holmström. (1998). *Solar Energy Materials.* **51** 243-253

[10] M.Öztaş. (1996). Ph.D Thesis. *University of Gaziantep*

[11] A.P. Samantılleke, M.H. Boyle, J. Young, I.M. Dharmadasa. (1998). *J. Materials Science: Materials in Electronics.* **9**. 231-235

[12] M. Musiani. (2000). Electrochimica Acta. **45**. 3397-3402

[13] J.N. Hilfiker, D.W.Thompson, J.S.Hale. J.A.Woollen. (1995). *Thin Solid Films.* **270**. 73-77

[14] Ö.F.Bakkaloğlu, İ.H.Karahan, H.Efeoğlu, M.Yıldırım, U.Çevik, Y.K.Yoğurtçu. (1998) *J.Magnetism and Magnetic Materials.* **190**. 193-198

[15] L.J. Gao, P.Ma, K.M. Novogratecz, P.R. Norton. (1997). *J.Appl.Phys.* **81**. 7595-7598

[16] J.Neamtu, M.Volmer, A.Coraci. (1999). *Thin Solid Films*. **343.** 218-221

[17] A.A.Pasa, W.Schwarzacher.(1999). *Phys.Stat.Sol.* **173**. 73-77

[18] L.Wang, P.Fricoteaux, K.Yu-Zhang, M.Troyon. (1995). *Thin Solid Films.*212. 160-167

[19] H.El Fanity, K.Rahmouni, M.Bouanani, A.Dinia, (1998). *Thin Solid Films.* **318.** 227-230

[20] S.N.Alamir, A.W.Brinkman. (2000). *J.Phys.D:Appl.Phys.***33**. L1-L4

[21] S.A.David, H.R.Subhash. (1987). *Thin Solid Films*. **147**. 203-212

[22] K.L.Chopra, R.C.Kaintla, P.K.Pandya, A.P.Thakoor. (1982). *Physics of Thin Films*. **12**.167-171

[23] K.L.Chopra, S.R.Das, *Thin Film Solar Cells*. (1983*). Plenum Press*. Newyork.

[24] K.L.Chopra. (1969). Thin Film Phenomena. *McGraw-Hill Book Company*. Newyork

[25] J.E.Hill, R.R.Chamberlin. (1964*). US Patent*. **3**. 148084

[26] R.R.Chamberlin, J.S.Skarman.(1966). *J.Electrochemical Society.* **113**. 86-90

[27] R.R.Chamberlin, J.S.Skarman. (1966). *Solid State Electronic*. **9**. 819-822

[28] R.S.Feigelson, A.N.Diage, S.Yin, R.H.Bube. (1977). *J.Appl.Phys.* **48**. 3162-3165.

[29] Y.Y.Shaiw, A.L.Fahrenbruch, R.H.Bube. (1978). *J.Appl.Phys.* **52**. 4963-4966

[30] T.A.Chynoweth, R.H. Bube. (1980). *J.Appl.Phys.* **51**. 1844 –1846

[31] M.Krunks, E.Mellikov, E.Sork. (1986). *Thin Solid Films.* **105**. 145-147

[32] H.Luquest, M.Perotin, A.Dhould, J.Bougnot, M.Savelli. (1986). *Solar Cells.* **13**. 289-294

[33] P.K.Gogna, L.Malhotra, K.L.Chopra.(1977). *Research and Industry.***22**. 77-80

[34] A.Banerjee, P.Nath, V.D.Vankor, K.L.Chopra. (1978). *Physc.Stat.Solid (a).* 46. 723-726

[35] S.R.Das, A.Banerjee, V.Dutta, K.L.Chopra.(1979). *Sol.Stat.Electr.* **22**. 533-535

[36] E.Shanthi, A.Banerjee, V.Dutta, K.L.Chopra. (1980). *J.Appl.Physc.* **18**. 6243

[37] S.Major, A.Banerjee, V.Dutta, K.L.Chopra. (1982). *Thin Solid Films.* **133**. 179-183

[38] K.S.Ramaiah, R.D.Pilkington, A.E.Hill, R.D.Tomlinson, A.K.Bhatnagar. (2001). *Materials Chemistry and Physics.* **68**. 22-30

[39] H.L.Kwok, W.C.Siu. (1979). *Thin Solid Films.* **61**. 249-252

[40] H.L.Kwok. (1983). *J.Appl.Phys.D.* 16. 2367-2370

[41] M.S.Tomar, F.J.Garcia. (1980). *Japan J.Appl.Phys.* **19**. 567-571

[42] P.J.George, A.S.Juarez, P.K.Nair.(1996). *Semicond.Sci. Technol.* **11**. 1090-1095

[43] A.L.Dawar, P.K.Shishodia, G.Chauhan, A.Kumar, P.C.Mathur. (1990).*J.Materials Sci. Lett.* **9**. 547-548

[44] R.R.Bon, N.C.S.Inda, F.J.E.Beltran. (1997). *J.Phys.:Condens.Matter*. **9**. 10051-10058

[45] S.J.Lade, C.D.Lokhande. (1997). *Materials Chemistry and Physics*. **49**.160-163

[46] A.Mzerd, D.Sayah, I.J.Saunders,B.K.Jones.(1990). *Phys.Stat.(a)*.**119**. 487-490

[47] B.M.Başol.(1988). *Solar Cells*.**23**. 69-88

[48] F.Kroeger. (1978). *J.Electrochem. Soc*. **125**. 2028-2032

[49] S.S.Ou, O.M.Stafsudd, M.Başol. (1984). *J.Appl.Physc*. **55**(10). 3769-3772

[50] R.N.Bhattacharya, K.Rajeshwan.(1985). *J.Appl.Physc*.**58**(9).3590-3593

[51] M.Tomkiewicz, I.Ling,W.S.Parsons. (1982). *J.Electrochem*.**129**(9).2016-2022

[52] S.K.Das, G.C.Morris. (1993). *J.Appl.Physc*.**73**(2).782-786

[53] M.Takahashi, K.Uosaki, H.Kita. (1986).. *J.Appl.Physc*.**60**(6).2046-2049

[54] T.Mahalingam, C.Sanjeeviraja. (1992). *Phys.Stat.Sol.(a)*.**129**.K89

[55] S.Eriksson, T.Gruszecki, P.Carlsson, B.Holmström. (1995). *Thin Solid Films*. **269**.14-17

[56] H.Wynands, M.Cocivera. (1992). *J.Electrochem.Soc*. **139** (7).2052-2057

[57] P.N.Gibson, M.E.Özsan, D.Lincot, P.Cowache, D.Summa. (2000). *Thin Solid Films*. **361/2**. 84-87

[58] G.Sasikala, R.Dhanasekaran, C.Subramanian. (1997). *Thin Solid Films*.**302**. 34-40

[59] H.Cachet, R.Cortes, M.Froment, A.Etcheberry. (2000). *Thin Solid Films*. **361/2**. 84-87

[60] R.P.Silberstien, M.Tomkiewics. (1983). *J.Appl.Physc*. **54**(3). 5428-5435

[61] S.J.Lade, M.D.Uplane, C.D.Lokhande. (1998). *Materials Chemistry and Physics*. **53**. 239-242

[62] R.S.Mane, C.D.Lakhande. (1997). *Thin Solid Films*. **304**. 56-60

[63] S.J.Lade, M.D.Uplane, M.M.Uplane, C.D.Lokhande. (1998). *J.Material Science: Materials in Electronics*.**9**. 477-482

[64] D.Gal, G.Hodes. (2000). *J. Electrochem. Soc.* **147**(5). 1825-1828

[65] G.Riveros, H.Gomez, R.Henriquez, R.Schrebler, R.E.Marotti, E.A.Dalchiele. (2001). *Solar Energy Materials and Solar Cells*. **70**. 255-268

[66] A.Barlev. (1993). Semiconductor and Electronic Devices.Technio-Israel. *Ins.of Tech.* Prentice-Hall.

[67] H.J.M.Bowen.(1976). Properties of Solids and Their Atomic Structure. *McGraw-Hill Pub.Comp.Limit.*New York.

[68] M.A.Omar.(1975). Elementary Solid State Physics, Principles and Applications. *Addison -Wesley Pub. Comp.*London.

[69] P.D.Townsend. (1973). Colour Centers and Imperfections in Insulators and Semiconductors. *Crane,Russak and Comp.Ins.*New York.

[70] R.H.Bube.(1978).Photoconductivity of Solids.*R.E.Krieger Pub.Com.*New York.

[71] A.Van Der Ziel.[1976).Solid State Physical Electronics. *Prentice-Hall. Inc.* New York.

[72] T.E.Jenkins.(1995). Semiconductor Science Growth and Characterization Techniques.*Prentice-Hall.* New York.

[73] W.Ruythooren, K.Attenborough, S.Beerten. (2000) Electrodeposition for the Synthesis of Microsystems. *J.Micromech.Microeng.***10**. 101-107.

[74] B.D.Cullite.(1972).Introduction to Magnetic Materials. *Addison-Wesley Pub. Comp.* London.

[75] C.G.Kim, H.C.Kim,B.S.Park. (1999). *J.Magnetism and Magnetic Materials.***198**/9.33-35

[76] M.Volmer, J.Neamtu.(2001). *Surface Science.* **482**/5.1010-1014

[77] W.Brückner, S.Baunack, M.Hecke. (2001). *Material Science and Engineering.***B86**.272-275

[78] L.Vila, W.Park, J.A.Caballero. (2000). *J.Appl.Physc.***87**(12). 8610-8614

[79] M.U.Rana, T.Abbas, F.A.Khawaja. (2002). *Materials Letters.***52**. 389-393

[80] H.S.Nam, T.Yokoshima.(2001). *Thin Solid Films.***384**. 288-293

[81] C.J.Wang, L.Wu-Yan. (2001).. *Chin.Phys.Lett.***18**(12). 1651-1654

[82] L.Tie, S.H.Lie. (2002). *Chin.Phys. Soc.* **11**(1). 54 –57

[83] A.O.Adeyeye, R.P.Cowburn, M.E.Welland. (2000). *J.Magnetism and Magnetic Materials*. **213**. L1- L6

[84] N.Myung.(2001)*Bull. Korean Chem.Soc.***22**. 9-14

[85] I.Tabakovic, V.Inturi and S.Riemer. (2002). *J.Electrochemica Society.* **149**(1) 18-22

[86] H.Gong,D.litvinov and T.J.Klemmer. (2000). *IEEE Transactions on Magnetics.* **36**(5).2963-2965

[87] M.Xu,C.Chai, G.Luo, T.Yang, Z.Mai and W.Lai. (2000). *Thin Solid Films.* **375**.205-209

[88] J.Neamtu and M.Volmer, A.Coraci.(1999). *Thin Solid Films.* **343/4**. 218-221

[89] F.Czerwinski and J.A.Szpunar. (2000). *J.Materials Science: Mareials in Electronics.* **11**. 243-251

[90] H.R.Khan, K.Petrikowski. (2000). *J. Magnetic and Magnetic Materials.* **215/6**. 526-528

[91] Y.Shimazu, K.Sakai, T.Noda, I.Yamamoto, M.Yamaguchi. (2000). *Physica (B)* **284/8**. 1239-1240

[92] N.V.Myung, K.Nobe. (2001). *J.Electrochem.Soc.***148**(3).C136-C144

[93] W.F.Smith.(1990). *Principles of Materials Science and Engineering.* (2^{nd} Ed.). Mc-Graw Hill Int.Edi. New York

[94] J.C.Anderson, K.D.Leaver, J.M.Alexander, R.D.Rawlings. (1980). *Materal Science* (2nd Ed.). Thomas Nelson and Sons. Ltd. G.Britain

[95] D.Jastrzebski. (1959). *Nature and Properties of Engineering Materials.* Edition by Wiley Int. New York

[96] H.P.Myers. (1990). *Introductory Solid State Physics.* Pub. Taylor and Francis. London-New York

[97] J.A.Jacobes, T.F.Kilduff. (1985). *Engineering Materials Technology.* Prentice Hall. Inc. New Jersey

[98] H.M.Rosenberg, E.J.Burge, D.J.E.Ingram, J.A.D.Matthew. (1988). *The Solid State* (3rd Ed.). Oxford Physics Series

[99] C.Kittle.(1986). *Introduction to Solid State Physics* (8th Ed.). John Wiley and Sons.Inc

[100] K.L.Horovitz, V.A.Johnson. (1959). *Methods of Experimental Physics* (Part B).**6**. Academic Press. New York

[101] J.Q.Xiao, J.S.Jiang, C.L.Chien. (1992). *Physical Review B.*(46) **14**. 9266-9269

[102] J.Balogh, L.F.Kiss, A.Halbritter. (2002). Magnetoresistance of Ag/Fe/Ag and Cr/Fe/Cr Trilayers. *Solid State Com*. Inpress

[103] A.Siritaratiwat, E.W.Hill. (2000). *Sensors and Actuators*.**81**. 40-43

[104] S.H.Charap. (1964). *Physics of Magnetism*. John Wiley and Sons. Inc. New York

[105] I.Vitina, M.Lubane, A.Korne, V.Rubene, V.Belmane, Z.Zarina, A.Krumina (1995). *Thin Solid Films*. **270**. 380-385

[106] H.Wang, S.P.Wong, X.Lu, X.Yan, W.Y.Cheung, N.Ke, S.Hu, D.Zeng, Z.Liu. (2000). *J.Phys: D:Appl. Phys.***33**. 1464-1467

[107] E.C.Stoner, E.P.Wolhfart, (1948). *Proc.Trans.Roy.Soc.* **240**. 599-563

7.CURRICULUM VITAE

The author was born in Osmaniye, in January, 1965. He graduated from the primary, secondary and high schools in Osmaniye, in 1978, 1981 and 1984, respectively. He received a B.S. degree from University of Çukurova, Faculty of Arts and Science, Department of Physics in 1991. He also received an M.Sc. degree from University of Çukurova, Applied and Natural Science Institute, Department of Physics in 1994. He started to work as a research assistant in the Department of Engineering Physics, University of Gaziantep in 1991. In 1995, he was accepted to a Ph.D. program in the Department of Engineering Physics, Universty of Gaziantep. He is currenty working as an instructor in the Department of Engineering Physics, University of Gaziantep since 1999.

He married in November, 1992 to Z. Emel and he has two daugthers T. İrem and E.Ece.